SANDIA REPORT
SAND2012-8099
Unlimited Release
Printed September 2012

First-Principles Flocculation as the Key to Low Energy Algal Biofuels Processing

John C. Hewson, Nicholas B. Wyatt, Flint Pierce, Xuezhi Zhang, Pasquale Amendola, David A. Barringer, Patrick V. Brady, Brian P. Dwyer, Anne M. Grillet, Matthew G. Hankins, Qiang Hu, Lindsey G. Hughes, Jeremy B. Lechman, Lisa A. Mondy, Jaclyn K. Murton, Timothy J. O'Hern, Kylea J. Parchert, Philip I. Pohl, Milton Sommerfeld, Cecelia V. Williams

Prepared by
Sandia National Laboratories
Albuquerque, New Mexico 87185 and Livermore, California 94550

Sandia National Laboratories is a multi-program laboratory managed and operated by Sandia Corporation, a wholly owned subsidiary of Lockheed Martin Corporation, for the U.S. Department of Energy's National Nuclear Security Administration under contract DE-AC04-94AL85000.

Sandia National Laboratories

Issued by Sandia National Laboratories, operated for the United States Department of Energy by Sandia Corporation.

Available to DOE and DOE contractors from
U.S. Department of Energy
Office of Scientific and Technical Information
P.O. Box 62
Oak Ridge, TN 37831

Telephone: (865) 576-8401
Facsimile: (865) 576-5728
E-Mail: reports@adonis.osti.gov
Online ordering: http://www.osti.gov/bridge

Available to the public from
U.S. Department of Commerce
National Technical Information Service
5285 Port Royal Rd.
Springfield, VA 22161

Telephone: (800) 553-6847
Facsimile: (703) 605-6900
E-Mail: orders@ntis.fedworld.gov
Online order: http://www.ntis.gov/help/ordermethods.asp?loc=7-4-0#online

SAND2012-8099
Unlimited Release
Printed September 2012

First-Principles Flocculation as the Key to Low Energy Algal Biofuels Processing

John C. Hewson, Nicholas B. Wyatt, Flint Pierce, Patrick V. Brady, Brian P. Dwyer, Anne M. Grillet, Matthew G. Hankins, Lindsey G. Hughes, Jeremy B. Lechman, Lisa A. Mondy, Jaclyn K. Murton, Timothy J. O'Hern, Kylea J. Parchert, Philip I. Pohl, Cecelia V. Williams

Sandia National Laboratories
P.O. Box 5800
Albuquerque, New Mexico 87185

Xuezhi Zhang, Qiang Hu, Pasquale Amendola, Monica Reynoso, Milton Sommerfeld

Department of Applied Sciences and Mathematics
Arizona State University, Polytechnic Campus
Mesa, AZ 85212

Abstract

This document summarizes a three year Laboratory Directed Research and Development (LDRD) program effort to improve our understanding of algal flocculation with a key to overcoming harvesting as a techno-economic barrier to algal biofuels. Flocculation is limited by the concentrations of deprotonated functional groups on the algal cell surface. Favorable charged groups on the surfaces of precipitates that form in solution and the interaction of both with ions in the water can favor flocculation. Measurements of algae cell-surface functional groups are reported and related to the quantity of flocculant required. Deprotonation of surface groups and complexation of surface groups with ions from the growth media are predicted in the context of PHREEQC. The understanding of surface chemistry is linked to boundaries of effective flocculation. We show that the phase-space of effective flocculation can be expanded by more frequent alga-alga or floc-floc collisions. The collision frequency is dependent on the floc structure, described in the fractal sense. The fractal floc structure is shown to depend on the rate of shear mixing. We present both experimental measurements of the floc structure variation and simulations using LAMMPS (Large-scale Atomic/Molecular Massively Parallel Simulator). Both show a densification of the flocs with increasing shear. The LAMMPS results show a combined change in the fractal dimension and a change in the coordination number leading to stronger flocs.

ACKNOWLEDGMENTS

This program to improve our understanding of algal flocculation and harvesting was initiated through the Laboratory Directed Research and Development (LDRD) program, and the authors of this report are indebted to many people for their continued support. We have benefited in particular from the braider understanding of the bioenergy landscape provided by Ron Pate, Blake Simmons, Grant Heffelfinger, Anthony Martino and Ben Wu. In building our understanding of algae and cultivation practices, we have benefited from interactions with Jeri Timlin, Todd Lane and Ryan Davis.

CONTENTS

FIGURES

TABLES

1 INTRODUCTION

Concerns about energy security, resource depletion and environmental consequences of fossil fuel use have motivated the development of biomass as a source raw material for biofuels. Much of the oil that we remove from the ground as petroleum today originated as algae, and a significant fraction of the biomass on the earth at any given time is associated with algae. Algae have potential as a significant source of biomass due to its high photosynthetic efficiency, high growth rates and high lipid fraction. Further, algae can grow in brackish and saline waters, reducing the need to employ valuable fresh water resources for biofuel production. Algae also consume nitrates and phosphates in waters, making them valuable for cleaning municipal and agricultural waste streams in some communities. With their potential for high oil production per acre relative to other biofuels sources, algal biofuels have the potential to substantially contribute to energy diversity if certain barriers can be overcome [1-12].

A significant barrier is the energy/cost associated with harvesting and dewatering algae. Algae cultures grow to densities on the order of one kilogram of biomass per ton of water, and the cost of pumping water is a significant concern for energy efficient and economic biomass production. While advanced cultivation methods can yield somewhat higher yields, the cost to move one thousand times more water to recover biomass rapidly becomes prohibitive.

A typical approach to separating solids in suspension is centrifugation, and this has been employed for algae, especially in industries where nutritional and cosmetic products with high values can be obtained. The energy associated with centrifugation is proportional to the volume of the culture media, however, and the energy cost to centrifuge algae of typical culture density is comparable to the energy in a potential biofuel product [5]. Filtration is another approach to solids separation that is favorable at low culture densities [13]. However, the small cell size of productive algal species and the existence of a continuum of sizes of organic matter from the lysed cell fragments to organic macromolecules can cause membrane fouling and increase pumping costs [5].

Algae flocculation is a potentially low cost and low energy approach to providing the initial separation of the biomass from the bulk of the culture media [2, 14-39]. If algal cells come together and form sufficiently large flocs, their differential density will cause them to gravitationally settle, or to float in the presence of bubbles. The resulting biomass slurry or paste generally has a relatively high liquid content (perhaps as high as 80-90% water), but the order of magnitude or greater concentration and increased floc size make subsequent processing with filter presses or centrifuges energy efficient.

Flocculation is a common means for separation of solids from suspensions and several notable reviews outside of the algae-harvesting field can be referred to understand the progress of the field to date. Bratby provides a broad overview of the field as it applies to water treatment [40], while Gregory reviews flocculation at a more fundamental level [41]. Duan and Gregory provide an overview of the chemistry of typical inorganic flocculants used in water treatment, in particular Fe and Al based flocculants like those employed in much of the present work [42].

1.1 ALGAE SURFACE CHARGE

The small size and low concentration of algal cultures make separation by settling or flotation difficult, but it is the ionic nature of the algal cell surface that provides the first barrier to floc growth. Algae like other cellular organisms have organic molecules on their cell surfaces that are strongly hydrophilic. These hydrophilic surfaces are the result of acidic and neutral polysaccharides and proteins on the surface [43]. Typical polysaccharides might be from the class of pectins and include uronic acid and similar functional groups [43]. Further, surface functional groups are often charged under culture conditions. Carboxyl groups (uronic acid is a carboxylated sugar) are typical of cell surfaces and these tend to dissociate to a negatively charge group for pH much above four. Other typical groups include hydroxyl and phosphate groups that tend to be negatively charged; amine groups are positively charged at neutral pH [44]. Overall, it has long been known that a negative surface charge exists that serves to stabilize the suspension at most pH [45]. In Sec. 3.1 we describe measurements of the algae surface charge.

This negative surface charge interacts with the ionic content of the water (indeed the development of charge depends on the hydronium ion concentration), and complexes between cell surface molecules and ions in the culture media will influence the net surface charge. To induce flocculation, it is generally necessary to induce favorable, or at least overcome unfavorable, surface charges. In Sec. 3.2 we discuss the prediction of surface complex formation that allows us to predict the change in the charge density on the algal cell surface with the change in the ionic content of the culture media.

For algae flocculation the surface charge density is high enough (see Sec. 3.1) that precipitates with favorable surface charges are found to be the most effective means of overcoming the algae surface charge. This is the mechanism by which traditional inorganic salts used for water treatment appear to act in conjunction with algae; iron and aluminum-based salts are typical examples. The phase space over which these typical flocculants work for algae is discussed in Sec. 2.1 in work that is based on experimental observations. The boundaries for effective flocculation are related to the surfaces of the algae and the precipitates there, and the prediction of the precipitate surface charges is discussed in Sec. 3.2. More attention is paid to the precipitation and surface charges of natural salts that are potential flocculants. Calcium and magnesium are present in seawater and often in brackish waters in concentrations sufficiently high to precipitate at high pH. Since photosynthetic growth of algae tends to increase the pH, this occurrence of flocculation can sometimes be induced automatically by just neglecting to mix in enough CO_2 to maintain near neutral pH. This so-called autoflocculation is described in Sec. 2.2.

1.2 FLOC GROWTH AND SEPARATION

If the surface charge is overcome, there will be a tendency for algae to flocculate, but the time scales for floc growth and separation are generally too small and the density of the settled flocs is too low without some influence of fluid mixing. The fact that promising algae are larger than one micron means that Brownian diffusion is generally not very effective in bringing cells together. Fluid mixing creates shear that can bring cells together (Figure 1) and this is generally the primary means of initial floc growth. Larger flocs will typically settle faster than smaller flocs and differential settling is also a significant mode of floc growth for floc sizes in the tens of microns and larger (Figure 1).

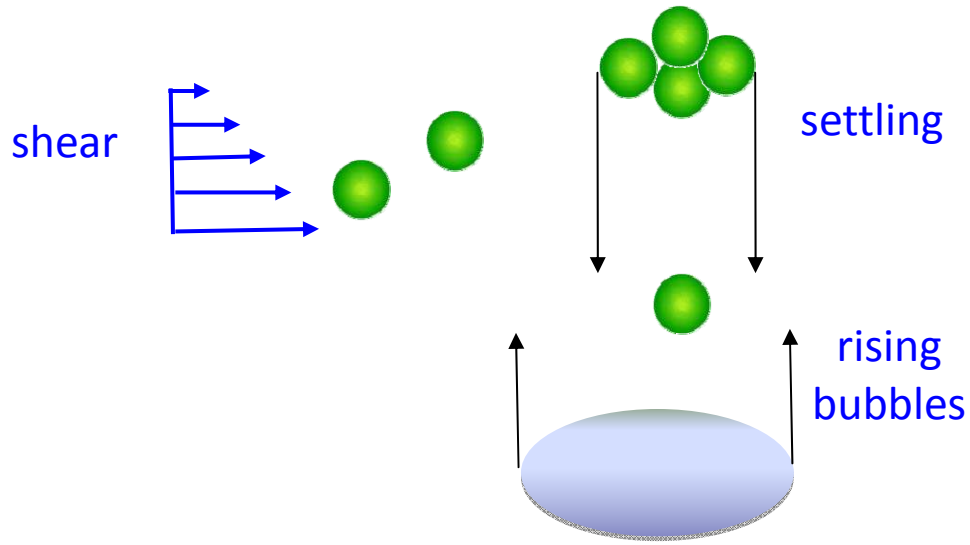

Figure 1. Schematic representation of shear and settling modes of particle interaction.

Dissolved air flotation (DAF) also operates in the differential-settling regime. In DAF, bubbles nucleate due to the injection of supersaturated air, and typical bubble sizes are fifty to seventy microns. These bubbles interact with algae cells and their buoyancy brings the algae to the surface, leaving a subnatant that can be decanted. The efficiency of DAF algae separation is described in Sec. 2.1 where it is shown that added flocculant is generally required to attain good separation efficiencies. Added flocculant provides two benefits: it collects the large number of algae cells into a smaller number of flocs that can be collected by the injected bubbles, and it neutralizes anionic surface charges on both algae flocs and bubbles to allow more efficient adhesion. In Ref. [46] we describe a model for DAF-based separation. The key development associated with this model is its identification of the importance of the degree of pre-flocculation in determining the overall separation efficiency. The biomass loadings in algae cultures are large enough that without pre-flocculation there are not enough bubbles to collect all of the algae cells.

The degree of mixing required to grow flocs is an important energy consideration, but mixing can have two other effects: it is observed to both restructure and fragment flocs. Restructuring leads to denser flocs and can be beneficial if the flocs are designed to settle. Greater floc density will generally lead to higher solids fractions in the separated slurry or paste. On the other hand, denser flocs have smaller collision cross sections, leading to slower overall growth or reduced interaction with bubbles. Floc fragmentation can also lead to denser flocs and it results in an upper bound on the stable floc size for a given input shear energy. To optimize separation processes requires an understanding of the interplay between floc growth, restructuring and fragmentation. This balance between floc growth and fragmentation is particularly evident in Couette flow experiments where steady state size distributions can be observed. In Sec. 4 we describe algae floc characteristics in Couette flow and compare these with observations of other particle systems.

To better understand this interplay between floc growth and restructuring, we describe in Sec. 6 and 7 simulations using the LAMMPS (Large-scale Atomic/Molecular Massively Parallel Simulator) code. These provide a fully exposed view of particle dynamics that allows us to observe in detail the simultaneous growth, restructuring and fragmentation of flocs. The results

show the shift from relatively open (low density flocs) at early stages of growth to more dense flocs. The higher density is clearly evident in flocs larger than a critical size and the density can be characterized in terms of an increase in both the fractal dimension and the average coordination number. While the change in the fractal dimension with time is observed experimentally, this detailed view of restructuring during floc growth has never been reported experimentally demonstrating the value of high fidelity simulations applied to difficult-to-observe processes.

In Sec. 5 we bring together the mixing, restructuring, fragmentation and differential settling driven evolution of the floc size distribution. A sectional model discretizes the size distribution and describes the relative flux of mass to larger and smaller size flocs through the combined effects of each of these processes. The long term evolution of the size distribution can be predicted with these models as can steady state distributions. In the long term, these will be the appropriate models to couple with computational fluid dynamics methods to optimize flow and flocculation together.

2 A REVIEW OF ALGAE FLOCCULATION

In this section we review past research in algae flocculation, and highlight some results coming from this project that are detailed in Refs. [37, 38]. Algae flocculation practice is similar to water treatment [18, 40]. However, the economics of algal flocculation are less favorable than those of water treatment because the flocculant requirements per mass of algae harvested are relatively large compared to the flocculant required to treat a given quantity of water. To leading order, except at very high concentrations of solids (discussed later and in [37]), flocculant requirements increase with the mass of algae to be separated, and the mass densities of algae in intentional algae cultivation are several orders of magnitude larger than are typical in water treatment.

Algae flocculation is generally associated either with the precipitation of favorably charged inorganic salts or organic polymers. A list of typical algal flocculants is provided in Table 1. The present work will focus on inorganic flocculants with a particular emphasis on the precipitation of bulk salts at high pH.

Table 1. Algae flocculants

	Flocculant	Mechanism
Metals	Alum	Charge neutralization (low pH), sweep flocculation (high pH)
	PACl	Charge neutralization/Bridging
	Fe(III) chloride/sulfate	Charge neutralization (low pH), sweep flocculation (high pH)
	Lime (CaO, $Ca(OH)_2$)	Increase pH, charge neutralization
	Mg	Charge neutralization by formed $Mg(OH)_2$
Organics	Cationic polyelectrolytes – Chitosan, Polydiallyldimethylammonium chloride (PolyDADMAC), Cationic polyacrylamides (e.g. Praestol Zetag 63 and 92), Cationic starches, Microbial bioflocculants (AM49), Purifloc C-31	Charge neutralization/Bridging
	Anionic polyelectrolytes (+ Ca^{2+}, Mg^{2+})	Charge neutralization/Bridging

2.1 FLOCCULATION WITH INORGANIC SALTS

In water treatment, aluminum and iron-based flocculants (i.e. $Al_2(SO_4)_3$ and $FeCl_3$) are typically employed, and these are added in concentrations that lead to precipitation in the form of metal hydroxides [40, 42]. The most typical precipitates are $Al(OH)_3$ and $Fe(OH)_3$, but a wider range of forms are commonly observed with aluminum [47]. The basic mechanism for flocculation involving multivalent cationic salt flocculants involves a mutual attraction and subsequent neutralization of the algae charge by the oppositely charged hydroxide of the flocculant.

Duan and Gregory provide a comprehensive review of flocculation using Fe and Al based flocculants as of 2002 [42]. Metal cations are hydrated in water and with a highly charged metal cation the hydrating molecules become strongly polarized leading to displacement of hydronium and reactions like

$$Me^{3+} \rightleftarrows Me(OH)^{2+} \rightleftarrows Me(OH)_2^{+} \rightleftarrows Me(OH)_3 \rightleftarrows Me(OH)_4^{-} \quad (1)$$

with reactions progressing further to the right under higher pH conditions because of the availability of OH^- in the solution. Equilibrium constants are given in Table 2 along with solubility constants for the amorphous phase precipitates. These equilibrium constants are based on the following reaction set

$$\begin{aligned} Me^{3+} + H_2O &\rightleftarrows Me(OH)^{2+} + H^+ && K_1 \\ Me(OH)^{2+} + H_2O &\rightleftarrows Me(OH)_2^{+} + H^+ && K_2 \\ Me(OH)_2^{+} + H_2O &\rightleftarrows Me(OH)_3 + H^+ && K_3 \\ Me(OH)_3 + H_2O &\rightleftarrows Me(OH)_4^{-} + H^+ && K_4 \\ Me(OH)_3(amorph) &\rightleftarrows Me^{3+} + 3OH && K_{s,amorph} \end{aligned} \quad (2)$$

Note that the Al species constants are grouped into a narrow range of pH from 5 to 7 while the Fe constants span the range of $2 < pH < 10$ (see Table 2 and figures from Refs. [48] and [49]). This suggests that one goes from Al^{3+} to $Al(OH)_4^-$ in a narrow range while each of the ferric species has a regime over which it is the dominant soluble species.

Table 2. Hydrolysis and solubility constants from [48] and [49].

	pK_1	pK_2	pK_3	pK_4	$pK_{S,amorph}$
Al^{3+}	4.95	5.6	6.7	5.6	31.5
Fe^{3+}	2.2	3.5	6	10	38

Polynuclear species can be formed from both Fe and Al, but those in the Al system are better studied with good evidence for $Al_{13}O_4(OH)_{24}^{7+}$ (a central $Al_{13}O_4^{5-}$ surrounded by 12 Al $Al(OH)_2^+$) [42]. Duan notes that the surface charge characteristics and isoelectric points for precipitates depend on the preparation of the precipitate. For example, he notes that the i.e.p. (iso-electric point) for $Al(OH)_3$ precipitated from $AlCl_3$ is around 9 while that precipitated from $Al_2(SO4)_3$ is around 8. For amorphous $Fe(OH)_3$ precipitate the i.e.p. is somewhat lower. They note a dependence on the ratio of the cation to OH^- and to the presence of polyvalent anions like sulfate. In general, for pre-hydrolysed precipitates, the i.e.p. is one or more pH units greater, potentially giving a wider bound for the cation-anion interactions [42].

The application of the ferric-based flocculant $FeCl_3$ to algae harvesting was investigated in this work, and is the subject of Ref. [37]. There are several key results. First, flocculation is limited to $pH > 4$ because for lower pH the algal surface is cationic and unfavorable to reaction with strongly cationic ferric species. At high pH where ferric species are anionic along with the algae surface there were no observed limitations on the flocculability. This is presumed to be because the net ionic charge on the algae is formed from a combination of anionic surface groups (like carboxylic groups) and cationic surface groups (like amine groups) while the ferric hydroxide precipitate has an overall cationic charge.

Second, the required dosage of flocculants like $FeCl_3$ for high efficiency flocculation is relatively high. When the algae concentration is below 1g/L, there is an approximate linear relationship, referred to in the literature as the stoichiometric relationship, between the algal mass and the required flocculant with approximately 0.7 g $FeCl_3$ required per gram of algal biomass [37].

This value is expected to depend on the species, but results of this magnitude have been found in other work [20, 27] and also with aluminum-based coagulants [27, 38].

For higher algae concentrations, above 1 g/l the results of [37] show that less flocculant per mass of algae is required . The reduced flocculant requirements at high algae concentrations are related to the more frequent collisions between flocs that occur at high densities. These more frequent collisions allow flocculation to occur even when the algae surface is less completely covered by flocculant. This is significant because it shows the value of cultivating algae at high densities in terms of reducing flocculant costs.

In another paper to come out of this project, Zhang et al. quantify the aluminum flocculant requirements for varying degrees of harvesting efficiency [38]. In that work the tendency to require stoichiometric concentrations of flocculant is related to the concentrations of charged functional groups on the algae surface. It was also shown that later in the lifecycle, the concentrations of these functional groups decline and this leads to reduced flocculant requirements. Since this late-stage growth corresponds to higher lipid contents under nitrogen-starvation conditions, this can be an effective method of reducing the flocculation costs while simultaneously increasing lipid yields [38].

Another key result that has come out of the work from this project is the quantification of interactions between dissolved organic material (DOM) and flocculants. DOM is organic matter not associated with the actual cells, although a large fraction or the majority may originate with the algae. DOM has similar functional groups as the cell surface and associates with the flocculant, effectively reducing the quantity of flocculant that can neutralize the surface charges [17, 50-52]. DOM is found in our work to vary over the algae cultivation lifecycle, increasing in later stages, but this was not as strong of an effect as the reduction in the flocculant requirements associated with the reduced concentrations of surface functional groups [38].

In Ref. [38]it was found that the harvesting efficiency dependence on flocculant dosage (in the absence of DOM) could be empirically be expressed in the general form of a logistic equation of the form

$$\eta = A_1 + \frac{A_2 - A_1}{1 + \exp\left(A_0 - B \cdot \alpha_{algae}(\eta)\right)} \tag{3}$$

where η is the harvesting efficiency, and A_i and B are system-dependent empirical constants that are tabulated for one system in Ref. [38]. The parameter $\alpha_{Algae}(\eta)$ is the flocculant dosage per mole of functional surface groups. A benefit of the relation between required flocculant dosage and the harvesting efficiency in the form of Eq. (3) is that one can identify the benefit of additional coagulant in terms of the additional algae harvested. This is of interest primarily for determining the economic costs for different process designs. For example, differentiating Eq. (3) and multiplying by the concentration of surface sites, $(Y_F - Y_{F,0})$, yields

$$(Y_F - Y_{F,0})\frac{d\alpha_{Algae}}{d\eta} = \frac{(Y_F - Y_{F,0})}{B}\left(A_0 - \log\frac{A_2 - \eta}{\eta - A_1}\right) \tag{4}$$

the additional Al^{3+} dosage required in the DOM-free cultures to increase the efficiency by $d\eta$ above η. The quantity that depends only on η, $d\alpha_{Algae}/d\eta$, is plotted in Figure 2 demonstrating that the marginal cost of improving flocculation is low in the vicinity of 50%, but the marginal additional coagulant requirement is greatly increased at the highest efficiencies. In other words, the benefit of additional coagulant is greatly reduced at the highest efficiencies potentially leading to a reduced return on investment in coagulants. This is yet another example of the maxim that 90% of the effort goes into the last 10% of a task.

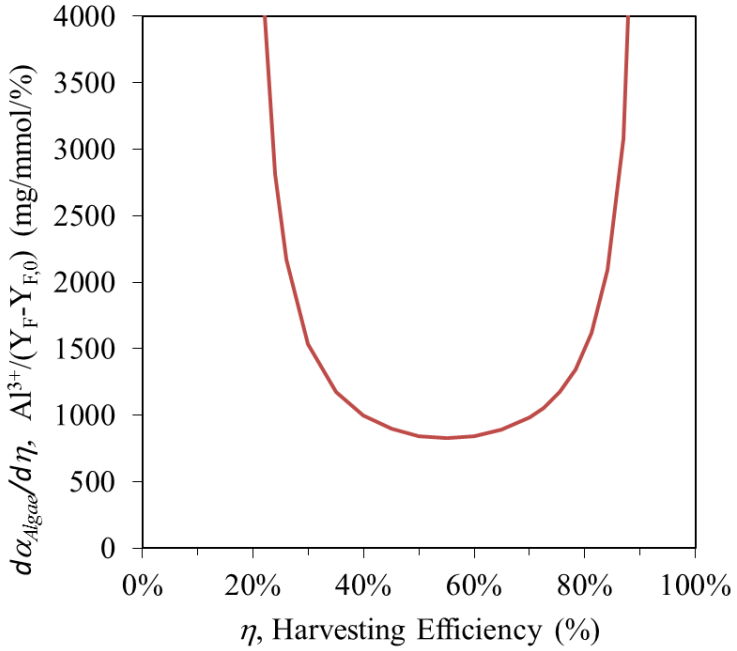

Figure 2. Marginal additional coagulant required to increase the efficiency based on correlation in Eq. (3).

A significant issue that was not addressed in the present project, but that has been addressed previously is the role of salinity in the effectiveness of various flocculants. Sukenik et al. [2] studied the effect of salinity and ionic strength on inorganic flocculants and inorganic flocculants combined with cationic polymers (see [15] for a related study focusing on cationic polymers). In saline waters with ionic strength of approximately 0.7 M the required dosage for $FeCl_3$ and $Al_2(SO_4)_3$ was five to ten times higher (higher required dosage for motile algae) than for freshwater species. The authors suggest that high ionic strengths (or high salt concentrations) interfere with inorganic flocculants by masking functionally active sites of metal hydroxides and by reducing the overall activity (activity coefficients) of the added flocculants. A linear relationship is found between the required dosage and the medium ionic strength [2]. At ionic strengths typical of desert brackish waters (I = 0.1 M) the inorganic flocculants do not lose much of their activity/effectiveness relative to their freshwater performance. Low concentrations of chitosan in conjunction with inorganic flocculants resulted in improved flocculation, but the chitosan needs to be added first. Adding on the order of 2 – 4 mg chitosan per liter significantly increased the effectiveness of the $FeCl_3$ [2]. Treatment with ozone also significantly increased the effectiveness of the inorganic flocculants in sea water; the authors ascribe this effect to reductions in cell motility and changes in cell surface characteristics.

2.2 PH DRIVEN AUTOFLOCCULATION

The large relative concentrations of flocculants required for harvesting algae suggest that inexpensive flocculants will be required. Because seawater and many brackish waters contains large quantities of calcium and magnesium, concentrations several times greater than the concentrations generally required for flocculation with iron or aluminum based flocculants, there has long been an interest in the use of these salts as flocculants, and this interest is supported by observed flocculation and separation at high pH where magnesium and calcium containing salts precipitate [14, 20, 31, 32, 53, 54]. This phenomenon has been referred to as autoflocculation since the photosynthetic consumption of carbon dioxide can lead to sufficiently increased pH where this autoflocculation has been observed to be driven by the algae themselves. Thus, algae can be induced to autoflocculate just by turning off the supply of carbon dioxide.

Ayoub et al. demonstrated algae flocculation in wastewater to which sea water (up to 20%) is added in conjunction with shifts in the pH (from pH of 9 to 11.5) [14]. They reached the conclusion that $Mg(OH)_2$ precipitation was driving the flocculation. In that and other work, $Mg(OH)_2$ precipitation has been found to be more effective that calcite precipitation [14, 53], even though calcite precipitation occurs in similar quantities over similar pH ranges.

Sukenik and Shelef studied the autoflocculation of seawater containing additional phosphate [32]. Under these conditions, autoflocculation associated with calcium phosphate (amorphous hydroxyapatite) is observed for pH > 8. The fact that this leads to the nutrient phosphate being removed from the culture media may not be desirable for algae cultivation (although this is a desirable consequence with waste water treatment).

The conditions over which autoflocculation occur depend on the water chemistry and also apparently on the species. The causes for the differences in flocculation behavior between algal species have not yet been identified. Given the variations in flocculation efficiency with differing algae strains, it is crucial to understand the interactions between flocculant and algae cells as well as solution conditions that provide the highest flocculation efficiencies for the algae strain selected for a given application. To this end, in Sec. 3 and Ref. [55] we discuss the predictions of the surface chemistry of precipitates of $Mg(OH)_2$, calcite and calcium phosphates in conjunction with the algae surface chemistry.

3 ALGAE AND PRECIPITATE SURFACE MODELING

The typically anionic algae surface charge is responsible for the stability of the algal suspension (resistance to flocculation) under natural growth conditions. In this work we have related the algal surface properties to the efficiency of flocculation [37, 38], and we have provided models for the change in surface state with water chemistry [55]. Further, the effectiveness of flocculants and other natural processes (i.e. bulk salt precipitation described in Sec. 2.2 on autoflocculation) depends on the surface state of precipitates. In Ref. [55] we provide models for the surface state of several precipitates relevant to autoflocculation.

Modeling of algae surface charge is complicated by the fact that algae surfaces are chemically heterogeneous mixtures of proteins and macromolecules and are parts of living cells out of equilibrium with adjacent fluids. Algal surface charge is apparently species-dependent but not phyla-dependent [56]. While there are subtle differences in the equilibrium constants and site densities between different species of algae [see e.g. Table 3 of 57] and bacteria, they are broadly similar and can be generalized.

Above pH ~ 4 - 5 algae surfaces are generally measured to be anionic; at lower pH they have a positive charge. pH and ionic strength-dependent algae surface charge is controlled by carboxylate, phosphate, and hydroxyl/amine groups which become deprotonated above pH 4 - 6 (carboxylic groups), pH 7 - 8 (phosphoric groups), and pH 9 - 10 (hydroxyl/amine groups). The observed shifts in net surface charge around pH ~ 4 – 5 reflect the predominance of carboxylate groups on the algal surface. The anionic algae surface charge effectively stabilizes many algal suspensions. Carboxylate and phosphate groups are able to sorb cationic species such as Ca^{+2} and Mg^{+2} and decrease their electrostatic repulsion from other algae, or they can attach to positively charged solid surfaces and cationic polymers. Coordination with cations, mineral precipitates, and cationic polymers, in particular, leads to algae flocculation. The conditions under which this occurs will depend upon fluid chemistry and the chemistry of the particular algae surface. Below we measure algae surface charge, algae flocculation with ferric chloride, and then develop a general model that links fluid chemistry to algae surface charge with a surface complexation model using the USGS chemical speciation code PHREEQC [58]. In Appendix A we provide an input file for PHREEQC that includes the appropriate parameters for algal surface modeling along with the solution phase and parameters for the surfaces of relevant precipitates.

3.1 MEASUREMENT OF ALGAE SURFACE CHEMISTRY

The titration method of Hadjoudja et al. [44] was used to measure *C. zofingiensis* surface charge. 100 mL algae samples were taken every 4 days, centrifuged 20 min at 500 G and then washed twice with 0.001 Na_2EDTA to remove adsorbed metals. Algae were subsequently rinsed 3 times with 0.1 M $NaNO_3$ and the volume brought up to 45 mL with 0.1 M $NaNO_3$. Suspension pH was lowered to around 3.0 using 0.1 M HCl and the suspension purged with N_2 for 10 min to remove CO_2. Samples were then titrated up to pH of 10 under N_2 protection using 0.1 M NaOH. 20 µL NaOH was added each time and the pH recorded after equilibrium; sample pH versus NaOH profiles are given in Figure 3. The titration process took 30~40 min. The volumes of algal suspensions before and after titration were recorded. Dry weights were measured after titration and the total algal biomass were calculated. The data were analyzed using Profit 2.1 [59].

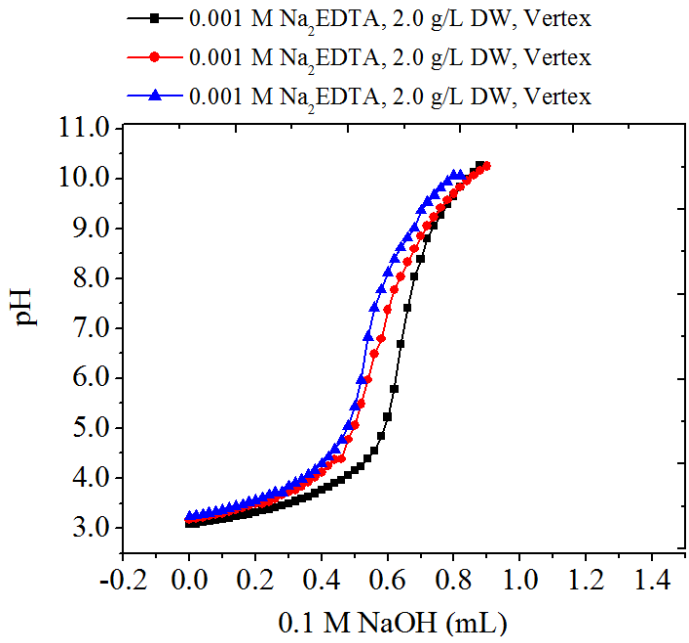

Figure 3. Representative surface titration results.

Hadjoudja et al. [44] fit their algae surface titration results with a Donnan Shell Model which assumes that a fraction of the surface potential exists beneath the algae-water interface. We use the same constants to predict surface charge using a diffuse layer model (DLM). The DLM is one of the simplest models of the electric double layer and envisions a surface layer with a pH-dependent surface charge and a Gouy-Chapman diffuse layer of counterions [see e.g. 60].

Figure 4 shows calculated carboxyl, phosphate, amine/hydroxyl abundances from measurements conducted during this project. These measured concentrations are for continuous growth conditions in a chemostat overflow. In the chemostat overflow a continuous supply of nutrients couples with a long residence time to provide one set of growth conditions that can be contrasted with batch cultivation described in the following paragraph. Results from our predictions of the surface state as a function of the surrounding fluid phase chemistry (pH and ionic concentrations) are reported in Refs. [37, 55]. These predictions describe the deprotonation of the reported functional groups along with the formation of complexes with abundant ions and flocculants.

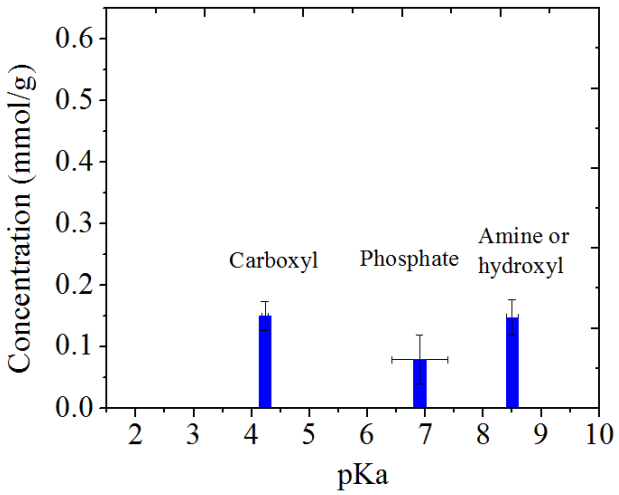

Figure 4. Measured functional group concentrations for C. zofingiensis under continuous growth conditions.

Measurements of surface functional groups was also carried out at Arizona State University within the context of this project under batch culture conditions. The nitrogen nutrient load was significantly reduced to induce nitrogen-starvation driven lipid production [13], giving growth conditions that typically result in a relatively high lipid fraction. Under these culture conditions, the growth moves rapidly through exponential to stationary and then declining growth. Concentrations of carboxyl, phosphate, amine/ hydroxyl groups were measured to decrease as the culture transformed from the exponential growth to declining phases, and this reduction in the surface functional group concentrations was found to be linearly correlated with the required flocculant for a given flocculation efficiency [13]. It is noteworthy that differences in growth stage and growth conditions lead to significant variations in the surface state. This sensitivity suggests that monitoring of the algal surface state in terms of the concentrations of functional groups as a function of growth conditions will be important in understanding the flocculation requirements. This represents an area where further study of varied species is required.

3.2 PREDICTING ALGAE AND PRECIPITATE SURFACE STATES

The algae surface charge varies with the ionic content of the water. To leading order, pH-dependent deprotonation leads to charges on surface functional groups. These functional groups also form complexes with other ionic species in the solution that alter the surface state. In Ref. [55] we provide models for the surface state of algal functional groups. We also provide models for the surface of key precipitates associated with bulk salts that are readily available in saline waters, namely brucite or $Mg(OH)_2$, calcium phosphate (hydroxyapatite) and calcite [55]. The equilibrium constants(log K's) associated with each surface complex are summarized in Table 3. -COOH, -POOH, and –NH represent respectively carboxyl, phosporyl and nitrogen base groups. For each surface reaction an equilibrium constant is defined as, for the example of carboxylate group deprotonation, $K = [\text{-COO}^-]\exp(-F\psi/RT)a_{H+}/[\text{-COOH}]$ where bracketed terms are surface concentrations (μmoles/m^2); F is Faraday's constant; ψ is the surface potential; a_{H+} is the activity of the hydrogen ion; R is the gas constant; T is absolute temperature.

Table 3. Diffuse layer model input parameters for the surfaces of algae, $Mg(OH)_2$, hydroxyapatite and calcite [55].

	Algae	25°C log K
1	$-COOH \leftrightarrow -COO^- + H^+$	-3.9
2	$-POH \leftrightarrow -PO^- + H^+$	-7.1
3	$-NH_2^+ \leftrightarrow -NH + H^+$	-9.0
4	$-COOH + Ca^{+2} \leftrightarrow -COOCa^+ + H^+$	-3.8
5	$-COOH + Mg^{+2} \leftrightarrow -COOMg^+ + H^+$	-3.5
6	$-COOH + Fe^{+3} \leftrightarrow -COOFe^{+2} + H^+$	-1.5
7	$-COOH + FeOH^{+2} \leftrightarrow -COOFeOH^+ + H^+$	-3.3
8	$-POH + Ca^{+2} \leftrightarrow -POCa^+ + H^+$	-0.6
9	$-POH + Mg^{+2} \leftrightarrow -POMg^+ + H^+$	-0.7
	$Mg(OH)_2$	
10	$>MgOH_2^+ \leftrightarrow >MgOH + H^+$	-10
11	$>MgOH \leftrightarrow >MgO^- + H^+$	-12
	Hydroxyapatite	
12	$>CaOH + H^+ \leftrightarrow >CaOH_2^+$	8.41
13	$>PO_3H_2 \leftrightarrow >PO_3H^- + H^+$	-1.11
14	$>CaOH + HPO_4^{-2} + H^+ \leftrightarrow >CaPO_4H^- + H_2O$	11.63
15	$>PO_3H_2 + Na^+ \leftrightarrow >PO_3Na^- + 2H^+$	-5.1
16	$>PO_3H_2 + Ca^{+2} \leftrightarrow >PO_3HCa^+ + H^+$	-0.7
17	$>PO_3H_2 + Mg^{+2} \leftrightarrow >PO_3HMg^+ + H^+$	-0.7
	Calcite Surface/ Solution Analogue	
18	**$>CaOH + H^+ \leftrightarrow >CaOH_2^+$**	**[a]11.8**
19	$Ca(OH)_2^{aq} + H^+ \leftrightarrow CaOH^+ + H_2O$	[a]11
20	**$>CaOH + H^+ + CO_3^{-2} \leftrightarrow >CaCO_3^- + H_2O$**	**17.1**
21	$Ca(OH)^+ + H^+ + CO_3^{-2} \leftrightarrow CaCO_3^{aq} + H_2O$	16.6
22	**$>CaOH_2^+ + SO_4^{-2} \leftrightarrow >CaSO_4^- + H_2O$**	**2.1**
23	$Ca^{+2} + SO_4^{-2} \leftrightarrow CaSO_4^{aq} + H_2O$	2.1
24	**$>CO_3H \leftrightarrow >CO_3^- + H^+$**	**-5.1**
25	$^cH_2CO_3^* \leftrightarrow HCO_3^- + H^+$	[b]-5.1
26	**$>CO_3H + Ca^{+2} \leftrightarrow >CO_3Ca^+ + H^+$**	**[c]-2.6**
27	**$>CO_3H + Mg^{+2} \leftrightarrow >CO_3Mg^+ + H^+$**	**[d]-2.6**
28	**$>CaOH_2^+ + HPO_4^{-2} \leftrightarrow >CaHPO_4^- + H_2O$**	**2.7**
29	$Ca^{+2} + HPO_4^{-2} \leftrightarrow CaHPO_4$	2.7
30	**$>CaOH_2^+ + HPO_4^{-2} \leftrightarrow >CaPO_4^{-2} + H^+ + H_2O$**	-5.3
31	$Ca^{+2} + HPO_4^{-2} \leftrightarrow >CaPO_4^- + H^+$	-5.3

Notes: [a]Derived from analogues by Pokrovsky and Schott [61] [b]$H_2CO_3^*$ denotes true H_2CO_3 – see pg. 150 of Stumm and Morgan [62]. [c]Adjusted to the value of Van Capellen et al. [63] to achieve lower Ca surface coverage. The total calcite site density is set to 8.22 μmol/m^2 split equally over >CaOH and $>CO_3H$ sites [61]. [d]Set equal to the Ca^{+2} sorption constant. All Aqueous log Ks and enthalpies came from the Lawrence Livermore National Laboratory thermo.com.V8.R6.230 thermodynamic database, with the exception of the H_2CO_3 deprotonation enthalpy, which came from Stumm and Morgan [62] and the enthalpies of $CaOH^+$, $MgHCO_3^+$, $CaHCO_3^+$ and $CaSO_4$ formation which were calculated from the Yucca Mountain Repository Program thermodynamic database (data0.ymp.r5d) values.

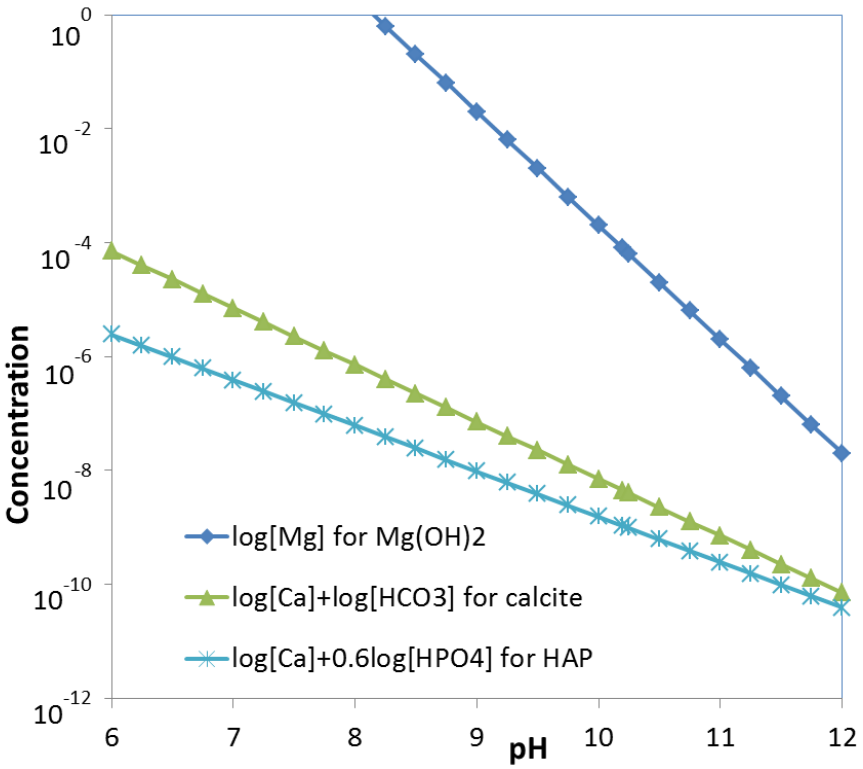

Figure 5. Concentrations for above which precipitation is expected for key brackish and saline water salts.

The parameters in in Table 3 are also included in the PHREEQC input file provided in Appendix A. This enables the prediction of combined algae and precipitate surface properties to identify favorable conditions for flocculation in saline and brackish waters. In Ref. [55] we discuss these favorable conditions for flocculation in the context of several experimental demonstrations of autoflocculation [14, 20, 32]. Also of relevance is the concentration range over which precipitates occur. In Figure 5 we plot the nominal ion concentrations above which precipitation is expected for key saline and brackish water salts.

3.3 BRACKISH AND SALINE WATER RESOURCES

A significant advantage of algae over other sources of biomass comes from its ability to grow in brackish and saline waters. In this section we briefly review some potential water resources that are not suitable for traditional agricultural uses. While the removal of algae from relatively dilute wastewaters is well understood, the controls over algae flocculation in saline/brackish water algal biofuels production settings is less clear. Saline waters have salt concentrations greater than 1,000 ppm and can exceed seawater salinities (35,000 ppm). Saline groundwaters in the US southwest, in particular waters of New Mexico, have been suggested as media for algal biofuels production. Saline groundwaters in the southwest are dominated by the salts of $CaSO_4$, NaCl, $CaCO_3$, $MgSO_4$, and silica. Figure 6 describes the compositions of New Mexico saline waters.

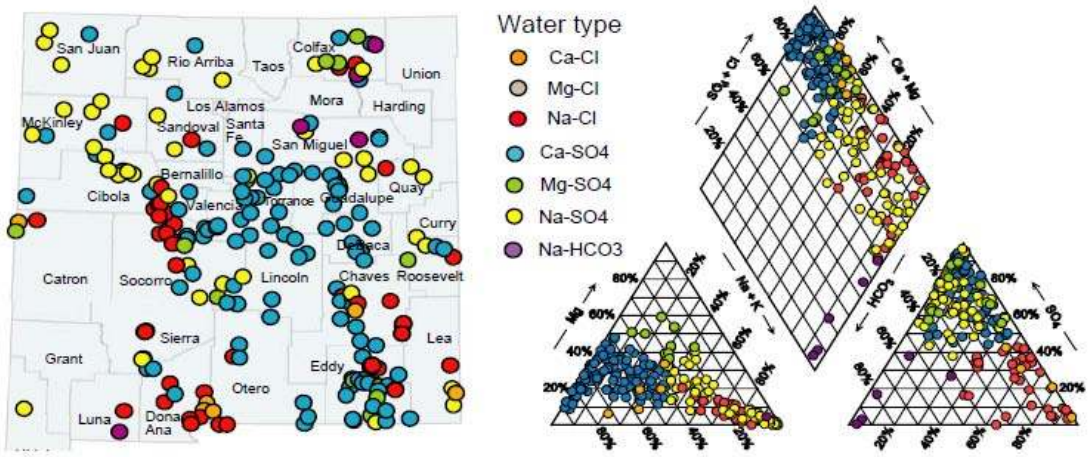

Figure 6. Piper diagram of New Mexico saline water types [from 64].

Waters are typically alkaline, having pHs ≥ 8. Silica levels often exceed ~ 30 ppm. When concentrated (e.g. for desalination to produce drinking water) past 120 ppm, amorphous silica scale (SiO_2) spontaneously precipitates. Waters are typically at, or very close to, saturation with respect to calcite ($CaCO_3$) and/or gypsum ($CaSO_4$:$2H_2O$). Like most groundwaters, their carbonate chemistry indicates equilibrium with CO_2 partial pressures ≥ 10 times atmospheric ($P_{CO2,atmospheric} = 10^{-3.5}$ atm.) Because inland brines are increasingly the target of drinking water desalination efforts, algal ponds may end up using reverse osmosis reject waters (desalination concentrates) or power plant cooling tower waters, which would each carry, in addition to high levels of the salts mentioned previously, anti-scalants as well. Table 4 provides representative water compositions of desalination concentrate and cooling tower water.

Table 4. Potential algal biofuel feedwater compositions (ppm except where noted). Desalination concentrate from [65], and cooling tower water analysis from 1/14/2010 analyses from SNL/CINT cooling tower water

	Desalination concentrate	Cooling tower water
SiO_2^{aq}	148	123
Na^+	2674	152
Ca^{2+}	589	163
Mg^{2+}	153	27
Cl^-	4699	105
SO_4^{2-}	1039	139
HCO_3^-	412	374
T	24°C	
pH	8.0	8.9

4 ALGAE FLOC STRUCTURE UNDER IN A SHEAR FLOW

4.1 INTRODUCTION

Wyatt et al. (2012) studied the flocculation behavior of a freshwater alga (*Chlorella zofingiensis*) that shows promise for biofuels production. They measured the effects of algae concentration, $FeCl_3$ flocculant concentration, and pH on the flocculation efficiency of the algae under quiescent conditions. They showed that for *C. zofingiensis* concentrations above 0.5 g/L, the concentration of $FeCl_3$ required for flocculation becomes independent of algae concentration. The change in this relationship is indicative of a change in the dominant flocculation mechanism which is marked by the presence of a critical floc density (i.e., number of flocs per unit volume). In the stoichiometric regime, increasing the algae concentration (and thus, the $FeCl_3$ concentration) results in the formation of a larger number of coagulated algae flocs. Increasing the algae and flocculant concentrations further leads to a point where the floc density is high enough (i.e., critical density) that they begin to interact with one another and form larger flocs. Once the large flocs are formed, they enmesh suspended algae and remove them as they settle. The formation of the larger flocs marks the change in flocculation mechanism from being dominated by coagulation by bridging to being dominated by sweep flocculation where the algae flocs sweep other suspended algae out of solution. Floc size and structure, therefore, determined the settling time and solids removal efficiency.

The rate of settling of a spherical particle is proportional to its density and to the square of its radius (or the cross-sectional area), according to Stokes' law. A non-spherical floc with branching arms has a lower effective particle density and a larger effective cross-sectional area, influencing the speed with opposite effects [66]. Furthermore, it has been reported that fractal aggregates of microspheres can be many times faster than Stokes' law predictions for a solid sphere with the equivalent volume [67]. Therefore, determination of the drag on flocs and the resulting differential settling rates that can lead to collisions and floc growth must include an understanding of the floc morphology. Most processes, however, do not rely on quiescent settling to induce flocculation and shear is present in commercial processing of algae. During shear the flocs are subjected to both aggregation and fragmentation brought on as the differential velocity in the region of interest either brings particles together or tears existing flocs apart. It is possible that flocs can break and reform resulting in restructuring with time. Eventually a steady state is reached.

The branching nature of a floc can be described in terms of fractal dimensions, a mathematical means of relating a characteristic dimension of the floc (say the perimeter) to the projected area. Many experimental and modeling studies exist of the influence of shear on the fractal dimensions of flocculating colloidal particles. Spicer and Pratsinis used approximately 1-micron-diameter polystyrene particles and an aluminum sulfate flocculant in a stirred tank to study the evolution of the floc structure with time [68]. They found that at high flocculant concentrations the steady-state floc size distribution was self-preserving with respect to shear rate; although, this was not true at low flocculant concentrations. They also observed that the average floc structure became less open (the fractal dimension changed) before attaining steady state due to restructuring. Spicer and Pratsinis also modeled the coagulation and fragmentation with a population balance model [69]. Serra et al. used polystyrene spheres in a NaCl aqueous solution sheared in a concentric cylinder Taylor-Couette device and found that, despite the fact that the final aggregate

size can depend on the primary particle concentration and the shear stress, no significant changes in the fractal dimensions occurred due to restructuring and that these dimensions remained unchanged for different values of the shear rate in the laminar region [70, 71]. More recently, Soos et al. looked at 10-micron-diameter polystyrene spheres in a Taylor-Couette device under turbulent conditions and showed that the time evolution of the particle cluster size distribution could be captured by standard population balance modeling [72]. They also examined the evolution with time of the perimeter fractal dimension; although, they destabilized the particles outside the Taylor-Couette apparatus and speculated that the shear experienced by pumping the dispersion into the apparatus caused significant restructuring. Selomulya et al. examined 60- to 810-nanometer diameter polystyrene spheres in both a Taylor-Couette device and a baffled stirred tank and measured the floc size and structure with small-angle light scattering [73, 74]. They found that flocs of the smaller particles were more prone to restructuring when compared with those made up of larger primary particles particularly at low to moderate shear rates. They performed a dimensional analysis to find a correlation among the particle properties (size, concentration, surface chemistry) and the steady-state aggregate properties (size and structure), showing that "larger or less dense flocs correspond to a stronger binding force or a lower level of applied shear." Wang et al. further examined floc strength by measuring the structure of alum-kaolin flocs with small angle laser light scattering at various agitation rates [75]. They concluded that strong, compact flocs play a key role in designing effective flocculation reactors and efficient water treatment. Furthermore, they noted distinction of fractal dimensions after breakage, inconsistent with self-similarity of aggregates noted by Spicer et al. [76].

Despite the interest in modeling coagulation in algae production or wastewater treatment there has been no studies looking systematically at the effects of shear on the size and structure of algal flocs where the effect of the flocculant concentration and pH are well documented in quiescent systems. Jarvis et al. looked at the effect of shear on fractal dimensions of natural organic matter using various coagulants and compared their results to model floc systems of monodisperse polystyrene particles [77]. Their results indicated that flocs formed with natural organic matter and iron precipitates were not dominated by pure charge neutralization as in the case of polystyrene/NaCl mixtures, but must include chemical bonds. Our intent is to extend the work of Ref. [37] to describe the effects of flow on *C. zofingiensis* in the presence of $FeCl_3$ and compare to a model system of polystyrene particles.

In the next section we describe the algae culture used, the flow device, image processing to determine floc size and structure, and the fractal analysis. The following section first defines the flow field through flow visualization and then through examination of a model polystyrene sphere system. Algal floc size distributions and floc fractal dimensions are reported next as functions of shear rate. In the last section we summarize our conclusions that our steady-state results for *C. zofingiensis* in the presence of $FeCl_3$ closely follow those obtained here and by others for charge neutralized polystyrene microparticles in shear environments.

4.2 MATERIALS AND METHODS

4.2.1 ALGAE CULTURE AND FLOCCULATION

A culture of *Chlorella zofingiensis* was obtained from researchers at Arizona State University and was grown in BG-11 growth media (Table 5) [78]. The culture was maintained in a chemostat under controlled conditions (e.g., light (12 hours light/12 hours dark), temperature,

etc.) and was continuously agitated by a magnetic stir bar and by bubbling air enriched with 1% carbon dioxide through the culture. Under these culture conditions, the algae are maintained in the log phase of the growth cycle at cell concentrations near 0.05 g/L dry weight [37].

Table 5. Composition of BG-11 growth media [78].

Component	Concentration (mM)
$NaNO_3$	17.6
K_2HPO_4	0.22
$MgSO_4 \cdot 7H_2O$	0.03
$CaCl_2 \cdot 2H_2O$	0.20
Citric Acid $\cdot H_2O$	0.03
Ammonium Ferric Citrate	0.02
$Na_2EDTA \cdot 2H_2O$	0.002
Na_2CO_3	0.18
Trace Metals	Cu, Mn, Zn, etc.

The *Chlorella zofingiensis* was flocculated by adding a quantity of ferric chloride (40% w/v solution obtained from Ricca Chemical Company, Arlington, TX) and adjusting the pH to 5-6 using 0.1 N NaOH or 0.1 N HCl, both obtained from Acros Organics (New Jersey, USA). All chemicals used were reagent grade. The flocculated algae suspension was then immediately introduced into the Couette apparatus. As soon as the algae suspension was introduced into the Couette, the rotation of the inner cylinder at a set speed was initiated. The total time between algae flocculation and the beginning of the cylinder rotation was approximately 30 seconds. The suspensions were then sheared for at least one hour at the lowest speeds and 30 minutes at the highest speeds before the floc structure was imaged.

4.2.2 COUETTE CELL

A concentric cylinder or Couette cell was constructed of clear acrylic for the experiments described here (Figure 7). The cell consists of an inner cylinder having a diameter of 9.2 cm which rotates inside an outer cylinder having an inner diameter of 10.1 cm. The annular gap in which the fluid is sheared is 0.9 cm. The entire apparatus is 53 cm tall. There are three sample ports located at heights of 7 cm, 27 cm and 47 cm from the bottom of the cell which allow for sample extraction during the experiment, if desired. There are also two viewing ports located 17 cm and 37 cm above the bottom of the device where a quartz window was mounted for better optical quality for visualization studies. The inner cylinder is rotated by an electric motor controlled by a programmable digital controller and can rotate at speeds ranging from 0.01 revolutions per second (rps) to 100 rps. The bottom of the inner cylinder sits atop a brass bushing which allows for relatively friction free rotation and minimizes heat generation during the experiment.

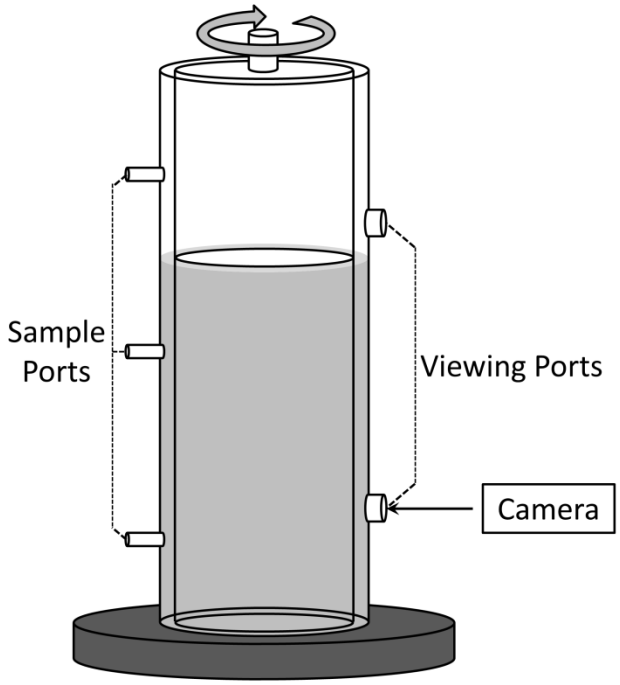

Figure 7. Schematic representation of the Couette cell used in the present study.

Floc images were obtained via a Phantom v9.1 high speed camera (Vision Research, Wayne, New Jersey) using a 20x Mitutoyo microscope objective attached to the lens. Lighting was provided from behind the Couette (facing the camera lens) so that the flocs imaged appear dark against a light background. Images were captured at a speed of 100 frames per second with a 10 µs exposure time.

4.2.3 IMAGE ANALYSIS

The images obtained from the test apparatus were analyzed using an image analysis script written in MatLab. The raw image intensity was first inverted (i.e., black changed to white, white changed to black) to make the remaining analysis simpler (Figure 8a). The background intensity was calculated using a moving average with a user specified disk size. Once calculated for the entire image, the background was then subtracted (Figure 8b). Next, the image was converted to a binary image using a user defined threshold intensity and the speckles of noise were removed (Figure 8c). Finally, using a user defined intensity gradient threshold, flocs that were blurry or out of focus were removed leaving only focused flocs to be analyzed (Figure 8d). The parameters of area, perimeter, and major axis length (length of the major axis of an ellipse fit to the floc) for each floc were then calculated and added to a data table. For each data set, a minimum of 1000 algae flocs were used in the analysis reported here.

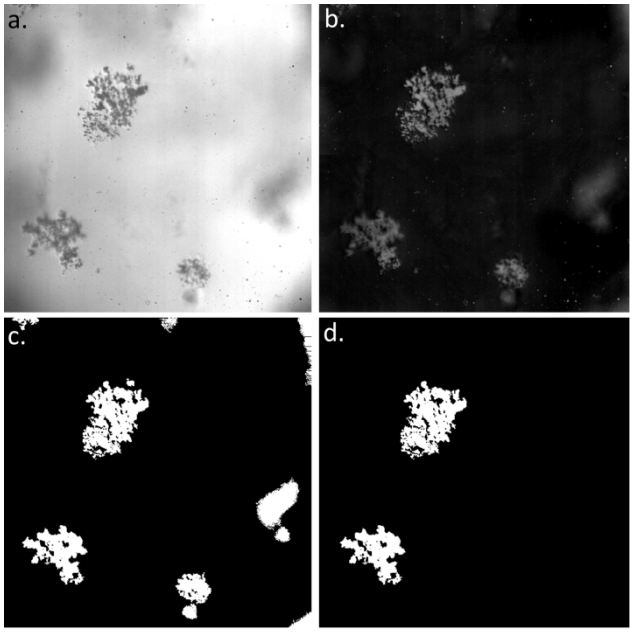

Figure 8. Example of image processing procedure showing the raw image (a.), inverted image with background subtracted (b.), binary image with noise removed (c.), and the final flocs that meet the sharpness criteria for analysis (d.).

4.2.4 FLOC FRACTAL ANALYSIS

The concepts of fractal geometry provide a mathematical means of describing the complex, irregular structure of particulate flocs. In fractal analysis, a characteristic dimension of the floc such as the perimeter (P) can be related to the projected area (A) of the floc by

$$P \propto A^{D_f/2} \tag{5}$$

where D_f is the perimeter-based fractal dimension of the floc. The value of D_f can be obtained by plotting the perimeter verses projected area of a distribution of flocs on a log-log plot. The slope of a line fit to the data will have a value of $D_f/2$ (Figure 9). The value of D_f will vary between 2 (a line) and 1 (a circle – the projected area of a solid sphere). Therefore, values of D_f closer to 2 are indicative of open, branched, and irregular floc structures while values closer to 1 indicate structures that are more densely packed.

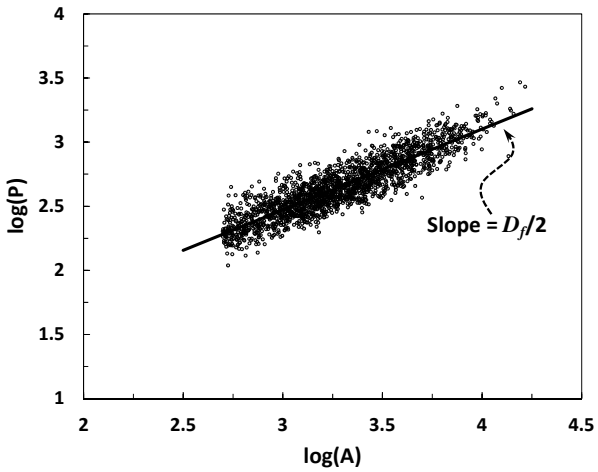

Figure 9. Determination of the fractal dimension (D_f) from the relationship between the floc perimeter and projected area.

The fractal structure of flocs can alternatively be described by one- and two-dimensional fractal dimensions [79-82]. A one-dimensional fractal dimension (D_1) can be determined from the relationship between the floc perimeter and the floc major axis length (l) by

$$P \propto l^{D_1} \tag{6}$$

Similary, a two –dimensional fractal dimension (D_2) can be determined from the relationship between the projected area of the floc and the major axis length by

$$A \propto l^{D_2} \tag{7}$$

As with the perimeter-based fractal dimension, D_1 and D_2 can be determined from log-log plots of the respective variables where a line fit to the data will have a slope of either D_1 or D_2. For a Euclidian object (e.g., circle), $D_1 = 1$. Values of $D_1 > 1$ indicate a structure whose perimeter increases faster than the object length scale resulting in a complex object outline. On the other hand, $D_2 = 2$ for a Euclidian object such as a circle. Values of $D_2 < 2$ indicate that the projected area of an object increases slower than the square of its characteristic length scale. As such, the projected area of larger objects is less than that of a Euclidian object of the same scale because of elongation or due to "holes" within the structure (i.e., flocs are not densely packed).

4.3 RESULTS AND DISCUSSION

4.3.1 TAYLOR-COUETTE FLOW VISUALIZATION

Flow patterns in the custom made Couette cell were visualized by filling the cell with Kalliroscope particles (AQ-1000) and tap water at room temperature. The cell was then run at a range of shear rates spanning those used in the floc structure experiments and images taken of the flow (Figure 10). At the lowest shear rates studied here, the flow in the cell is well within the wavy vortex regime typical of Taylor-Couette flow fields. As the speed of the inner cylinder is increased, the onset of turbulence is observed. At the highest speeds tested the flow transitions to be completely turbulent.

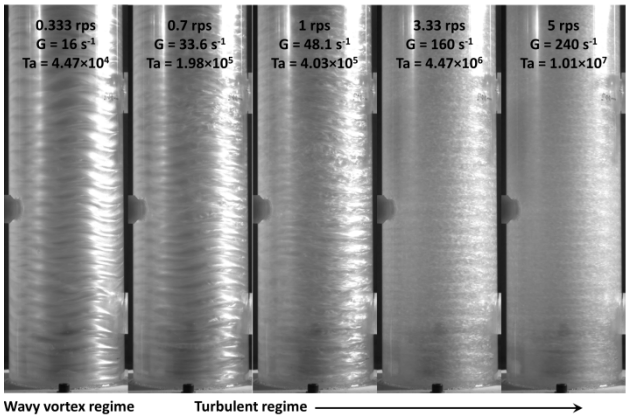

Figure 10. Images from a flow visualization study in the Couette cell used for the present study showing the wavy vortex regime, onset of turbulence, and fully turbulent regimes in a Couette flow.

4.3.2 IMAGING A TEST SYSTEM

Before studying algae floc structure in the Couette device, aggregation of 6 µm polystyrene particles in a 1.2 M NaCl solution was studied for comparison to published results. Sulfate latex particles having diameter of 6 µm were obtained from Life Technologies (Grand Island, NY). The particles were suspended in a 1.2 M NaCl solution at a volume fraction of 6.7 x 10^{-3} for the aggregation studies. Suspending the particles in a salt solution makes the particles neutrally buoyant as the salt solution density closely matches the density of the particles. Further, the salt molecules screen electrostatic charges between particles, which encourages aggregation.

Once made, the solution of particles was sonicated for 15 minutes to break up any aggregates formed. The solution was then carefully introduced into the Couette device in a manner than minimized the shear stress imparted to the fluid. The inner cylinder of the Couette began spinning at the desired speed immediately after the solution was introduced. The time between sonication of the particle solution and initiation of shear in the Couette was about 30 seconds. The absence of initial aggregates was confirmed visually with the Phantom camera at the beginning of each test. A sequence of images was then taken at specified time intervals to monitor the formation of the aggregates and enable an analysis of aggregate structure. The images were then analyzed using the method described above and the 2-dimensional fractal dimension calculated (Equation 3). For ease of comparison, the time dependence of the fractal dimension was examined in terms of a dimensionless time, t*, determined by

$$t^* = \phi t \gamma \tag{8}$$

where t is the time at which the measurement was taken, φ is the volume fraction of particles in solution, and γ is the applied shear rate. This allows the comparison of data taken at various shear rates and particle concentrations on similar terms.

Initially, there is a strong time dependence of the fractal dimension where the fractal dimension increases sharply (Figure 11). As time proceeds, the aggregates reach a steady state size and structure and the fractal dimension likewise reaches a steady state value that is independent with time. Similar trends were observed with other aggregate properties such as projected area, major axis length, and perimeter. These results agree well, both quantitatively and qualitatively with results reported by Refs. [68, 83] that also studied flocculation of polystyrene microspheres.

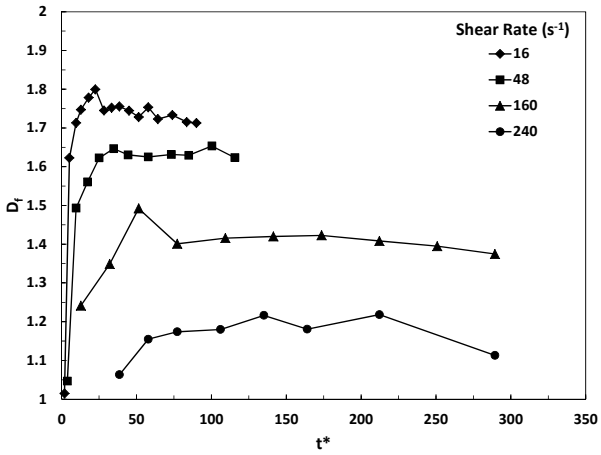

Figure 11. Time evolution of the fractal dimension of flocs composed of 6 µm polystyrene spheres in a 1.2 M NaCl solution at several shear rates.

As the shear rate is increased in the Couette device, the aggregate fractal dimension decreases (Figure 12). The added shear stresses in the fluid accompanying the higher shear rate cause the larger, higher fractal dimension aggregates to break up. Further, the aggregates begin to elongate in the direction of flow which results in a lower overall fractal dimension. Spicer and Pratsnis report a similar trend for the steady state average floc length with shear rate for polystyrene particles flocculated using alum [68]. The agreement between the present results obtained for polystyrene particles and those in the published literature give confidence in the experimental apparatus described here.

4.3.3 ALGAE FLOC SIZE DISTRIBUTIONS

Next, the floc size and structure of freshwater algae flocculated with ferric chloride at pH 5-6 was studied over a range of shear rates spanning from 30 s^{-1} to 240 s^{-1}. The distribution of floc sizes for all shear rates studied is lognormal in nature (Figure 13). At low shear rates, the distribution is quite broad and contains many very large flocs. As the shear rate is increased, the increased shear stress causes the large flocs to break up and the distribution sharpens around a smaller floc size.

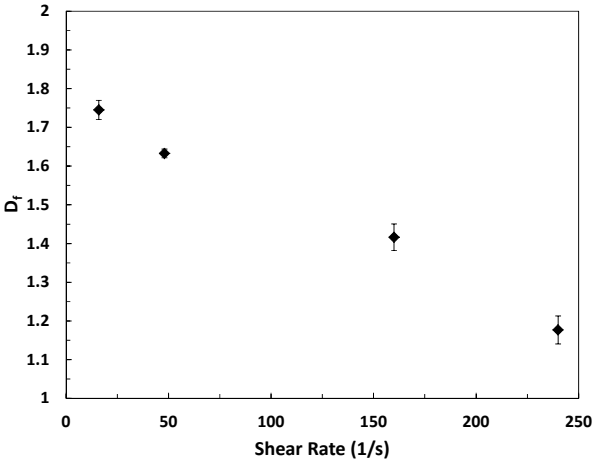

Figure 12. Shear rate dependence of the steady state fractal dimension for 6 µm polystyrene particles in 1.2 M NaCl solution.

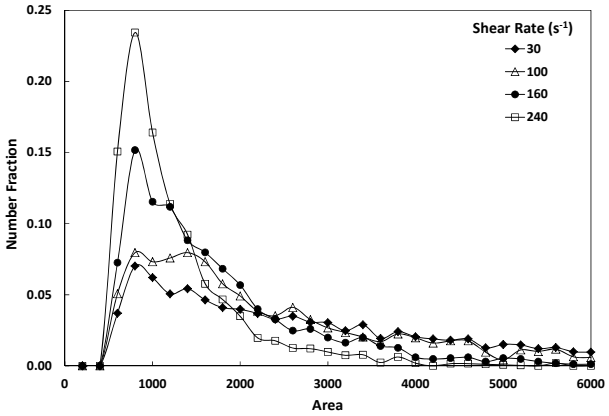

Figure 13. Algae floc size distributions for several shear rates ranging from 30 s^{-1} to 240 s^{-1} in a Taylor-Couette flow.

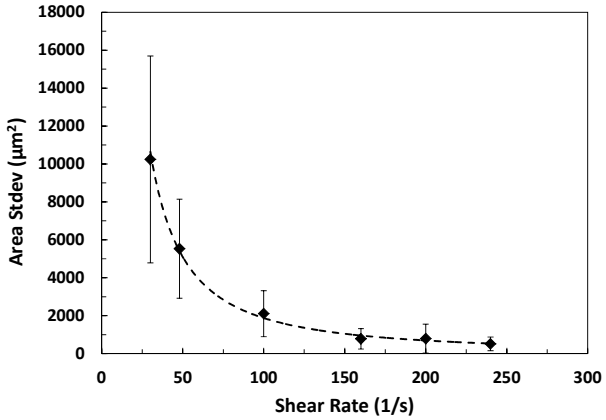

Figure 14. Standard deviation of the distribution of floc sizes as a function of shear rate in a Taylor-Couette flow. Error bars represent the error associated with the average of at least three measurements.

The shape of the floc size distribution can be further understood by examining the width of the distribution (i.e., the standard deviation) as a function of shear rate. This parameter gives a numerical value to the spread observed in floc sizes. A power law relationship is observed between the standard deviation of the floc size and the shear rate (Figure 14). At low shear rates, there is a strong dependence of the width of the distribution on shear rate. This means that small changes to the applied shear rate will have dramatic effects on the size distribution of the associated flocs. At high shear rates, however, the dependence is much weaker. In the region of high shear rates, the distributions are narrow and changing the applied shear rate has little effect on the resulting size distribution.

Next, the floc size distribution was examined in terms of a normalized floc size in the same manner as reported by [68]. If the floc size is normalized by the average floc size for each shear condition, the distributions collapse to a single curve (Figure 15). Shear has no effect on the shape of the distribution when normalized in this manner, which makes it self-preserving with respect to shear. Similar results have been reported for flocs of polystyrene particles with various flocculants [68, 70, 71]. The self-preserving nature of the floc size distribution is

important because it greatly simplifies the characterization of the steady state floc structure. For a steady state floc size distribution that is self-preserving with respect to shear, the entire distribution can be obtained once the average floc size is known (or estimated).

Further insight into the effect of shear on algae floc structure can be obtained by examining the largest floc present at each shear rate studied. The largest floc present at a given shear rate indicates the largest floc that is able to withstand the shear stresses of the flow field without fragmenting into smaller flocs. A power law relationship is observed between largest floc size and shear rate over the range studied here (Figure 16). The dependence is much stronger at low shear rates as the flocs are both larger and have a more branched structure. As the shear rate is increased, the additional shear stresses encountered by the flocs causes the flocs to fracture and restructure. The effects of fracture and restructuring are greatly diminished at the higher shear rates (i.e., there is a much weaker dependence of floc size on shear rate).

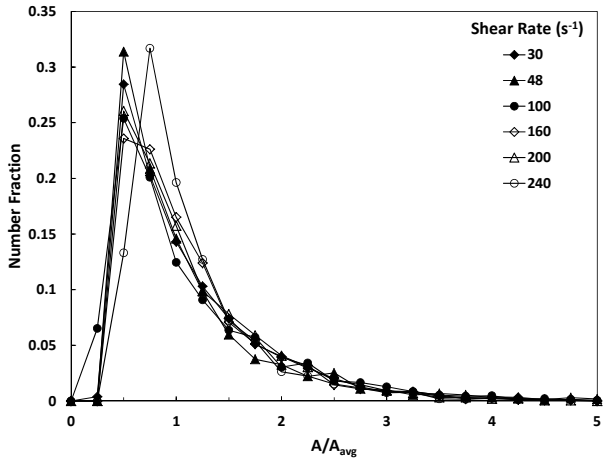

Figure 15. Normalized algae floc size distributions for shear rates ranging from 30 s^{-1} to 240 s^{-1}. Normalizing the floc size by the average floc size results in all curves collapsing to a single distribution curve.

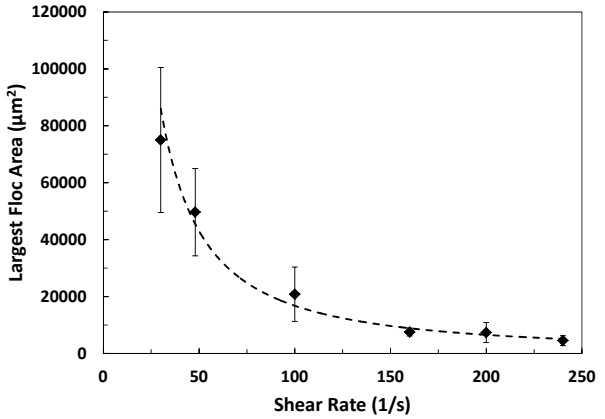

Figure 16. Larges algae floc as a function of shear rate in a Taylor-Couette flow. Points represent the average of at least three experiments and error bars represent one standard deviation.

4.3.4 ALGAE FLOC FRACTAL DIMENSION

The perimeter-based fractal dimension has a value of 1.34 at low shear rates and increases linearly to a value of 1.41 at the highest shear rate studied here (Figure 17). The relatively low value D_f indicates that the algae flocs are relatively densely packed structures that have some degree of irregularity and branching associated with them. As the shear rate increases, D_f also increases which indicates that the floc structure becomes elongated under the additional shear stresses of the Taylor-Couette flow.

The one- and two-dimensional fractal dimensions exhibit a power law dependence on shear rate over the range of shear rates studied here (Figure 17). At the lowest shear rate $D_1 = 1.28$ which indicates a structure whose perimeter increases faster than the floc length scale. Thus, the perimeter is more complex than a Euclidian object such as a circle due to irregular, branched floc structure. Further, the value of D_2 at the lowest shear rate is 1.83 which further supports the branched, irregular structure of the algae flocs. As the shear rate increases, both D_1 and D_2 decrease in a power law fashion until $D_1 = 1.14$ and $D_2 = 1.24$ at the highest shear rate. Under these shear conditions, the values of both D_1 and D_2 are much closer to those expected for a much less compact, elongated structure. These results are consistent with results of the perimeter-based fractal dimension.

Each of the fractal dimensions analyzed here provides complementary information in describing the structure of algae flocs in a Taylor-Couette flow. In summary, at low shear rates the algae flocs are large, relatively dense, branched structures. As the shear rate increases, the flocs are broken up and become elongated in the flow.

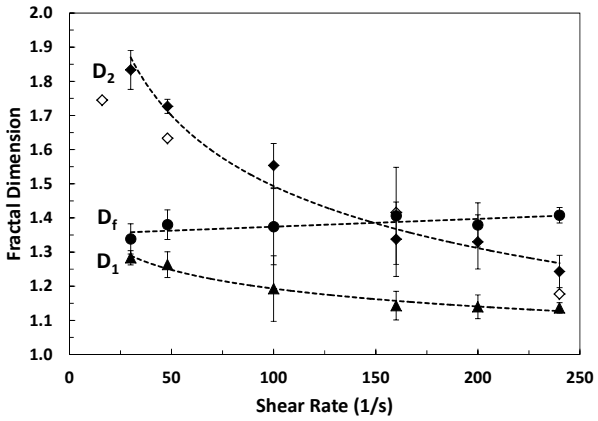

Figure 17. Fractal dimensions calculated for algae flocs as a function of shear rate in a Taylor-Couette flow. Data for 6 µm polystyrene microspheres is shown for comparison (open symbols).

4.4 CONCLUSION

The size distribution and structure of algae flocs are important as floc properties such as density and settling velocity are functions of the fractal dimension. These properties, in turn, effect the economics of the harvesting process for algal biofuels production.

Freshwater algae floc sizes and structures were measured in a Couette cell over a wide range of shear conditions. Flocs sizes are found to be lognormally distributed and narrow around smaller

floc size as the shear rate is increased. When examined in terms of a normalized floc size, the distributions for all shear rates collapse to a single curve. The self-preserving nature of the distribution means that, once a single parameter is known about the flocs (i.e., average floc size), the entire distribution can be predicted independent of shear rate. These results closely follow those obtained here and by others for polystyrene microparticles in shear environments.

Three fractal dimensions were calculated to characterize the floc structure as a function of shear rate. Low shear rates result in large, relatively densely packed flocs which break up and elongate as the shear rate is increased. This is evidenced by power-law decreases in the one- and two-dimensional fractal dimensions. Further, the perimeter-based fractal dimension increases linearly with increasing shear rate as the flocs elongated and assume a more complex perimeter.

5 POPULATION BALANCE MODELS FOR FLOC GROWTH AND BREAKAGE

The growth of flocs can be described in terms of an average floc size, but flocs are observed to vary in size over several orders of magnitude. Collisions and floc growth through differential settling require some differentiation in settling velocity that comes with accounting for differences in floc size. Further, the fraction of primary particles that do not become enmeshed in the largest flocs is an important component of separation efficiency. For this reason and others, it is beneficial to predict more of the size distribution than just its first moment. Here we discuss the use of sectional models [84] to describe the evolution of the floc size distribution.

5.1 POPULATION BALANCE EQUATION

The general particle balance equation (neglecting mass growth of individual particles) is

$$\begin{aligned}\frac{\partial n_v(v,t)}{\partial t}+\nabla\cdot\left(n_v\mathbf{v}\right)+\nabla\cdot\left(n_v\mathbf{c}_v\right)-\nabla\cdot\left(D_t\nabla n_v\right)&=\int_{v_0}^{v/2}\alpha(v-v',v')\beta_v(v-v',v')\;n_v(v-v',t)\;n_v(v',t)\;dv'\\&-n_v(v,t)\int_{v_0}^{\infty}\alpha(v-v',v')\beta_v(v,v')\;n_v(v',t)\;dv\\&-F(v)n_v(v)+\int_{v}^{\infty}f(v,v')F(v')n_v(v')dv'\end{aligned}\tag{9}$$

where n_v is the number density of particles of volume v, $\mathbf{c}_v$ is the velocity of particles of size v relative to the fluid velocity $\mathbf{v}$, $\alpha(v,v')$ is the sticking probability for particles of size v and v' and $\beta_v(v,v')$ is the collision frequency between particles of size v and v'. Fragmentation can also occur with a rate $F(v)$ and a distribution of fragments of size v from the breakup of a floc of size v' being $f(v,v')$.

Equation (9) can be written in terms of the number of primary particles in a floc, i. by noting that $v = iv_0$ where v_0 is the volume of the primary particle, a single algal cell. The general particle balance equation is then written

$$\begin{aligned}\frac{\partial n_i(i)}{\partial t}+\nabla\cdot\left(n_i\mathbf{v}\right)+\nabla\cdot\left(n_i\mathbf{c}_i\right)-\nabla\cdot\left(D_t\nabla n_i\right)&=\int_{1}^{i/2}\alpha(i-i',i')\beta_{net}(i-i',i')\;n_{i-i'}(i-i')\;n_{i'}(i')\;di'\\&-n_i(i)\int_{1}^{\infty}\alpha(i-i',i')\beta_{net}(i,i')\;n_{i'}(i')\;di'\\&-F(i)n_i(i)+\int_{i}^{\infty}f(i,i')F(i')n_i(i')di'\end{aligned}\tag{10}$$

where n_i is the number density of particles of volume iv_0, $\mathbf{c}_i$ is the velocity of particles of size i relative to the fluid velocity $\mathbf{v}$, $\alpha(i,i')$ is the sticking probability for particles of size i and i' and $\beta_{net}(i,i')$ is the collision frequency between particles of size i and i' including shear, differential sedimentation and any other relevant terms. Fragmentation can also occur with a rate $F(i)$ and a distribution of fragments of size i from the breakup of a floc of size i' being $f(i,i')$.

The description of the floc size in terms of the number of primary particles is based on the typically observed fractal scaling as described in Eqs. (74) and (75) of Sec. 9. This description will be important in the specification of the collision kernels.

The settling velocity for a fractal floc is proportional to the volume (or mass) divided by the fractal or cross section radius

$$\mathbf{c}_v = \frac{2(\Delta\rho) g i v_0}{9\mu r_f} = \frac{2(\Delta\rho) g v_0}{9\mu\left(\frac{3v_0}{4\pi}\right)^{1/3}} b^{1/D} i^{1-1/D}. \tag{11}$$

This description for the relative settling velocity does not account for the permeability of the floc. When there is permeability, the floc settling velocity can be much greater, and this is significant for flocs with small fractal dimensions, in particular for those with $D < 2$. A Brinkman viscosity approach to modeling the reduced drag associated with this increased permeability, but we do not account for this in the present work [67, 85].

5.2 COLLISION KERNELS

The rate of collision between flocs of size i and i' is given by the product of the collision kernel times the number densities of flocs of each size as indicated in Eq. (10). Relevant collision mechanisms for algae flocculation are shear and differential settling. Brownian diffusion is also relevant for submicron particles.

5.2.1 SHEAR-DRIVEN INTERACTIONS

The collision frequency kernel associated with laminar shear is

$$\beta_{sh}(i,i') = \frac{4\gamma}{3}\left(\frac{3v_0}{4\pi}\right)\left(\left(\frac{i}{b}\right)^{1/D} + \left(\frac{i'}{b'}\right)^{1/D'}\right)^3 \tag{12}$$

where γ is the rate of shear. This is an approximate scaling of the collision frequency with the floc radius cubed or with $i^{3/D}$. In turbulent flows, γ can be approximated as $(\varepsilon/\nu)^{1/2}$ where ε is the rate of turbulent energy dissipation and ν is the fluid kinematic viscosity. When considering jar tester configurations, the turbulent dissipation rate can be related to the impeller speed, Ω, and the jar test geometry through the power number, P_0, the jar volume, V, and the impeller diameter, d_{imp}, [40]

$$\varepsilon = \frac{P_0 \Omega^3 d_{imp}^5}{V} \tag{13}$$

The collision kernel given in Eq. (12) is referred to as the rectilinear kernel and does not take into account hydrodynamic interactions that tend to push flocs around each other. Li and Logan evaluated the relative collision frequency for fractal flocs under shear and empirically determined the correction associated with this hydrodynamic interaction [86, 87]. We employ a simplified correlation

$$\beta_{sh,fr} = \beta_{sh}(i,i')\left(\frac{r_{min}}{r_{max}}\right)^{0.785} \tag{14}$$

that indicates greater differences in the size of the floc lead to reduced collision frequencies. Evaluating the floc radii, r_{min} and r_{max}, in terms of the size i and i' with the prime denoting the smaller floc gives

$$\beta_{sh,fr}(i,i') = \frac{4\gamma}{3}\left(\frac{3v_0}{4\pi}\right)\left(\left(\frac{i}{b}\right)^{1/D} + \left(\frac{i'}{b'}\right)^{1/D'}\right)^3 \left(\frac{b}{b'}\frac{i'}{i}\right)^{0.785} \tag{15}$$

for the fractal floc shear collision kernel. If *i*' is the smaller particle the shear kernel scaling for collisions with large flocs (based on largest particle times the correction) is

$$\beta_{sh,fr}(i,i') \sim \left(\frac{i}{b}\right)^{3/D-0.785}\left(\frac{i'}{b'}\right)^{0.785}. \tag{16}$$

For spherical particles, the hydrodynamic correction is stronger due to reduced permeability, and Han and Lawler provide a correction referred to as the curvilinear kernel [88]. This is an adjustment to allow for particles to slide past each other along streamlines and the collision kernel is substantially reduced. We do not consider nonporous spherical flocs in the present work.

5.2.2 DIFFERENTIAL SETTLING-DRIVEN INTERACTIONS

The collision frequency for differential settling is given by the product of the difference in the settling velocity and the cross-sectional area

$$\begin{aligned}\beta_{ds}(i,i') &= \pi\left(\frac{3v_0}{4\pi}\right)^{2/3}\left(\left(\frac{i}{b}\right)^{1/D} + \left(\frac{i'}{b'}\right)^{1/D'}\right)^2 \left(\Delta c_v\right) \\ &= \frac{2\pi g}{9\mu}v_0\left(\frac{3v_0}{4\pi}\right)^{1/3}\left(\left(\frac{i}{b}\right)^{1/D} + \left(\frac{i'}{b'}\right)^{1/D'}\right)^2 \left|(\Delta\rho)b^{1/D}i^{1-1/D} - (\Delta\rho')b'^{1/D'}i'^{1-1/D'}\right|\end{aligned} \tag{17}$$

where we have allowed both the size and density of the separate particles to vary. The dependence of the kernel on the size is proportional to the size of the larger particle to the $(D+1)/D$ power: $i^{(D+1)/D}$; this is compared to the shear kernel where the dependence is to the $3/D$ power—roughly the same dependence.

As above, this is a rectilinear kernel. To account for the hydrodynamic interactions that tend to push small flocs out of the way of larger flocs, Li and Logan developed a correction for differential settling suitable for fractal flocs in analogy to Eq. (14) that reduces the collision frequency [87, 89]. As with Eq. (14) we employ a simpler correlation

$$\beta_{ds,fr} = \beta_{ds}(i,i')\left(\frac{r_{min}}{r_{max}}\right)^{0.984} \tag{18}$$

Evaluating the floc radii, r_{min} and r_{max}, in terms of the size *i* and *i*' with the prime denoting the smaller floc gives

$$\beta_{ds,fr}(i,i') = \frac{2\pi g}{9\mu}v_0\left(\frac{3v_0}{4\pi}\right)^{1/3}\left(\left(\frac{i}{b}\right)^{1/D} + \left(\frac{i'}{b'}\right)^{1/D'}\right)^2 \left(\frac{b}{b'}\frac{i'}{i}\right)^{0.984} \left|(\Delta\rho)b^{1/D}i^{1-1/D} - (\Delta\rho')b'^{1/D'}i'^{1-1/D'}\right| \tag{19}$$

Han and Lawler have also provided corrections to the collision kernels to describe the reduced collision efficiency for spherical particles in differential settling associated with particles sliding past each other along streamlines [88].

In general, in the present work we have used the collision kernels given in Eqs. (15) and (19).

5.3 BROWNIAN INTERACTIONS

For small particles, Brownian diffusion can lead to perikinetic coagulation. This is generally less significant for particles larger than one micron in water, but this is included here for completeness. The Brownian collision frequency is

$$\beta_B(i,i') = \frac{2kT}{3\mu}\left(\left(\frac{i}{b}\right)^{-1/D} + \left(\frac{i'}{b'}\right)^{-1/D'}\right)\left(\left(\frac{i}{b}\right)^{1/D} + \left(\frac{i'}{b'}\right)^{1/D'}\right) \tag{20}$$

where k is the Boltzmann constant and T is the temperature.

5.4 FRAGMENTATION KERNELS

Flocs that are subject to hydrodynamic forces can fragment. Hydrodynamic forces are generally expressed in terms of the shear as discussed in Sec. 5.2.1. Floc breakage can be broken into two main effects: (1) large-scale floc breakage assumed to be the result of tensile stress acting to split the floc into smaller flocs and (2) surface erosion where individual cells or small flocs are removed from the surface by shear stresses across the floc surface. This work will focus on large-scale floc breakage, also referred to as fragmentation, since this appears to be the significant mode of breakage. In particular, the self-similarity observed in the Couette flow data as reported in Figure 15 will only occur when fragmentation and not erosion is the dominant breakage mechanism.

Floc strength is often given in terms of the ratio of maximum or average particle sizes before and after a period of enhanced shear [90]

$$\frac{d_2}{d_1} = C\left(\frac{\gamma_2}{\gamma_1}\right)^{-a} \quad \text{or in terms of diameter dependence on shear} \quad C^{1/a} = \frac{\gamma_2}{\gamma_1}\left(\frac{d_2}{d_1}\right)^{1/a} \tag{21}$$

where d_1 is the initial diameter with shear γ_1, d_2 is the diameter after shear γ_2 is applied, C is a constant related to the floc strength and a is an exponent that gives the sensitivity of the floc breakage to the imposed shear. Both a and C are measures of overall floc strength. Typical values of a are in the range of 0.4 to 0.6 with some larger values reported.

There is evidence that the size of the turbulence microscale plays a role in the breakup mode [91], and there are theoretical arguments for different values of the exponent a in Eq. (21) with values of a = 0.5 suggesting fragmentation in the sub-Kolmogorov range being dominant [90, 92, 93], but in the present work we will treat this scaling as an unknown.

5.4.1 POWER LAW FRAGMENTATION KERNELS

There are at least two classes of fragmentation model. One model takes the general form

$$F(i)n_i(i) = k_F\gamma^b a_0\left(\frac{i}{b}\right)^a n_v(i) \tag{22}$$

where k_F is a breakage rate and b is related to a given above. The characteristic length scale of the floc over which the shear acts is $i^{1/D}$, but other exponents can appear as described below. As an example of this power-law fragmentation kernel, Flesch, Spicer and Pratsinis observed that b = 1.6, a = 1/D and k_F = 7e-4 gave good results in comparisons with their measurements [94].

The basic idea behind Eq. (22) is that fragmentation is limited by the frequency with which the shear stress, $\tau = \rho\nu\gamma$, acting on a floc exceeds the floc strength. There are several possible appraoches to describing the floc strength. Two possible lines of reasonaing will be given below, and a third is given in the subsequent subsection.

The force produced by this shear stress acting over the area of the floc is

$$\tau A_f = \pi a_o^2 \rho \upsilon \gamma \left(\frac{i}{b}\right)^{2/D} = \pi a_o^2 \rho \sqrt{\upsilon\varepsilon} \left(\frac{i}{b}\right)^{2/D} \tag{23}$$

We will assume here that this stress works against a *single set of bonds* that lead to a resistive force or floc strength like the product of the coordination number times a bond strength, $k_c F_B$. This leads to a breakage condition with $F_{sh} > k_c F_B$ corresponding to the dimensionless parameter

$$\gamma \left(\frac{i}{b}\right)^{2/D} \left(\frac{\pi a_o^2 \rho \upsilon}{k_c F_B}\right) > 1 . \tag{24}$$

where the greater than unity shows the conditions that favor breakage. Note that larger flocs are easier to break up, as are flocs with larger fractal dimensions and coordination numbers. A fragmentation kernel expression would include the shear rate to give the correct dimensions and any power, a_F, of the expression in Eq. (24)

$$\begin{aligned} F_F(i) &= A_F \gamma \left[\gamma \left(\frac{i}{b}\right)^{2/D} \left(\frac{\pi a_o^2 \rho \upsilon}{k_c F_B}\right) \right]^{a_F} \\ &= A_F \left(\frac{\pi a_o^2 \rho \upsilon}{F_B}\right)^{a_F} \frac{\gamma^{1+a_F}}{k_c{}^{a_F}} \left(\frac{i}{b}\right)^{\frac{2a_F}{D}} \end{aligned} \tag{25}$$

The shear stress is equivalent to an energy per volume, and we can develop an analogous expression for shear energy driven fragmentation. Instead of a bond force, a bond energy is introduced, dimensionally similar to the product of the force and particle length scale, $E_B \approx a_0 F_B$. The volume over which the shear energy acts is proportional to $(i/b)^{3/D}$ instead of the $2/D$ power appearing above. Alternative form of the breakage criterion is then written

$$\gamma \left(\frac{i}{b}\right)^{3/D} \left(\frac{\pi a_o^3 \rho \upsilon}{k_c E_B}\right) > 1 \tag{26}$$

that is very similar to equation (24), but with a different power, $3/D$ versus $2/D$, for the floc mass, i. As above, larger flocs are easier to break up, as are flocs with larger fractal dimensions and coordination numbers.

It is then possible to also write a power-law expression using Eq. (26) in analogy to Eq. (25), and this gives slightly different power dependence on the size

$$F_E = A_E\gamma\left[\gamma\left(\frac{i}{b}\right)^{3/D}\left(\frac{\pi a_o^3\rho\upsilon}{k_c E_B}\right)\right]^{a_E}$$
$$= A_E\left(\frac{\pi a_o^2\rho\upsilon}{F_B}\right)^{a_E}\frac{\gamma^{1+a_E}}{k_c{}^{a_E}}\left(\frac{i}{b}\right)^{\frac{3a_E}{D}}. \quad (27)$$

Since a_E and a_F are not determined by the physics provided here, it seems that there is no difference in the power law behaviors, just the requirement that the exponent on the shear rate be one greater than the exponent on i to give the proper rate dimensions.

5.4.2 EXPONENTIAL (ARRHENIUS) FRAGMENTATION KERNELS

The dimensionless parameter in Eq. (26) is written as a ratio of energies. If we think of this in analogy to chemical reaction rates where the shear energy takes the place of the temperature, an Arrhenius-like expression for the rate of breakage might be

$$F(i) = A_e\gamma\exp\left(-\left(\frac{k_c E_B}{\pi a_o^3\rho\upsilon}\right)\frac{1}{\gamma}\left(\frac{i}{b}\right)^{-3/D}\right). \quad (28)$$

A somewhat similar form was proposed in Ref. [91] where the dimensionless parameter is

$$\frac{32}{9}\frac{\pi a_0^2\tau}{\phi_f k_c F_B} > 1 \quad (29)$$

where the floc volume fraction, $\phi_f = b^{3/D} i^{\frac{D-3}{D}}$ from Eq. (78), is used along with the coordination number, k_c. Reference [91] provides an expression for the coordination number $k_c = 15\phi_f^{1.2}$ of unknown origin that significantly affects the kernel scaling with size. The fragmentation kernel in Ref. [91] is written

$$F(v)n_v(v) = \left(\frac{1}{15}\right)^{1/2}\exp\left(-\frac{9}{32}\frac{k_c\phi_f F_B}{\pi d_0^2\tau}\right)\gamma n_v(v). \quad (30)$$

Since d_f is related to i, the number of primary particles in the floc, by $d_f \propto (i/b)^{1/D}$, it is possible to estimate the relative magnitude of the floc size where fragmentation dominates as a function of the shear rate. This is done by expressing Eqs. (24), (26) and (29) in terms of the floc diameter. For Eq. (24) this suggests the scaling

$$d_f > \left(\frac{1}{\gamma}\frac{k_c F_B}{\pi\rho\nu}\right)^{1/2} \quad (31)$$

for fragmentation-dominated sizes while the scaling suggested by Eq. (26) is

$$d_f > \left(\frac{1}{\gamma}\frac{k_c E_B}{\pi\rho\nu}\right)^{1/3}. \quad (32)$$

Note that these are just based on dimensionless parameters and not precise values; a coefficient might vary significantly and is subsumed in the bond strength or energy here. For Eq. (29) the use of the floc volume fraction and the floc-volume-fraction-dependent coordination number gives a scaling

$$d_{frag} > \left(A \frac{F_B}{\gamma} \right)^{\frac{1}{2.2(3-D)}} \tag{33}$$

where we have lumped many parameters into the parameter A. The various exponents in Eqs. (31) to (33) can be compared with measured values of the exponent from Eq. (21).

5.5 TIME SCALES FOR POPULATION EVOLUTION

Using the kernels defined in the preceding sections in the right-hand side of Eq. (10) introduces certain time scales to the evolution. These time scales are the inverse of the product $\alpha\beta n$ for the collision kernels and the F for the fragmentation kernel. The characteristic time scales are those obtained by factoring out the size dependence and using the primary particle volume and initial particle volume fraction, ϕ_0, to provide a characteristic number density. The shear and differential settling time scales are

$$\tau_{sh} = \frac{\pi}{\alpha\gamma v_0 \phi_0} \text{ and } \tau_{ds} = \frac{9\mu}{2\pi\alpha\left(\Delta\rho\right) g \phi_0 a_0}. \tag{34}$$

The ratio of these time scales gives the approximate relative importance of shear-driven and differential-settling driven (subject to correction according to the size scaling of each mechanism). The relative importance of differential settling compared to shear is characterized by

$$R_{ds} = \frac{\tau_{sh}}{\tau_{ds}} = \frac{\pi\left(\Delta\rho\right) g}{6\mu\gamma a_0^2} \tag{35}$$

Written in terms of these time scales the integrals in Eq. (10) involve dimensionless size distributions normalized by the initial number of primary particles per volume. An integral involving Eq. (15) is written

$$\int_1^\infty \alpha\beta_{sh}(i,i')\, n_{i'}(i')\, di' = \frac{1}{N_0\tau_{sh}} \int_1^\infty \left(\left(\frac{i}{b}\right)^{1/D} + \left(\frac{i'}{b'}\right)^{1/D'} \right)^3 \left(\frac{b}{b'}\frac{i'}{i} \right)^{0.785} di' \tag{36}$$

and the similar integral involving Eq. (19) is written

$$\int_1^\infty \alpha\beta_{ds}(i,i')\, n_{i'}(i')\, di' = \frac{1}{N_0\tau_{ds}} \int_1^\infty \left(\left(\frac{i}{b}\right)^{1/D} + \left(\frac{i'}{b'}\right)^{1/D'} \right)^2 \left(\frac{b}{b'}\frac{i'}{i} \right)^{0.984} \left| \left(\Delta\rho\right) b^{1/D} i^{1-1/D} - \left(\Delta\rho'\right) b'^{1/D'} i'^{1-1/D'} \right| di'. \tag{37}$$

(Recall that i' is specified to be smaller than i in Eqs. (15) and (19).)

5.6 CHARACTERIZING SIZE DISTRIBUTIONS

The distribution $n(i)$ can be characterized in terms of its moments

$$M_0 = \int_1^\infty n(i)di, \quad M_1 = \int_1^\infty in(i)di, \quad M_r = \int_1^\infty i^r n(i)di. \tag{38}$$

The zeroth and first moments are related to the total number of particles and the total volume of particles, for example. Some terms involve fractional moments. For example, the rate of differential settling is shown by Eq. (11) to depend on the $1-1/D$ moment. If we introduce the settling velocity of a primary particle as

$$\mathbf{c}_0 = \frac{2(\Delta\rho)gv_0}{9\mu a_0} \tag{39}$$

the settling flux term can be written

$$\nabla\cdot\left(\int_1^\infty n_i\mathbf{c}_i\right) = \nabla\cdot\left(\mathbf{c}_0 b^{1/D} M_{1-1/D}\right) . \tag{40}$$

Integrating over the distribution *n(i)* for Eq. (10) yields

$$\frac{\partial M_0}{\partial t} + \nabla\cdot\left(M_0\mathbf{v}\right) + \nabla\cdot\left(\mathbf{c}_0 b^{1/D} M_{1-1/D}\right) - \nabla\cdot\left(D_t\nabla M_0\right) = -\frac{1}{2}\int_1^\infty\int_1^\infty \alpha(i,j)\beta_{net}(i,j)\, n_i(i)\, n_j(j)\, di\, dj \tag{41}$$

where terms that have more complex dependencies on the size distribution are left as integrals for now. Eq. (41) describes the evolution of the number of particles or flocs and the right-hand side predicts the reduced number of flocs resulting from agglomeration. Multiplying Eq. (10) by *i* leads to an equation that is related to the total volume of the flocs. This is a conserved quantity when no particle growth is included and the right-hand side of such a transport equation is zero.

For the simplest forms of the shear collision kernel (where there is no absolute value or specified smaller floc size), it is possible to express the right-hand side terms in terms of a sum of fractional moments. For example, the right-hand side of Eq. (41) with the rectilinear shear kernel is

$$-\frac{1}{2}\int_1^\infty\int_1^\infty \alpha(i,j)\beta_{net}(i,j)\, n_i(i)\, n_j(j)\, di\, dj = -\frac{\left(M_{3/D} + 3M_{1/D}M_{2/D}\right)}{N_0\tau_{sh}b^{3/D}} \tag{42}$$

where $N_0 = M_0(t = 0)$. The fractional moments can be evaluated from the whole moments by interpolation (in the logarithms of the moments), and this is the basis of the method of moments with interpolative closure [95].

5.7 SECTIONAL MODEL

Equation (10) is an integro-differential equation that can be solved numerically in a variety of ways. At one level, discussed separately, moments of the floc size distribution can be evolved. Knowledge of a sufficient number of moments will provide the necessary details regarding the evolution of the size distribution, but writing closed equations for moments has its own challenges that have been addressed in several ways [84, 95, 96]. Among other goals in the present work, we seek to understand the differing behavior of large and small flocs in order to understand flocculation efficiency. To this end, we discretize the distribution following the approach first rigorously derived by Gelbard and referred to commonly as the sectional method [84]. Following Gelbard, we introduce a conserved quantity, *q*, the net volume of primary particles in the present case, and make the assumption that it can be factored it into a time-dependent and size-dependent term, $\overline{q}(t)$ and *f'(i),*

$$q(i,t) = iv_0 n_i(i,t) = \overline{q}(t) f'(i) v_0 . \tag{43}$$

The quantities q and f are discretized across the size domain into m sections. The discretization is geometric with a factor of two in volume separating successive sections, and the centers of the sections are at $i = 2^l$ for the l-th section with l ranging from zero to an upper bound that needs to be large enough to track the mass of the largest flocs. To describe the discretization of the sections, we define the values of i at the upper bound of the l-th section to be $i_l = 2^{l+0.5}$, and the lower bound, $i_{l\text{-}1}$, is one half of this. With Eq. (43) integrated across sections from $i_{l\text{-}1}$ to i_l the integrated volume within a section is

$$Q_l(t) = \int_{i_{l-1}}^{i_l} q(i,t)di = \overline{q}(t)v_0 \int_{i_{l-1}}^{i_l} f'(i) = \overline{q}(t)v_0\left[f(i_l) - f(i_{l-1})\right]. \tag{44}$$

This is the total volume (per volume of the fluid) contained in flocs of sizes between $i_l = 2^{l\text{-}0.5}$ and $i_l = 2^{l+0.5}$. In terms of Q the number distribution is

$$n_i(i,t) = \frac{Q_l(t)f'(i)}{iv_0\left[f(i_l) - f(i_{l-1})\right]} = \frac{Q_l(t)}{iv_0\sqrt{2}\left(2^l - 2^{l-1}\right)} \tag{45}$$

An assumption is made as to the functional form of *f(i)* that differentiates implementations of this model; in the present work, we define *f(i) = i* leading to volume distribution, q, assumed to be constant across each section and the number distribution to be declining as seen in Eq. (45). The uncertainties in the parameters appearing in Eq. (10) at this point are much larger than the uncertainties introduced through different forms for *f(i)* so that we do not address this further at this point.

The sectional model is developed by identifying all combinations from Eq. (10) that lead to changes in q. This is described in detail in Ref. [84], and here we provide the results breaking the collision contributions to the section in a manner that is similar to that of Gelbard as provided in Eq. (19) and Table II of Ref. [84]. The form provided here is limited to geometrically spaced sections with $i_l \geq 2i_{l-1}$; this discretization leads to considerable simplifications because collisions between small sections have a limited impact on larger sections. The contributions of collisions to the changes in the sections, the first and second terms on the right-hand side of Eq. (10), is

$$\begin{aligned}\frac{dQ_l}{dt} = &\frac{1}{2}Q_{l-1}\sum_{j=1}^{l-1} {}^1\overline{\beta}_{j,l-1,l}Q_i - Q_l\sum_{j=1}^{l-1} {}^2\overline{\beta}_{j,l,l}Q_i \\ &-\frac{1}{2}{}^3\overline{\beta}_{l,l,l}Q_l^2 - Q_l\sum_{j=l+1}^{m} {}^4\overline{\beta}_{j,l,l}Q_j\end{aligned} \tag{46}$$

The terms on the right-hand side represent, in order, the addition of primary particles to section l by agglomeration of smaller section flocs, agglomeration of smaller section flocs with section l, agglomerations within section l that lead to formation of larger flocs and agglomerations between section l and larger flocs that also contribute to larger sections. Expressions for the collision kernels integrated over the sections are given in Table 6. The first and second indices indicate the values of Q_l that the collision kernel is multiplied by and the third index indicates the section to which that term contributes.

Table 6. Integrated collision kernels for the case where sections are geometrically discretized with $i_l \geq 2i_{l-1}$.

Symbol	Range of sections	Expression

${}^{1}\overline{\beta}_{j,l-1,l}$	$2 \le l \le m$ and $j < l-1$	$\frac{1}{i_{j-1} i_{l-2}} \int_{i_{j-1}}^{i_j} \int_{i_{l-1}-i}^{i_{l-1}} \frac{(i+i')\beta(i,i')}{ii'} di' di$
${}^{1}\overline{\beta}_{l-1,l-1,l}$	$2 \le l \le m$ and $j = l-1$	$\frac{1}{2i_{l-2}^2} \int_{i_{l-2}}^{i_{l-1}} \int_{i_{l-2}}^{i_{l-1}} \frac{(i+i')\beta(i,i')}{ii'} di' di$
${}^{2}\overline{\beta}_{j,l,l}$	$2 \le l \le m$ and $j < l$	$\frac{1}{i_{j-1} i_{l-1}} \int_{i_{j-1}}^{i_j} \int_{i_l-i}^{i_l} \frac{\beta(i,i')}{i} di' di$ $- \frac{1}{i_{j-1} i_{l-1}} \int_{i_{j-1}}^{i_j} \int_{i_{l-1}}^{i_l-i} \frac{\beta(i,i')}{i'} di' di$
${}^{3}\overline{\beta}_{l,l,l}$	$1 \le l \le m$	$\frac{1}{2i_{l-1}^2} \int_{i_{l-1}}^{i_l} \int_{i_{l-1}}^{i_l} \frac{(i+i')\beta(i,i')}{ii'} di' di$
${}^{4}\overline{\beta}_{j,l,l}$	$1 \le l \le m$ and $j > l$	$\frac{1}{i_{j-1} i_{l-1}} \int_{i_{j-1}}^{i_j} \int_{i_{l-1}}^{i_l} \frac{\beta(i,i')}{i} di' di$

The summations of the collision kernels over Q_i in Eq. (46) can be thought of as integrals of these collision kernels over the floc size distribution. Interpreted in this respect, the first term on the right hand side is the effect of the integral of the collision kernel over smaller sections times $Q_{l\text{-}1}$. The remaining terms represent the effect on Q_l of the collision kernel integrated across the complete distribution times Q_l. Since the magnitude of Q_l varies dramatically over the size distribution, it is sometimes helpful to think of the sectional equations in terms of the fractional change in the section. Dividing Eq. (46) by Q_l, we obtain the evolution equation for the fractional change

$$\frac{d(\ln Q_l)}{dt} = \frac{1}{2}\frac{Q_{l-1}}{Q_l}\sum_{j=1}^{l-1} {}^{1}\overline{\beta}_{j,l-1,l} Q_j - \sum_{j=1}^{l-1} {}^{2}\overline{\beta}_{j,l} Q_j - \frac{1}{2} {}^{3}\overline{\beta}_{l,l} Q_l - \sum_{j=l+1}^{m} {}^{4}\overline{\beta}_{j,l} Q_j \tag{47}$$

In Figure 18 and Figure 19, we have plotted the collision kernels for various parameter ranges. Each figure contains six subplots with rows corresponding to the shear, differential settling and orthokinetic collision kernels, respectively. The shear and differential settling kernels are plotted for unity shear rates (γ = 1/s) and unity differential density ($\Delta\rho$ = 1 g/cm^3). The left-hand column of figures shows the kernel for the growth in a column associated with collisions between smaller flocs; this corresponds to ${}^{1}\overline{\beta}_{i,l-1,l}$. The right hand column contains the combination of ${}^{2}\overline{\beta}_{i,l}$ through ${}^{4}\overline{\beta}_{i,l}$ that describes the addition of removal of mass from section l associated with collisions with all floc sizes. Note that a part of the integrals of ${}^{2}\overline{\beta}_{i,l}$ and ${}^{3}\overline{\beta}_{i,l}$ lead to growth in section l while a portion of those integrals lead to flux from section l to larger sections. For the largest section in the model, flux of mass to larger sections is not allowed (leading to an accumulation of mass in the largest section) so that the terms describing the flux to larger sections are set to zero. In the figures, the right-hand column collision kernels show generally negative contributions except for the top row where the contribution is positive because of this prohibited flux to non-existent sections described in the previous sentence. The fact that the

right-hand column collision kernels generally have negative net contributions shows that most collisions with aggregates in section *l* (including those with larger aggregates) lead to a flux to larger sections.

Figure 18 shows the collision kernels for so-called rectilinear collisions. The rectilinear collision kernel ignores the effect of hydrodynamic repulsion that is associated with the need to remove fluid between particles as they approach. It has been shown that for spherical particles, the hydrodynamic repulsion leads to sharply reduced collision frequencies, in particular when the particles are of different size. Analytical studies of the collision frequencies for spherical particles have led to so-called curvilinear collision kernel models that reduce the collision frequencies according to [88]. The curvilinear collision kernels are based on spherical particles, but the fractal flocs of interest here are porous and permeable. This porosity/permeability allows some flow through the aggregate and reduces the hydrodynamic repulsion. The need to accurately treat interactions of fractal aggregates has led to a number of models for collision kernels for permeable flocs. We have used Eqs. (15) and (19) and refer to this model as the fractal collision kernel here; values are plotted in Figure 19. In comparing the fractal collision kernel with the rectilinear kernel of Figure 18, there is appreciable narrowing of the effective range of collisions. However, this narrowing is not as strong as the narrowing associated with the curvilinear collision kernel as is seen in Figure 20 where all three approaches are plotted for collisions with one size floc. The fall-off in the collision frequency away from the same-size collision is substantially stronger for the curvilinear kernel. Quantitatively, the fractal collision kernel is reduced by roughly one order of magnitude over a range of ten sections (2^{10} in floc mass) at this fractal dimension of 2.33. This is compared to the curvilinear kernel where the collision rate is reduced by one order of magnitude over a range of roughly five sections (2^5 in floc mass).

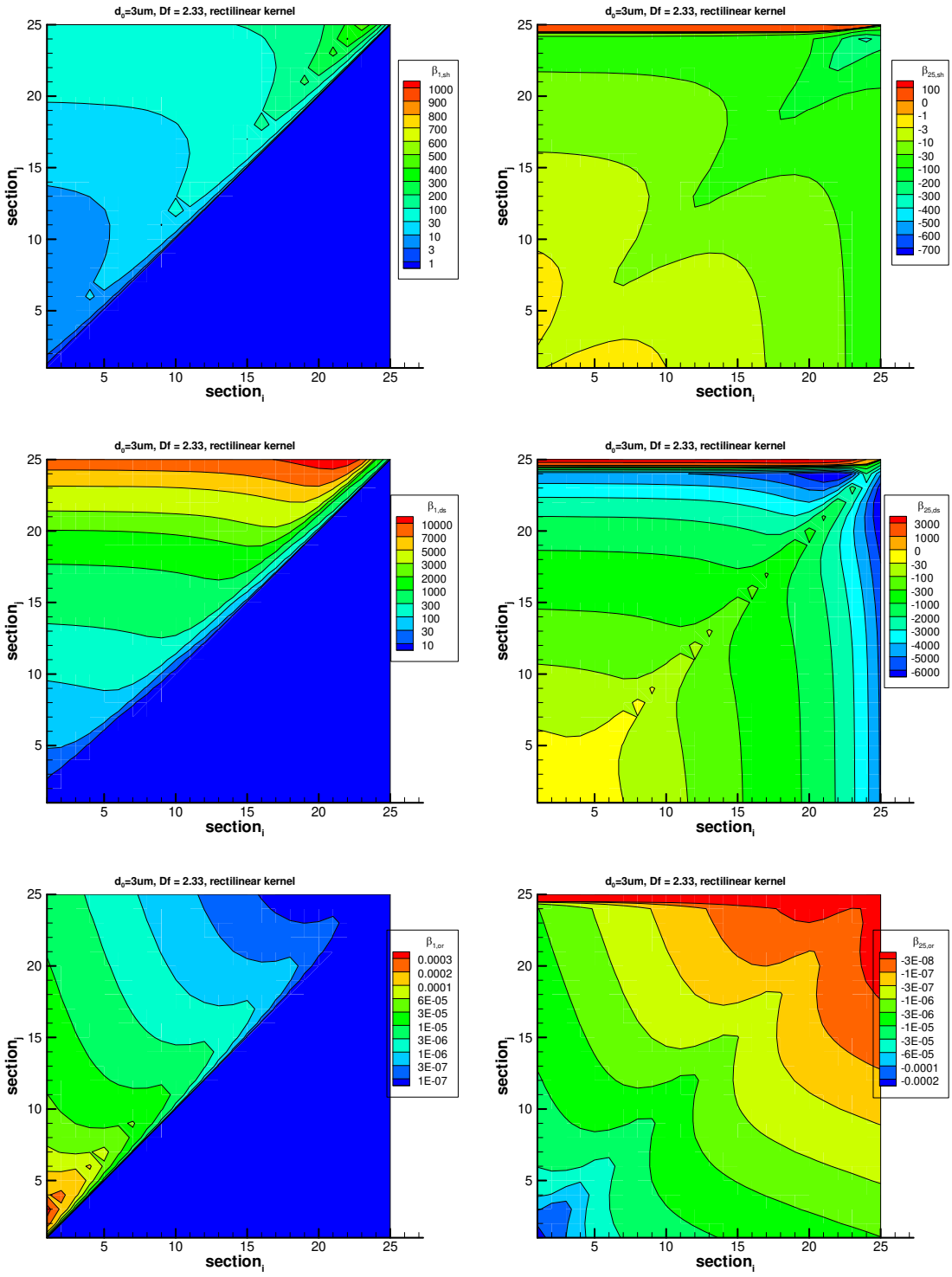

Figure 18. Collision kernels for fractal aggregates with Df = 2.33, primary particle size of 3 um, with rectilinear collisions assumed. Kernels associated with shear, differential settling and Brownian motion are plotted in the top, middle and bottom rows, respectively.

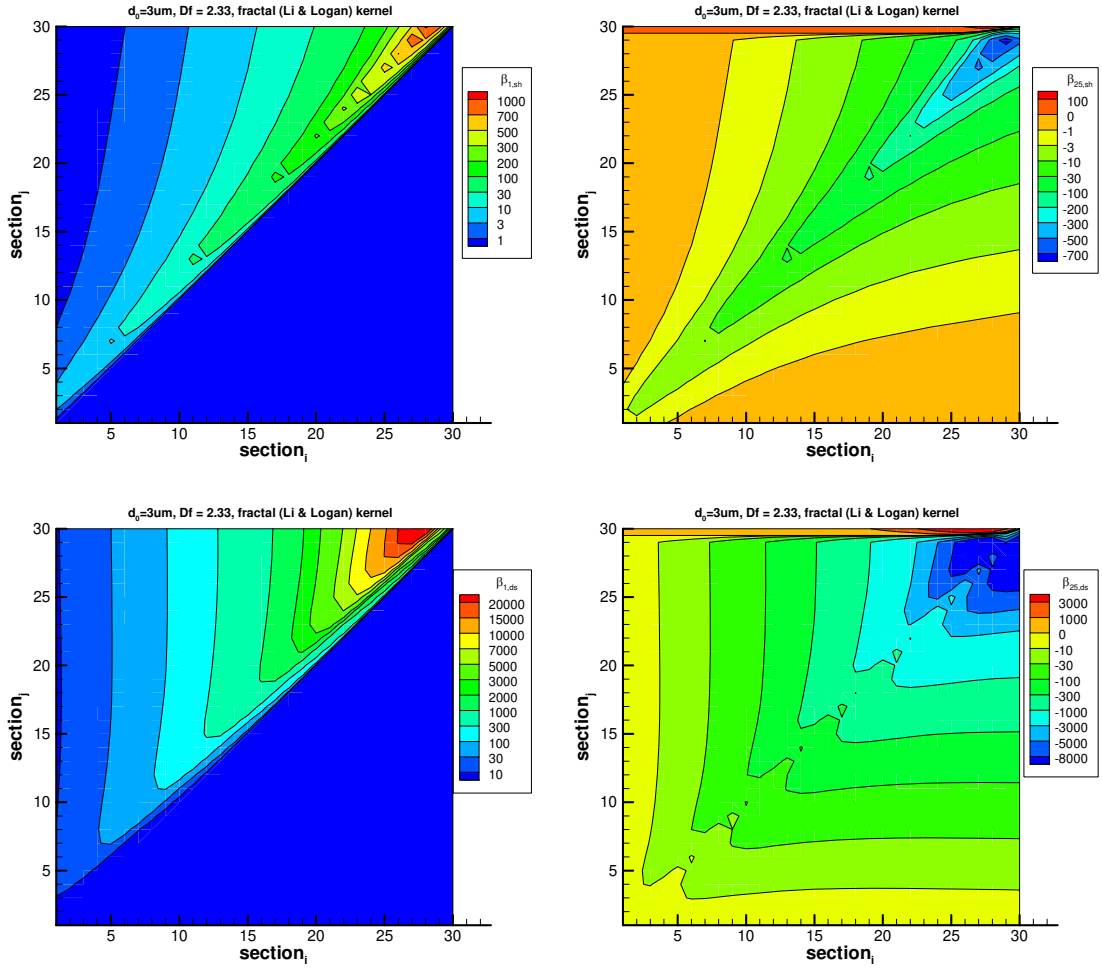

Figure 19. Collision kernels for fractal aggregates with Df = 2.33, primary particle size of 3 um, with Li and Logan adjustment to collision frequency.

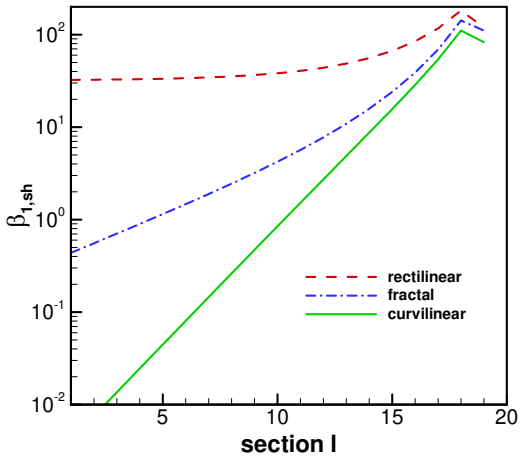

Figure 20. A comparison of collision kernels for shear aggreagation with fractal aggregates with Df = 2.33, primary particle size of 3 um, and shear rate of 1/s.

5.8 FLOC GROWTH WITH THE SECTIONAL MODEL

Here we present some basic results for floc growth without fragmentation using the sectional model as described in Eq. (46). Figure 21 shows the early growth under shear with the collision kernels evaluated from Eq. (15). The growth is expressed as one less than the average floc size following the discussion in Sec. 7.3 (c.f. Figure 29). These simulations are based on 10^5 primary particles of size 30 μm (large enough that perikinetic terms can be ignored) evolving under a shear rate of 0.1 s^{-1} with unity sticking probability ($\alpha = 1$). Simulations are run until the largest flocs get to be large enough to reduce the numerical accuracy of the simulation. The shear collision kernels scale approximately as $i_{l\text{-}1}^{2+3/D}$ so that as the range of floc sizes approaches a factor of 10^4 primary particles, the accuracy of the numerical solution will be reduced for double precision (roughly twelve digits of accuracy). Accuracy was checked by stopping simulations before the error in mass conservation reached 10^{-3}. The key result from Figure 21 is that lower fractal dimensions result in more rapid growth as expected since the cross sectional area scales with $i_{l\text{-}1}^{3/D}$. For a monodisperse distribution with fractal floc size, it can be shown that the growth diverges for finite time (c.f. Eq. (66)). The fractal shear kernel actually results in a distribution that is closer to a power-law size distribution. The number and volume distributions, n_i and Q_i, are shown in Figure 22 for three different times in the evolution of the case where D_f = 2.33. The volume moment is almost flat at longer times, and this is represented by the higher moments diverging. In addition to the first moment of the particles per floc, the fourth moment (particles to the fourth power per floc) is also shown in Figure 21 to indicate the gradual divergence of the higher moments when fragmentation does not occur.

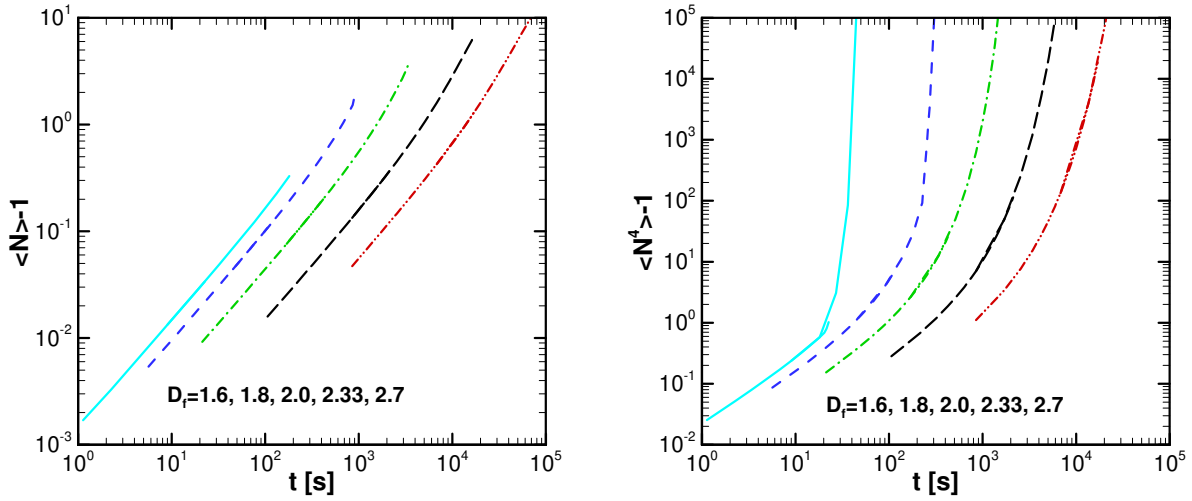

Figure 21. Growth of floc size predictions using sectional model with shear kernel for different fractal dimensions (Df = 1.6, 1.8, 2.0, 2.33, 2.7 from left to right). The left panel shows the evolution of the one less than the average particles per floc, while the right panel shows one less than the fourth moment of the particles per floc.

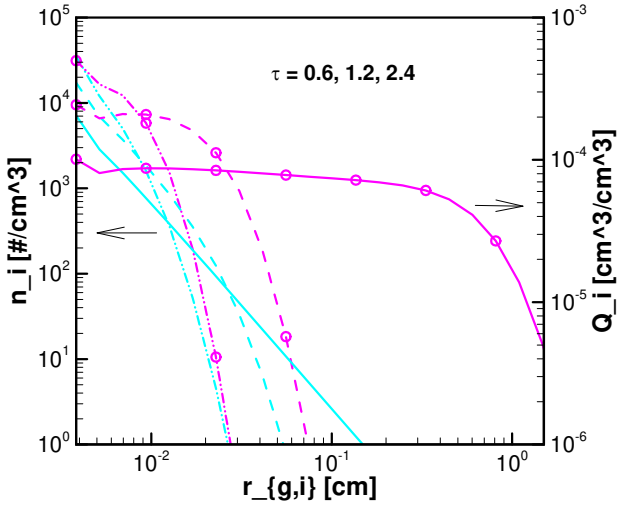

Figure 22. Number (no symbols) and volume (with symbols) distributions for the simulation in Figure 21 with D_f = 2.33 at three times expressed in terms of τ_{sh} of Eq. (34).

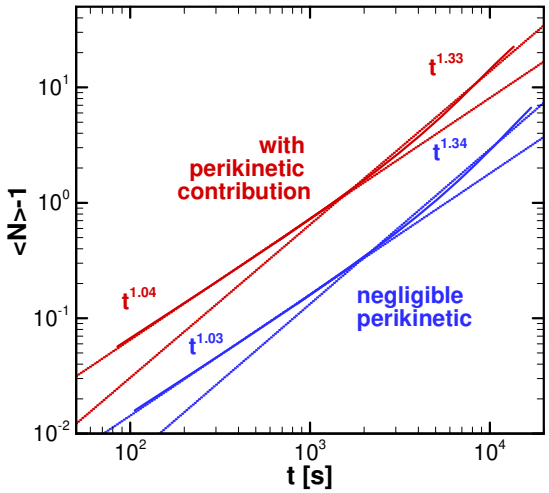

Figure 23. Growth of floc size prediction using sectional model with shear and Brownian kernels for fractal dimension of 2.33.

In Sec. 7 the growth of flocs under a combined Brownian and shear (peri-kinetic and ortho-kinetic) kernels will be discussed. Here we carry out a similar simulation but use the particle size close to size of the algae cells, 3 μm. At 3 μm, the Brownian kernel is less important than the shear kernel, but is not completely negligible as it is at 30 μm. Figure 23 shows a comparison of floc growth with 10^8 3 μm and 10^5 30 μm particles (giving the same volume fraction). The added influence of the perikinetic kernel accelerates the early growth, but the growth scales similarly in time. For comparison with Sec. 7 results, power laws early and late in the evolution are identified on Figure 23.

6 RESTRUCTURING OF CLUSTERS OF ADHESIVE PARTICLES DUE TO RANDOM FLUCTUATIONS

6.1 INTRODUCTION

Aggregates of fine particles are ubiquitous in nature and in industry. These aggregates grow through collision processes with rates determined by the combination of relative motion and effective cross-sectional area. In general, aggregates formed from well-defined primary particles (as opposed to coalescing liquid drops or bubbles) are observed to have fractal structures so that the effective radius of gyration is greater than that of a sphere of similar mass. Thus, a relationship between the mass, M, of an aggregate containing N primary particles of mass m_0 and radius r_0 and its radius of gyration R_g is:

$$\frac{M}{m_0}=N=k\left(\frac{R_g}{r_0}\right)^{D_f} \tag{48}$$

with k being a prefactor on the order of unity, and D_f being the standard mass fractal dimension. Such is the case for soot aggregates formed under explosive conditions and certain kinds of sooting flames [97-114] as well as other processes including flocculation in algal and waste water environments [115-118].

For rigid aggregates, various collision regimes have been identified and these have been found to result in fractal dimensions that are characteristic of the particular collisional mechanism. For example, in the continuum regime, in which aggregates diffuse before collision, also known as diffusion-limited cluster aggregation (DLCA), a fractal dimension of ≈1.8 [97, 104, 106, 110, 111, 113] (≈1.4−1.5 in 2D) [119] is observed for length scales just larger than the size of an individual particle up to nearly R_g. In the free molecular regime, where aggregates assume ballistic trajectories between collisions, the fractal dimension increases to ≈1.95 when thermal forces are the driving mechanism [120-122]. As aggregates grow in size and are affected more significantly by local shear conditions, two processes have been observed to cause deviations from these trends [123-132] . First, fragmentation of aggregates can be caused by fluid drag forces exceeding the bond strengths of particles making up the aggregate. Secondly, drag-imposed forces and torques can lead to restructuring of the aggregate. Both processes are strongly dependent on the exact multibody hydrodynamics that produce the drag forces, the nature and strength of the adhesive interactions between constituent particles, and the aggregate topology which controls the local strength of the aggregate, including the formation of multiple adhesive contacts and stress bearing structures.

A large body of work has focused on the determination of the fractal dimension that characterizes various collisional processes, the kinetic exponent that describes the rate at which the average cluster mass grows with time, and the evolving size distribution of clusters[119]. More often than not, researchers have focused on the relatively simple case of a single fractal dimensional scaling given a specified aggregation mechanism. As an example, many simulations of diffusive systems of aggregating particles have been able to reproduce the DLCA scaling of

mass to size ($D_f \approx 1.8$) seen in experiment. Alternatively, more elaborate flow conditions can complicate the aggregate structures, resulting in different fractal scaling laws at different length scales, even without restructuring [133-135]. One such case is the cluster dense regime. Due to the fractal nature of the growing structures, aggregation starting under dilute conditions can eventually lead to a situation where clusters are large enough to crowd each other and no longer collide along uncorrelated trajectories– a result of the reduction in the available free volume in the system ($R_{cluster} > N^{1/3}$). When this occurs, the fractal dimension can exhibit a shift from 1.8 to 2.6 [136], similar to the 3D percolation fractal dimension. Other cases where D_f shows a change with length scale have been observed in soot from laminar flames [134], where the aggregation mechanism becomes dependent on the height in the flame.

To date, much of the simulation work on aggregating systems has been performed in a Monte-Carlo framework where clusters are treated as idealized rigid entities. In such cases, the aggregates that are formed are normally simply connected; that is, every particle lies on a branch of a tree-like structure in which there are no closed loops. Topologically, these forms are relatively simple. The lack of closed loops allows for the exact specification of the constraint forces and torques, and one can make predictions about the locations at which clusters are likely to fragment or restructure under sufficient stress conditions [137, 138]. However, when closed loops are formed, the system becomes overspecified and the nature of the interaction potential becomes important. Stress can now be locked into the cluster structure. Under these conditions, particle dynamics simulations have an advantage over Monte-Carlo schemes since they allow for the determination of individual particle trajectories based on the solution of Newton's laws. Restructuring length and timescales result from these trajectories rather than being included in the model in an ad hoc manner.

In this work, we utilize a JKR-type adhesive potential [139-142] to describe the binary contacts that form between colliding adhesive particles. This potential resolves two-particle relative center of mass and angular motions and imposes constraints and damping terms on each mode. A method for thermostating this potential is presented. This approach to adhesive contacts provides a realistic description of the physical processes leading to the complex topologies encountered in aggregates of particles with semi-flexible contacts ranging from algae cells to colloids. The particle dynamics technique (i.e., Discrete Element Method – DEM) used in this work provides a realistic description of the physical processes governing aggregation and cluster restructuring in many practical situations, including aggregation of adhesive particles with flexible contacts in a liquid medium as well as restructuring and the formation of stress bearing structures within clusters.

In the second section of this paper we describe the implementation of the adhesive model as well as simulation details and parameters. Following this we discuss various measures of restructuring we have employed including the evolution of the cluster radius of gyration R_g, average coordination number and coordination number distributions, the pair correlation function $g(r)$, the static structure factor $S(q)$, and the formation of a stress-bearing backbone.

6.2 MODEL

We simulate clusters of adhesive particles using discrete particle dynamics with LAMMPS, an open-source molecular dynamics package [143] . We model the particle dynamics with a Langevin equation of motion to generate individual particle trajectories. Hence, our simulations are of a Brownian Dynamics type. For systems of adhesive particles, we solve two sets of Langevin equations, one for translation and one for rotational degrees of freedom

$$m_i \frac{d\mathbf{v}_i}{dt} = -\zeta \mathbf{v}_i + \sum_{j \neq i} \mathbf{F}_{ij} + \xi_i + \vartheta_{ij} \tag{49}$$

$$I_i \frac{d\omega_i}{dt} = \sum_{j \neq i} \tau_{ij} + \phi_{ij} \tag{50}$$

Here m_i and I_i are the mass and moment inertia of particle i, ζ the friction coefficient of the particles in the solvent, $\mathbf{v}_i$ the particle velocity, $\mathbf{F}_{ij}$ and τ_{ij} the interparticle forces and torques, and ξ_i, ϑ_{ij}, and ϕ_{ij} the stochastic forces and torques that couple thermal fluctuations to the dissipative components of the particle-fluid and particle-particle interactions. We will discuss the latter below when we describe thermostating internal modes, but note that these terms are applied pairwise as indicated by the subscript ij; this is essential. For now we note that the random force due to thermal fluctuations in the fluid is given by standard Brownian dynamics, $\langle \xi_i \rangle = 0$ and $\langle \xi_i(t) \xi_i(t') \rangle = 2k_B T \zeta \delta(t - t')$, where k_B is Boltzmann's constant and T is the temperature.

As can be gathered from the above discussion, for simplicity, we choose to model the hydrodynamic interactions using the "free-draining" assumption for particle drag. Thus, each particle feels a constant Stokes drag force, $-\zeta \mathbf{v}_i$, where $\zeta = -3\pi\eta d$, and a corresponding delta-function correlated random force consistent with fluctuation-dissipation balance which is standard for the Langevin-type thermostat of Brownian dynamics. Note that for this implementation, we do not allow particle-solvent interactions to impose torques on the individual particles. Again, we have not included multibody hydrodynamic effects in this work. The following section discusses the details of the particle-particle interactions. Since these interactions contain non-conservative (velocity-dependent) terms we shall also discuss thermostating inter-aggregate modes due to the pair-wise particle interactions.

6.2.1 ADHESIVE POTENTIAL

To handle particle interactions, we have implemented a JKR-based granular adhesive potential similar in form to that used by Marshall [141, 142] with components derived previously by Chokshi et al. [102], Dominik and Tielens [139, 140], Cleary [144] and Mindlin [145]. In this scheme, relative motion between spherical adhesive particle pairs is decomposed into normal [102], rolling [145, 146] shearing [139, 140], and twisting terms [142], with each mode of motion independently constrained. When no adhesion is present the relative motion between spherical particles of identical material in contact is standard [146].

$$\delta_{ij} = \frac{1}{2}(d_i+d_j)-r_{ij} \tag{51}$$

$$\mathbf{v}_{n_{ij}} = (\mathbf{v}_{ij}\cdot\mathbf{n}_{ij})\cdot\mathbf{n}_{ij} \tag{52}$$

$$\mathbf{v}_{t_{ij}} = \mathbf{v}_{t_{ij}} - \mathbf{v}_{n_{ij}} - \frac{1}{2}(\omega_i+\omega_j)\times\mathbf{r}_{ij}. \tag{53}$$

where $\mathbf{r}_{ij}=\mathbf{r}_i-\mathbf{r}_j$ is the relative position vector, $\mathbf{n}_{ij}=\mathbf{r}_{ij}/r_{ij}$ is the unit normal direction of the contact, $r_{ij}=|\mathbf{r}_{ij}|$ is the distance between particle centers, δ_{ij} is the distance between the particle surfaces along the normal, $\mathbf{v}_{ij}=\mathbf{v}_i-\mathbf{v}_j$ is the relative velocity of the two contacting particles, $\mathbf{v}_{t_{ij}}$ is the relative tangential surface velocity of the spheres, and ω_i is the rotational velocity of particle i.

With adhesion present additional constraints on the relative rolling and twisting motions are present. The relative motion in these modes is determined by

$$\Theta_{tw_{ij}} = (\omega_i-\omega_j)\cdot\mathbf{n}_{ij} \tag{54}$$

$$\mathbf{v}_{r_{ij}} = -R(\omega_i-\omega_j)\times\mathbf{n}_{ij} - \frac{1}{2}\left(\frac{d_j-d_i}{d_j+d_i}\right). \tag{55}$$

In the normal mode the magnitude of the force due to Hertzian contact of the linear elastic particles and the cohesive force due to adhesive surface energy, γ, is calculated according to

$$F_{n_{ij}}=4F_c\left[\left(a/a_0\right)^3-\left(a/a_0\right)^{3/2}\right], \tag{56}$$

with the cohesive force $F_c=3\pi\gamma R$. Here the contact radius between the spherical particles a, with equilibrium value $a_0=\left(\frac{9\pi\gamma R^2}{E}\right)^{1/3}$, is determined via the particle radii and the degree of overlap by inverting

$$\delta_{ij} = \frac{a^2}{R}-\sqrt{\frac{8\pi\gamma Da}{3}}, \tag{57}$$

with $R=2(\frac{1}{d_j}+\frac{1}{d_i})$, $D=\frac{3}{2}(1-\nu^2)/Y$, where Y is Young's modulus and Poisson's ratio ν[102, 147, 148]. The normal force is discontinuous in that up to the point of contact of approaching particles, no force is felt, whereas at first contact there is a finite force present. Similarly, an adhesive particle pair that is separated has a non-zero tensile force at a separation distance greater than the sum of the particle radii [102].

For contacting particles, a dissipative normal force is imposed on the normal mode of the form

$$F_{n_{ij}diss}=-\beta_{ij}|v_{n_{ij}}| \tag{58}$$

where $\beta_{ij}=\gamma_n R_H m_{eff}$, γ_n is the normal damping coefficient, $R_H=\left(R\left(r_{equil}-r_{ij}\right)\right)^{1/2}$ is the displacement from equilibrium using a Hertzian form following the viscoelastic model of Brilliantov et al. [147], is the equilibrium separation, and $m_{eff}=(1/m_i+1/m_j)^{-1}$ is the effective mass of the two particles.

The tangential (shear) force due to friction is calculated by

$$F_{t_{ij}}=-k_s\Delta|\mathbf{s}_{t_{ij}}| \tag{59}$$

where $k_s=8Ga$, G the shear modulus, $\Delta|\mathbf{s}_{t_{ij}}|$ is the accumulated elastic tangential (shear) surface displacement of the particles obtained by integrating the surface relative velocities over the lifetime of the contact. This force is truncated when appropriate to satisfy the Coulomb friction criteria under the influence of a constant adhesive force $F_{t_{ij}}\leq\mu F_{n_{ij}}+F_c$.

A torque, $\tau_{t_i}=\frac{1}{2}d_i F_{t_{ij}}$, is also associated with the tangential (shearing) mode in order to conserve angular momentum.

Similarly, a rolling torque is calculated from

$$\tau_{r_i}=-k_r\Delta|\mathbf{s}_{r_{ij}}| \tag{60}$$

where $k_r=4F_c\left(a/a_0\right)^{3/2}$ and $\Delta|\mathbf{s}_{r_{ij}}|$ is the magnitude of the accumulated surface displacement of the two particles along a rolling mode (tangential surface velocities along same direction) obtained by integrating $\mathbf{v}_{r_{ij}}$ over the lifetime of the contact.

Finally, for the twisting mode, a torque is assigned as

$$\tau_{tw_i}=-k_{tw}\Theta_{tw_{ij}} \tag{61}$$

where $k_{tw}=4Ga^3$ and $\Theta_{tw_{ij}}$ is the accumumulated angular displacement in the twisting mode. Note that no forces are associated with the rolling and twisting modes.

For the current set of simulations, we impose a critical condition on the normal mode only. A critical condition indicates one for which the amount of displacement in the given mode is sufficient to break the adhesive contact between particles. Critical conditions are not imposed on rolling, shearing, and twisting modes since restructuring can become highly sensitive to the critical values in each mode. These are difficult to parameterize to any degree of experimental accuracy. We have implemented the necessary machinery to handle critical conditions for each mode into our model, though we are reserving a complete investigation of that topic for a future study.

6.2.2 THERMOSTATING INTERNAL MODES

A new aspect of this work is the inclusion of thermostating for the adhesive contacts between pairs of particles. We have investigated restructuring for each set of simulation parameters both with and without thermostating of internal modes. In order to maintain a fluctuation-dissipation balance (F/D), each of the adhesive binary modes (normal, twist, roll, and shear) should receive stochastic forces and torques consistent with the dissipation experienced in that mode. A balance between thermal fluctuation and dissipation must be maintained on the particle-fluid interactions through the inclusion of a fluid drag force on particles in a solvent that corresponds to the stochastic thermal forces they receive from the fluid. This results in Brownian motion and diffusion for individual particles. However, when two or more particles are in contact, if we damp out the binary modes of relative motion, then if we measure the temperature for the system of particles based on the relative motion of the contacting particles, we will measure the "wrong" temperature relative to that specified due to the fluid fluctuations and measure based on translation degrees of freedom of the particles. Since the interparticle forces/torques are Newton-pairs, this will not directly affect the external motion of the cluster of particles, since they are adhesively bound. However, it can indirectly affect it since adding energy back into these modes to maintain F/D can result in additional restructuring of the cluster, which can in turn affect particle mobility in the solvent.

For simulations in which we incorporate a thermostat on the interparticle potentials, $\frac{1}{2}kT$ of thermal energy is contained in each mode of relative motion (normal, twist, roll, shear) at thermal equilibrium by equipartition of energy. Furthermore, fluctuation-dissipation balance is maintained by setting the stochastic (thermostat) force/torque (cf. terms ϑ_{ij} and ϕ_{ij} in Equations 2 and 3 above) in each mode in the standard, albeit pairwise, manner. The pairwise application of the stochastic force is key – Newton's third law must be respected for the thermostating to be effective. For example, in the normal mode the stochastic force is assumed to be a Gaussian random variable chosen according to $\langle \vartheta_{ij} \rangle = \mathbf{0}$, $\langle \vartheta_{ij}(t) \cdot \vartheta_{ij}(t') \rangle = 2k_B T \beta_{ij} \delta(t-t')$, where β_{ij} is the damping coefficient in the normal mode. Similar considerations exist for the other pairwise modes which also include dissipative/damping forces. A primary objective of this work is to understand the influence of including thermal energy fluctuations in the binary modes in terms of aggregate evolution.

6.2.3 INITIAL CLUSTER

We begin each simulation with a single prebuilt fractal cluster generated from an algorithm that creates structures of a specified mass, N, fractal dimension, D_f, and prefactor, k. For comparison to DLCA type flocs, we use D_f=1.8 and k=1.3 [149]. Clusters are built in a hierarchical fashion, starting with dimers. At each step an N-mer is built out of two identical $\frac{N}{2}$-mers that are placed in random contact locations with each other. For each placement a test of M vs R_g is performed. If R_g falls within a tolerance (in our case 10%) of the value given by the fractal scaling law, the placement is accepted. The user is allowed to specify for what size the fractal scaling law will be checked. We use 16, consistent with previous work [150] that shows that the fractal scaling law

for DLCA aggregates begins to hold near a cluster size of N=16. The builder thus generates clusters of size $N=2^M$, with M an integer. We choose to investigate clusters of mass N=128, which are large enough to exhibit fractal scaling over a significant size range while being small enough to allow for evolution of the structure within the available computational time. We are careful to set the interparticle spacing consistent with equilibrium separations determined from two particle runs using the same potential parameters used for restructuring simulations. This avoids any initial unstable response from particles being placed in high energy configurations at the beginning of the simulation. We use a single initial cluster configuration for all simulations. For each set of simulation parameters we perform a series of 10 independent simulations to allow for evolution of the structure over a statistically reasonable number of samples. For each simulation, we place the structure in a background solvent of a known viscosity and observe the evolution of the cluster structure as a function of time. The as built fractal cluster is not in equilibrium, that is its configuration is not a global energy minimum state which would be a collapsed compact structure with a large average coordination number per particle. The interparticle adhesive potential, described below, contains angular constraints that inhibit such collapse to a degree. Thermostating, both of the fluid-particle and interparticle interactions allows for a degree of restructuring.

6.2.4 PARAMETERS

For the sake of simplicity, we use dimensionless units for all potential parameters, where all particles are spherical with diameter, d=1 and mass m=1. Adhesive parameters are set to E=100, G=100, γ=1.0, γ_n=10.0. To increase rigidity we have increased the strength of the twisting, shearing, and rolling modes each by a factor of 10, which is mathematically identical to increasing the shear moduli G by the same factor. The maximum stable time step is $\approx 3\times10^{-4}\tau$. As stated, this parameter set enables significant evolution of the cluster structure in the available computational time. Each simulation proceeds for 9×10^8 time steps, which corresponds to a total simulation time of $t_{sim}=2.7\times10^5$. We set the fluid viscosity to $\eta=5.56\times10^{-4}$ or 5.56×10^{-3} in all cases, consistent with other aggregation simulations that we have performed at initially low volume fractions with this set of parameters to be reported separately. The system temperature is varied from $T=10^{-5}$ to 10^{-1}. We have chosen damping times (τ_{damp}) associated with dissipation of energy in each angular binary mode (rolling, twisting, shearing) that allow no more than four to five oscillations for any mode before falling below the thermal noise floor. While it may be desirable to overdamp each of these modes, doing so requires the use of smaller time steps than those used here in order to ensure system stability. We have chosen adhesive parameters that result in particles that stick on contact with unit probability under the influence of Brownian motion (using the chosen viscosity/temperature) and have a linear persistence length on the order of ten monomers at temperatures near $T=10^{-3}$. As for any binding potential, each of the four motional terms is approximately harmonic near equilibrium. To maintain rigidity, a large "spring" constant is required, which necessitates correspondingly small time steps. It is nontrivial to choose parameters that allow for both relatively rigid contacts (large spring constants) and sufficient time evolution of the system within a reasonable computational time.

6.3 RESULTS

We evaluate the results of cluster restructuring via several metrics. These include morphological changes observed in the restructured clusters as seen in late time configurations, time evolution of the cluster radius of gyration, R_g, and the particle coordination numbers (number of adhesive contacts per particle) $\langle N \rangle$, the formation of a stress supporting backbone, and the scaling of the mass with the size as determined from the logarithmic slope of the static structure factor, $S(q)$ [150], and the pair correlation function, $g(r)$.

6.3.1 MORPHOLOGIES

Restructuring is often evidenced by a decrease in a cluster's linear extent given a constant particle number. More precisely, restructuring in systems of adhesive particles is an energy minimization process where a reduction in the "size" of a cluster allows additional contacts and thus greater stability. Restructuring in this sense occurs when particles within a cluster are brought into contact by local rearrangement due to deterministic or stochastic forces leading to an energetically more stable structure than had previously formed. Figure 24 displays images of clusters observed during our simulations. . Figure 24 (a) shows the as-constructed cluster, a structure typical of the D_f=1.8 extended, branched fractals observed in diffusion limited cluster-cluster aggregation. . Figure 24 (b) through (f) show late time restructured clusters at temperatures from T^{-5} to T^{-2} and at a temperature of T=10^{-3} at two different viscosities η=5.56×10^{-3} and 5.56×10^{-4}, without and with inclusion of a thermostat on the binary adhesive modes. Clearly, larger temperatures result in greater degrees of restructuring as does the inclusion of an internal thermostat at all temperatures. We notice several key features including the reduction of the overall linear size of the cluster, the formation of closed, stress-bearing loops at moderate temperatures, and the large degree of compaction with a highly increased coordination number at the highest temperatures.

Restructuring is often thought of in terms of a morphological change such as an increase in D_f at all length scales, consistent with compaction resulting in a decrease in the size of the cluster. However, restructuring can and does produce topological changes that drastically increase the ability of a floc to withstand or handle fluid stress without that leading to large increases in the fractal dimension or significant changes in the size. Formation of closed loops is one example of this which we observe to be favored increasingly with rising temperature for simulations not invoking internal thermostating. Coarsening of a cluster can also occur, where branches collapse to form thicker stress-bearing backbones, affecting the fractal dimension only at small length scales. Compaction and possible coarsening occurs for simulations involving an internal thermostat, where closed stress-bearing loops are observed at the lowest temperature of T=10^{-5}, but compaction and or coarsening appears to dominate at higher temperatures. The static structure factor can be used to distinguish whether the compaction is scale-invariant leading to a global increase in the fractal dimension or occurs only on small length scales. This is discussed in detail a later section.

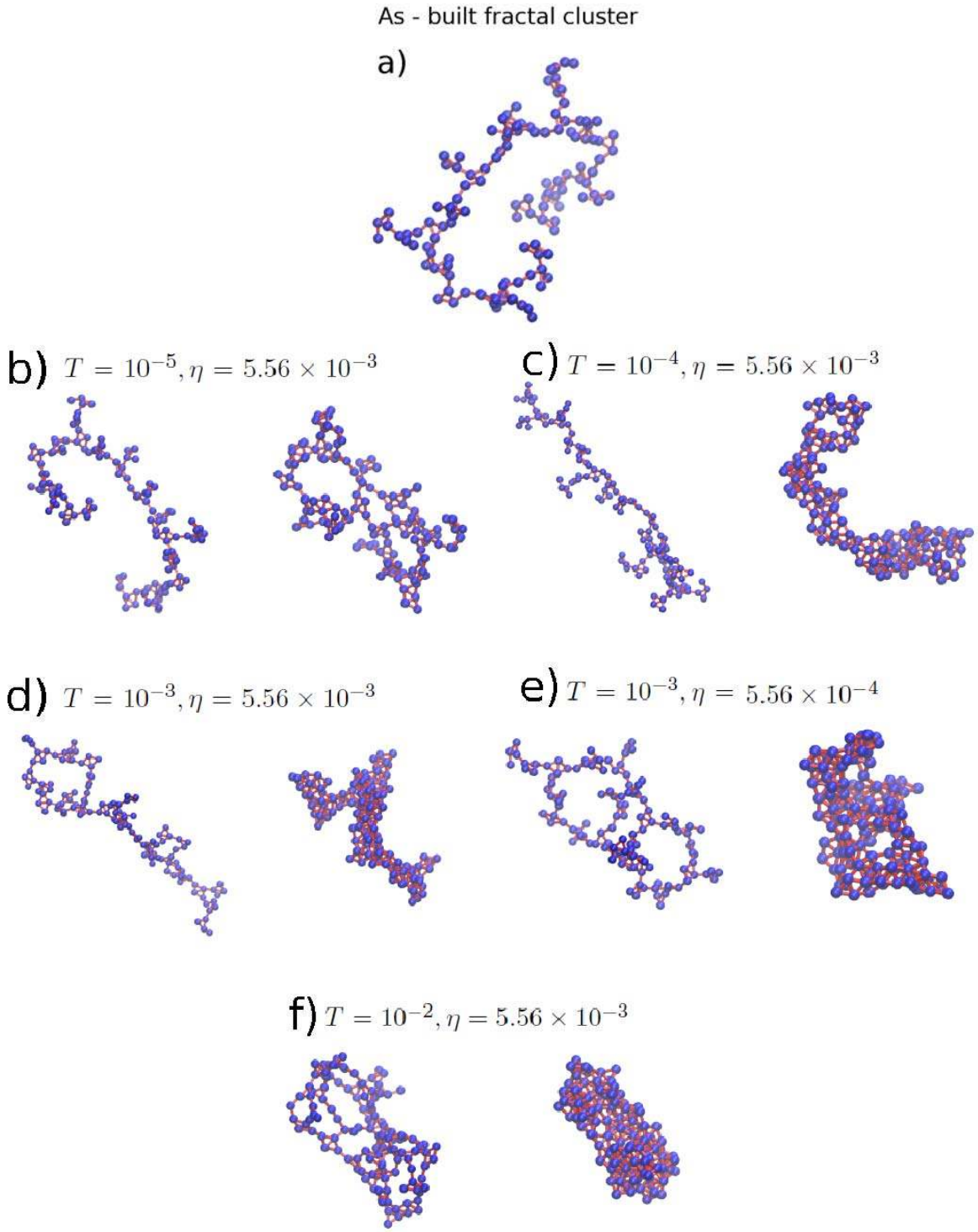

Figure 24. (a) Initial cluster configuration. (b)-(f) Late time cluster configurations (t=2.7×10^5) for each set of simulation parameters without (left) and with (right) internal thermostating.

Cluster restructuring often counterintuitively increases the effective density with increasing temperature up to the point of cluster instability, at which the particle contacts are broken and the cluster disintigrates or dissolves into the surrounding medium. Note that while fractal structural forms are generally "stable", they do not represent equilibrium structures sitting at well-defined energy minima, but are rather meta-stable and kinetically frustrated, their forms a result of the stochastic process of formation, existing in local energy minimum, not global energy minimum configurations. Further collapse to an energy minimum structure becomes inhibited by energetic barriers maintained either by multiple particle contacts or stress-bearing structures like closed loops. Heating a cluster up can increase internal cluster motions significantly, resulting in additional adhesive bond formation and structural adjustment.

6.3.2 RADIUS OF GYRATION

The "size" of a cluster of mass N is often calculated as the cluster radius of gyration, R_g. Figure 25 displays the time evolution of R_g for the clusters shown in Figure 24. The reduction observed in R_g is consistent with the restructuring we see in Figure 24, where clusters collapse to a greater or lesser degree. We observe that for each T and η, the internal thermostat leads to increased restructuring, significantly lowering R_g from its nonthermostated counterpart. The internal thermostat also results in more rapid rearrangement into the resulting structure. As we stated earlier, we expect particle rearrangement to be greater in clusters that include internal thermostating since each of the binary contact modes should contain $\frac{1}{2}kT$ of thermal energy and not simply act as a damping mechanism. The reduction in R_g is a strong function of temperature with and without the internal thermostat included. As expected, larger temperatures lead to larger degrees of restructuring and smaller late time R_g values. We do not display data for temperatures above 10^{-2} since for T not much above that point, a critical point is reached and particle contacts are broken as the cluster disintegrates. At T=10^{-3}, a change in viscosity does not have a large effect on the steady-state value of R_g, but it has a larger effect on the standard deviation, indicating that a larger viscosity results in structures with larger variation in R_g. Apparently, larger thermal forces which occur at higher viscosities even at the same temperature result in clusters with greater morphological variety. These larger forces may more easily push particles into irreversible adhesive trajectories, indicating that the larger the random force, the less deterministic the outcome. A change in R_g for a fractal structure can result from either an increase in the fractal dimension, D_f, or the fractal prefactor k. The scaling of the static structure factor $S(q)$ as a function of the wave vector q or the pair correlation function $g(r)$ with r (discussed later) can be used to distinguish between these possibilities, since the scaling exponent is independent of k.

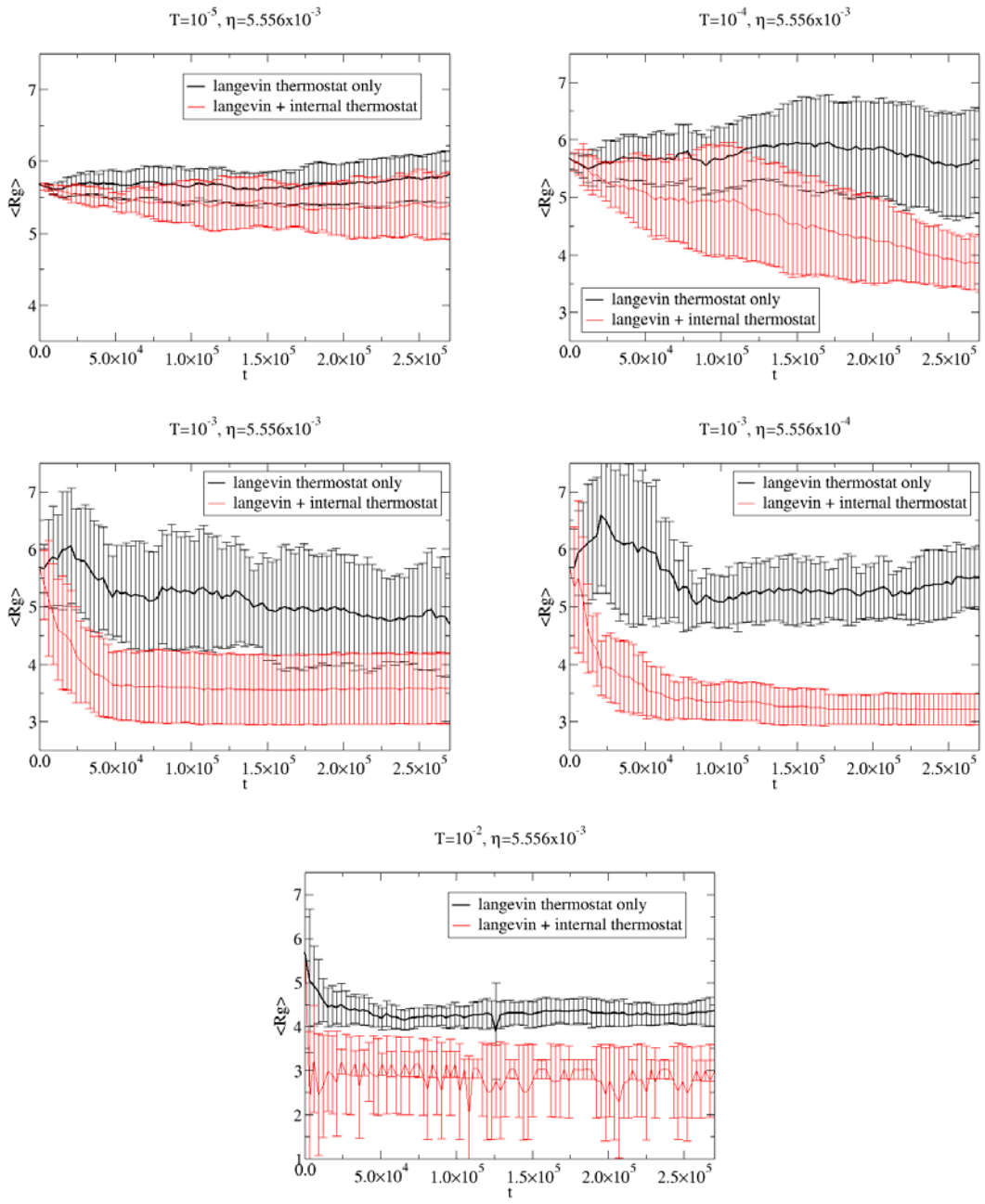

Figure 25. a) Time evolution of R_g for each set of simulation parameters without and with internal thermostating. Row 1 left: T=10^{-5},η=5.56×10^{-3}, Row 1 right: T=10^{-4},η=5.56×10^{-3}, Row 2 left: T=10^{-3},η=5.56×10^{-3}, Row 2 right: T=10^{-3},η=5.56×10^{-4}, Row 3: T=10^{-2},η=5.56×10^{-3}

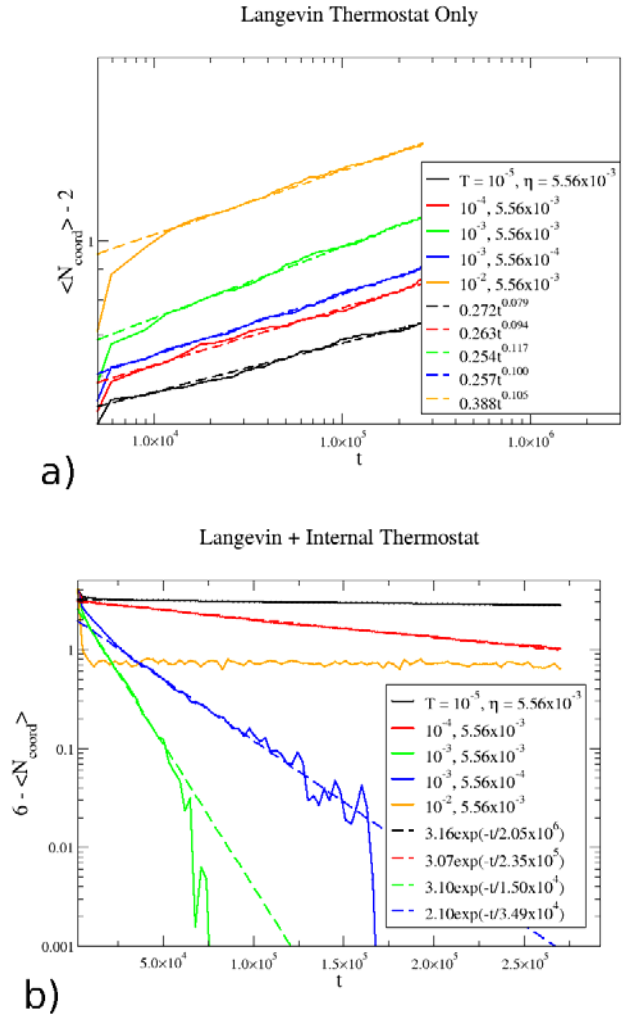

Figure 26. a) Time evolution of the average coordination number for each set of simulation parameters without internal thermostating showing power law growth with time: T=10^{-5},η=5.56×10^{-3}; T=10^{-4},η=5.56×10^{-3}; T=10^{-3},η=5.56×10^{-3}; T=10^{-3},η=5.56×10^{-4}; T=10^{-2},η=5.56×10^{-3}. b) Time evolution of the average coordination number for each set of simulation parameters with internal thermostating showing exponential trend. Colors are same as for a).

6.3.3 COORDINATION NUMBER

Figure 26 displays the time evolution of the average coordination number for the clusters shown in Figure 24. The original cluster structure has an average coodination number of 2, indicating a branched morphology, each branch a single particle thick. Lines and loops of particles also have coordination numbers of ≈2. As time proceeds, $\langle N_{coord} \rangle$ increases in a temperature dependent way. At the highest temperature of 10^{-2}, without internal thermostating, the coordination number grows quickly to ≈3 and slowly increases to ≈3.5 at the latest times. Referring to Figure 24, we see that this coincides with the formation of several small closed loops within the cluster. The growth is consistent with a power law form in time $\langle N_{coord} \rangle \propto t^{\alpha}$ with α≈0.1. In fact, for all temperatures and viscosities used in this study, restructuring without an internal thermostat is

well described by a power law dynamic with a power α not far from 0.1, with only a weak increase in α with T. That is, there is a slow evolution of the coordination number even at the latest times. When internal thermostating is included at $T=10^{-2}$, the restructuring is far more severe, leading to a steady state value of ≈5.2 for $R_g \approx 3$ (Figure 25) and a very compact morphology (Figure 24). Interestingly, with internal thermostating on, a slightly higher late time coordination number is obtained for all lower temperatures, which appear to exponentially approach 6. The relaxation time constant is a decreasing function of the temperature and viscosity. The rate of convergence is due to the intensity of the forces experienced by the particles, which is viscosity dependent. The fact that the final value is nearly independent of the viscosity is due to restructuring being dominated by interparticle contacts at late times rather than by particle-fluid interactions. A coordination number near 6 has been observed for hard sphere glasses by Rintoul and Torquato [151]. This is an interesting interpretation of the restructuring that can be expected of systems of adhesive particles where, in limiting cases, the cluster collapses into a frustrated glass-like state. The coordination number of ≈5.2 at $T=10^{-2}$ is lower than this due to the presence of sufficient thermal energy in the system to statistically break some of the interparticle contacts. Entropy gains, which favors fewer particle contacts (constraints) ($T\Delta S$) start to dominate over internal energy minimization which favors more contacts. At a temperature not much greater than 10^{-2}, the entire cluster disintegrates.

Figure 27 shows the evolution of individual coordination numbers for a few of these cases. For a temperature of 10^{-3} at $\eta=5.56\times10^{-3}$, the individual coordination numbers show nearly converged values with and without internal thermostating by the latest times. Without internal thermostating, approximately twice as many particles have a coordination number of 3 than either 2 or 4. With internal thermostating, the coordination numbers seem very well converged, with larger fluctuations consistent with the thermostat, though here there is nearly equivalent populations of coordination numbers of 5, 6, and 7, with a significant fraction of the particles with either lower or higher coordination numbers. That is, the distribution has a much larger spread in the case of the inclusion of an internal thermostat.

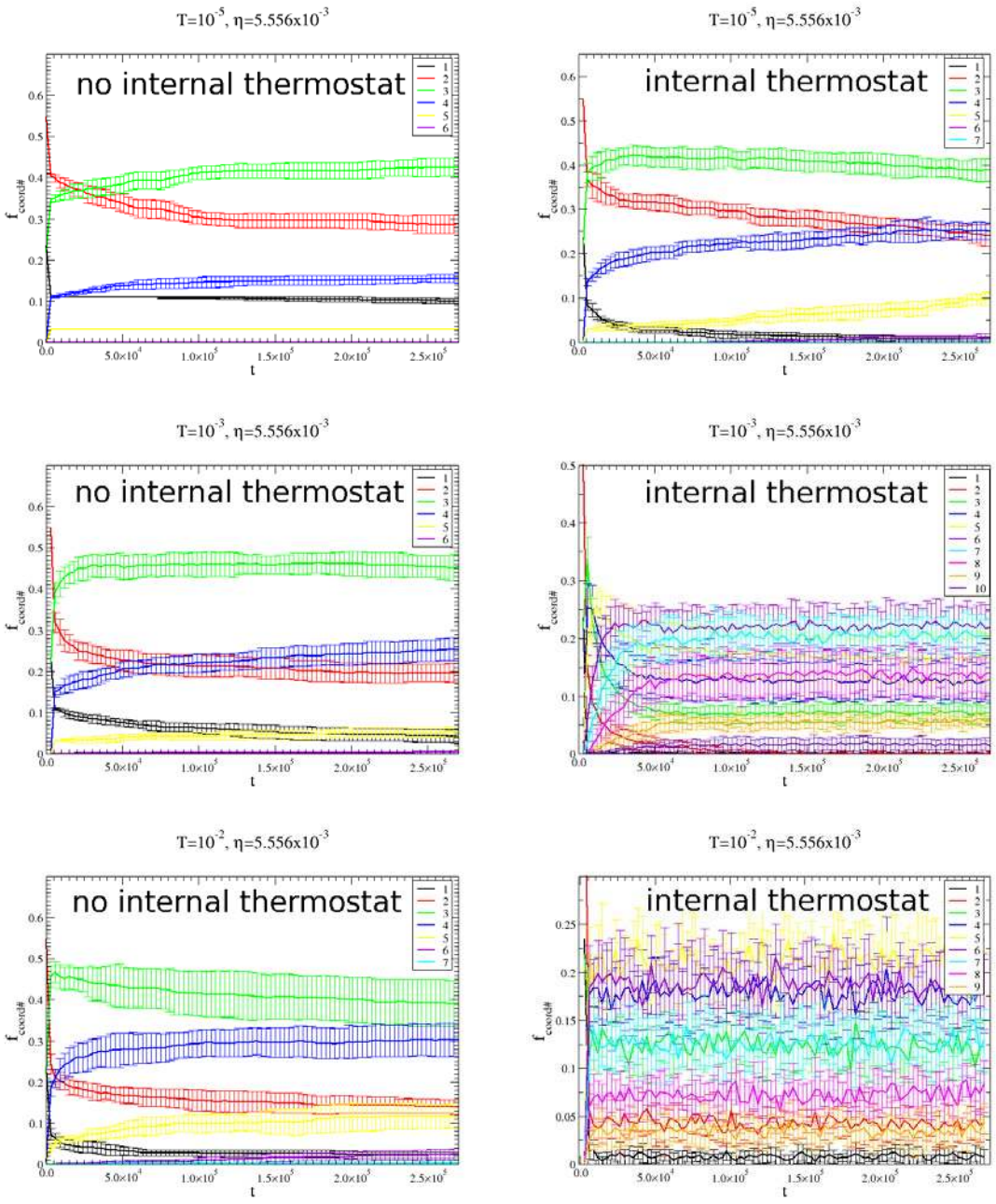

Figure 27. Time evolution of individual coordination numbers from 1 to 10 for 3 sets of simulation parameters without and with internal thermostating. Row 1 : T=10^{-5},η=5.56×10^{-3}; Row 2 : T=10^{-3},η=5.56×10^{-3}; Row 3 : T=10^{-2},η=5.56×10^{-4}. Error bars are standard deviation of values based on 10 independent runs at each set of parameters.

6.3.4 STRUCTURE FACTOR

In Figure 28 we display the static structure factor for clusters using each set of simulation parameters. The structure factor we define as $S(\vec{q})=N^{-2}\left|\sum_{i=1}^{N}\exp(i\vec{q}\cdot\vec{r}_i)\right|^2$ over the wave vector $\vec{q}$. A scalar form of $S(\vec{q})$, $S(q)$ is generated by averaging $S(\vec{q})$ over all possible $\vec{q}$ with the same magnitude but different orientations. The structure factor is the reciprocal space analog to the pair-correlation function $g(r)$. The real space variable r and its reciprocal-space counterpart q are related through $q = 2\pi r/r$, indicating that given a specific value (frequency) of q, the presence of a particle at a distance $r = 2\pi/q$ from another particle will represent a particle "in-phase" with the other at the given frequency. For fractal clusters, $S(q)$ is known to scale as q^{-D_f} for length scales between the monomer size and the cluster radius of gyration. For $q<<1/R_g$, $S(q)\approx1$, since for very low frequencies, the entire cluster of particles is in phase. We utilize the structure factor to determine if restructuring has produced any changes in the fractal scaling of clusters as a function of q or alternatively r. Fry et al. [136] have shown that a noticeable change in fractal scaling occurs in the structure factor for systems of particles that aggregate initially as diffusion limited up to a point that the clusters crowd one another and the free volume approaches zero. In this case, for low q (large length scales), the scaling of $S(q)$ changes from $q^{-1.8}$ to $q^{-2.6}$, indicating percolation in 3D, while at larger q values (smaller length scales), the $q^{-1.8}$ trend remains. The resulting clusters are multi-fractal, having different scaling laws active at different length scales. $S(q)$ is a powerful tool in shedding light on the fractal scaling in action at each length scale. For Figure 28, we plot $S(q)$ and it's logarithmic slope vs. $r = 2\pi/q$, since it is simpler to determine length scales via r. D_f is the logarithmic slope of $S(q)$ vs r. At the lowest temperature of $T=10^{-5}$, D_f is fairly consistent over the pertinent range of length scales, averaging about 1.7±0.1, regardless of internal thermostating, consistent with D_f for the original cluster. As we expect at this low temperature, the structure has not been significantly affected by thermal motions, whether or not thermostating of the internal modes has been included. As discussed in the morphology section, internal thermostating at this temperature results in the formation of closed loops, but clearly does not have a large impact on the resulting structure factor. At the next highest temperature, $T=10^{-4}$, some restructuring has occured, as evidenced by the increase in slope at large length scales to $D_f>2.0$ for both thermostated and non-thermostated samples. For the thermostated case, restructuring is increased at smaller length scales consistent with coarsening, D_f varying between 2.3 and 2.8 for r between 2 and 6. For the unthermostated case, $D_f<2.0$ and averaging near 1.5 for the same range, indicating that restructuring at larger length scales is favored. In all cases, we see that restructuring is greater when internal thermostating is included. At small length scales, when only dissipation is included (without stochastic thermal kicks) for binary adhesive modes, stochastic forces from the fluid are insufficient to restructure clusters at small length scales. When thermostating is included on these modes, however, restructuring can be initiated at all length scales. This trend continues to higher temperatures, in each case showing increased restructuring at large length scales for both inclusion and exclusion of internal mode thermostating, with inclusion resulting in restructuring at all length scales and exclusion lacking this feature. For $T>10^{-5}$, we also observe the reduction in cluster R_g as noted earlier; this is manifest in a shift in the position of the large r plateau between simulations with

and without internal thermostating with the plateau denoting the length scales over which the entire aggregate is in phase.

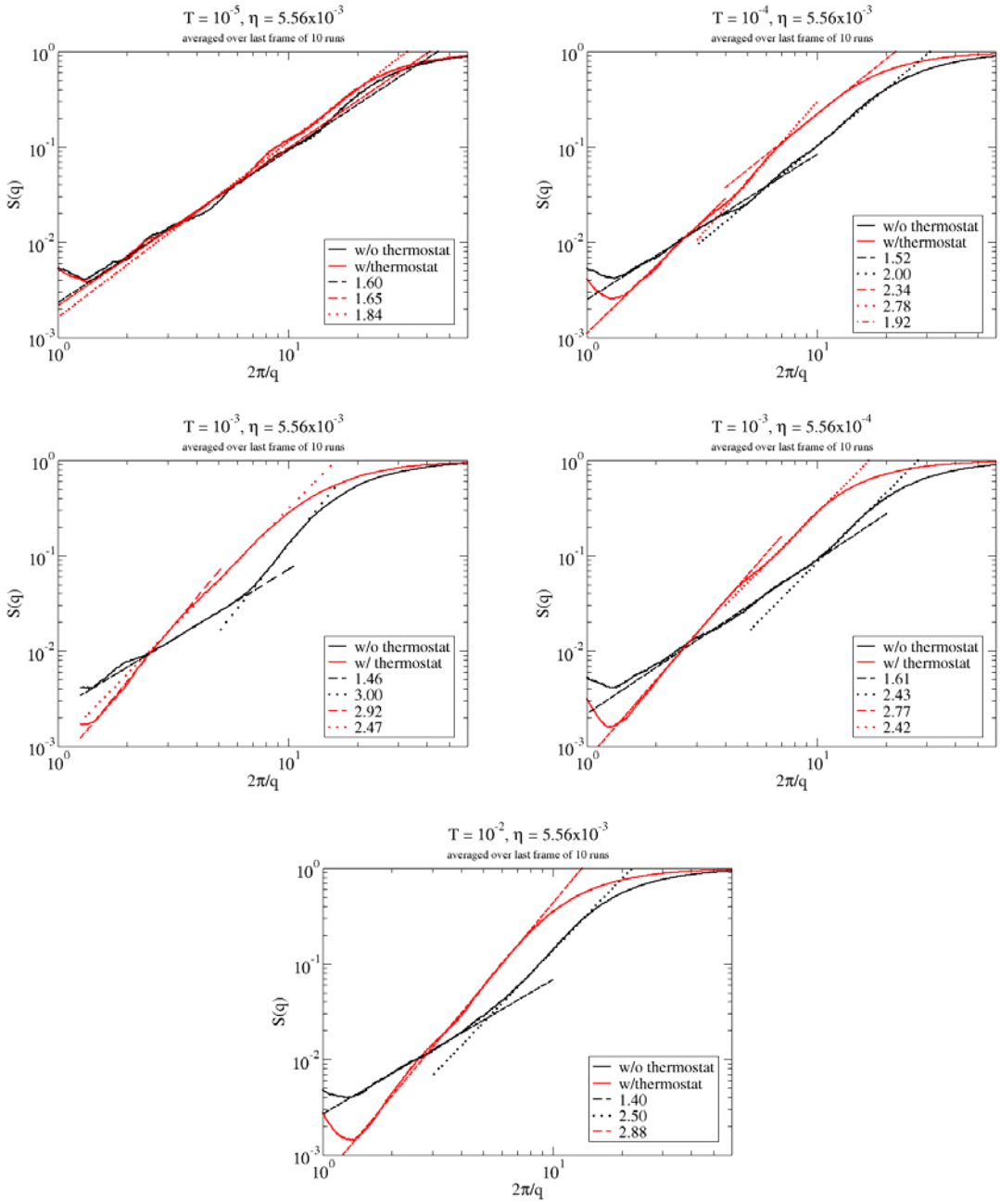

Figure 28. Average structure factor *S*(*q*) over 10 independent realizations of late time (*t*=2.7×10^5) simulations at each set of simulation parameters vs. *r* = 2π/*q*. Logarithmic slope indicating the value of D_f for various regions is also shown.

6.4 CONCLUSION

In this work the process of restructuring of fractal aggregates of adhesive particles has been investigated through a JKR-type adhesive model consistent with the original work of Dominik and Tielens [139, 140] . Restructuring is seen to be a dynamic process that is sensitive not only to the strength of the interparticle adhesive parameters, fluid viscosity, and temperature, but also to the exact way in which thermostating is treated. The authors argue that for adhesive potentials in which there is a dissipative term governing drag for a particular mode of motion (normal, shear, rolling, or twisting), a corresponding fluctuation term should be present. This coupling of fluctuation-dissipation is the basis for the Langevin thermostat that results in standard Brownian motion. Fluctuation-dissipation imposed on the adhesive particle modes ensures that "temperature" resolved at the particle scale is consistent with the thermostating temperature. When thermostating of adhesive modes is ignored, fractal aggregates of adhesive particles are seen to maintain the original fractal scaling of mass to radius at small length scales, but show enhanced fractal dimensions due to restructuring at large length scales only. When adhesive thermostating is included, fractal aggregates restructure to higher fractal dimensions at all length scales. These effects are observed in the evolving morphologies of the aggregates as well as the evolution of the static structure factor. The process of restructuring is very slow in the case of simple Brownian (no adhesive) thermostating and results in lower average coordination numbers than in the case of the inclusion of adhesive thermostating. At the latest simulation times, aggregates experiencing only Brownian thermostating exhibit structures that are still evolving as seen by the average coordination number while adhesively thermostated clusters appear to have reached steady-state forms.

7 PERI-/ORTHO-KINETIC AGGREGATION OF ADHESIVE PARTICLES

7.1 INTRODUCTION

Aggregation, agglomeration, coagulation, and flocculation are all terms used to describe the formation of clusters of small particles dispersed in a background fluid. Such processes have received a great deal of attention in the last several decades due their importance in a large number of industrial applications. The timescales for aggregate growth are a result of several key factors including the fluid flow conditions, the relative densities of the particles and the fluid, the particle concentration, and the evolving aggregate morphologies which are both affected by and affect the background flow. Evolving aggregate structures determine not only the drag forces felt by the aggregates but also the collision cross sections that leads to aggregate growth. At low shear rates, Brownian motion is dominant for aggregates of submicron length scales. Drag forces increase with size so that for sufficiently large particles or aggregates, shear forces become the dominant factor providing relative motion. This shift from perikinetic (Brownian or diffusive) to orthokinetic (shear-driven) aggregation is associated with a change in the scaling of the growth rate from roughly linear to something larger at a shear-rate dependent time. Previous works have found an exponential growth for coalescing drops under shear in agreement with Friedlander's (Friedlander64) and other's theoretical predictions based on the assumption of monomodal distributions. In addition to the aggregate motion, growth rates depend on the relative cross-sectional area presented by aggregates. Aggregates formed from noncoalescing particles are observed to have fractal structures so that the effective linear size is greater than that expected for a sphere of the same mass. The standard relation between the mass, M, of an aggregate containing i primary particles of mass m_0 and radius r_0 and its radius of gyration R_g is:

$$M=im_0=k\left(\frac{R_g}{r_0}\right)^{D_f} \tag{62}$$

with k being a prefactor on the order of one, and D_f being the fractal dimension. For rigid (nonrestructuring) aggregates, various collision regimes have been identified with characteristic fractal dimensions. In the continuum regime, for diffusion limited cluster-cluster aggregation, a fractal dimension of ≈1.8 (≈1.4−1.5 in 2D) is observed, while for ballistically colliding aggregates as seen in the free molecular regime, the fractal dimension increases to ≈1.95 when thermal forces are the driving mechanism. As aggregates grow in size and are affected more significantly by shear flows, two processes lead to deviations from these trends. First, fragmentation of aggregates can be caused by fluid drag forces exceeding aggregate. Also, drag-imposed bending moments acting on aggregates can cause restructuring and compaction, resulting in higher fractal dimensions.

To understand the significance of each of these processes, we refer to the general Smoluchowski equation describing the change in particle size distribution due to collisions and fragmentation; this is given in Eq. (10) where the left hand side is simplified by the homogeneity assumed here.

Using the relationship for perikinetic flocculation, the collision kernel can be written in terms of the number of primary particles as in Eq. (20). It is worth noting at this point that the terms in parentheses that depend on the aggregate size are alternately dominated by the smaller aggregate

and the larger aggregate. For the perikinetic kernel, it is common to assume that collisions are dominated by those between clusters of similar size, that is $j \approx i$, leading to a distribution peaked at an average cluster size, similar in form to log-normal distrubtions. This quasi-monomodal assumption allows for the determination of an analytic relationship between the kernel homogeneity (λ) of the system which describes how the collision rate of clusters scales with their size:

$$\beta(Ni,Nj) \propto N^{\lambda} \beta(i,j) \tag{63}$$

and the kinetic exponent (z), which describes the growth of the average cluster size $\langle N \rangle$ with time:

$$\langle N \rangle \propto t^{z} \tag{64}$$

that is:

$$z = \frac{1}{1-\lambda} \tag{65}$$

a result that holds generally for quasi-monomodal distributions, not just for the perikinetic kernel. For the perikinetic kernel, $\lambda=0$, so that $z=1$, and the average aggregate size grows linearly in time, a well-known result. In later sections we will show evidence of aggregates in different size regimes having different fractal dimensions under certain conditions leading to the potential for an adjustment here that would account for the different fractal dimensions.

For orthokinetic flocculation, the collision kernel is similarly written in Eq. (12). Within this kernel is the assumption that clusters of size i and j collide at a relative separation of $R_{p,i}+R_{p,j}$. While this may be approximately true for like sized clusters, collisions between large and small clusters ($i>>j$) may not follow this trend. While the perikinetic collision kernel has a relatively weak dependence on the aggregate size, the orthokinetic kernel scales with the cube of the radius of gyration, or with the size of the larger fragment as i^{3/D_f} to leading order. There is thus a transition at larger aggregate sizes from perikinetic to orthokinetic aggregation whenever a shear flow is present. The size dependence of the shear kernel gives an exponential scaling with time under the assumption that the distribution remains monomodal for coalescing particles (Friedlander64, Friedlander-Smoke,Dust,Haze-2000). Interestingly, the interpretation of the relationship between z and λ changes for the orthokinetic kernel. The growth is no longer power law at finite times for fractal clusters, but follows the the form:

$$\langle N \rangle \propto \left(1 - \frac{t}{t'}\right)^{x} \tag{66}$$

$$t'^{-1} = \frac{8\left(\frac{3}{D_f} - 1\right) C^3 \phi \gamma'}{\pi k^{\frac{3}{D_f}}} \tag{67}$$

$$x = \frac{D_f}{D_f - 3} \tag{68}$$

That is, the common assumption of monodispersity would inevitably lead orthokinetically driven systems to divergent behavior at finite times, t'. However, as we shall show, a purely orthokinetic kernel does not produce a monomodal distribution, and this can have significant impact on the kinetics.

7.2 MODEL

For the purpose of this study, we model systems of aggregating particles using discrete particle dynamics with LAMMPS, an open-source molecular dynamics package developed and maintained at Sandia National Laboratories (Plimpton95). Specifically, we have implemented a granular adhesive potential similar in form to that used by Marshall (Marshall08) with components derived previously by Chokshi et al. (Chokshi 93), Dominic and Tielens (Dominic95), Cleary et al. (Cleary98), and Mindlin (Mindlin 49). In this scheme, relative motion between spherical adhesive particle pairs is deconstructed into normal (Chokshi93), rolling (Mindlin49, Cleary98), shearing (Dominic95), and twisting terms, with each mode of motion independently constrained. Potential parameters include the particle radii R and the adhesive surface energy γ as well as the elastic and shear moduli E and G, respectively. In the normal mode:

$$F_n = 4F_c\left[\left(a/a_0\right)^3 - \left(a/a_0\right)^{3/2} \right] \tag{69}$$

with the cutoff force $F_c = 3\pi\gamma R$ and the contact radius between the spherical particles a with equilibrium value $a_0 = \left(\frac{9\pi\gamma R^2}{E} \right)^{1/3}$. The normal force is discontinuous in that up to the point of contact of approaching particles, no force is felt, whereas at first contact there is a finite force present. The same holds of an adhesive particle pair that is separated. For contacting particles, a dissipative normal force is imposed on the normal mode of form

$$F_{n,diss} = -\mu_n v_n \tag{70}$$

where $\mu_n = \gamma_n r_H m_{eff}$, v_n is the normal velocity of the two contacting particles, γ_n is the normal frictional coefficient, $r_H = \left[r_{eff}\left(r_{equil} - r\right) \right]^{1/2}$ is the displacement from equilibrium using a hertzian form, $r_{eff} = (1/r_i + 1/r_j)^{-1}$ is the effective radius, r_{equil} is the equilibrium separation, r the actual separation, and $m_{eff} = (1/m_i + 1/m_j)^{-1}$ is the effective mass of the two particle (i and j) system. Shearing forces are calculated as $F_s = -k_s R_s v_s$ where $k_s = 8Ga$, R_s is the accumulated surface displacement of the two particles along the shearing mode (tangential surface velocities opposite in direction), and v_s is the current direction of the tangential surface velocity in the shear mode. Likewise, a torque is associated with the shearing mode τ_s in order to conserve angular

momentum. Similarly, a rolling torque is calculated as $\tau_r = -k_r R_r$ where $k_r = 4F_c \left(a/a_0\right)^{3/2}$ and R_r is the accumulated surface displacement of the two particles along a rolling mode (tangential surface velocities along same direction). Finally, for the twisting mode, a torque is assigned as $\tau_t = -k_t \Theta_t$ where $k_t = 4Ga^3$ and Θ_t is the accumumulated angular displacement in the twisting mode. Note that no forces are associated with the rolling and twisting modes.

For the current set of simulations, we impose critical conditions on the normal mode only, since the resulting restructuring and fragmentation mechanisms can become highly sensitive to the choice of critical conditions for each mode. These critical conditions are difficult to parameterize to any degree of experimental accuracy. We have implemented the necessary machinery to handle critical conditions for each mode, however, but are reserving a complete investigation of that topic for a future study. We have chosen damping times (τ_{damp}) for each mode that allow no more than 4-5 oscillations for any mode before falling below the thermal noise floor. While it may be desirable to overdamp each of these modes, doing so requires the use of smaller timesteps than those used here in order to ensure system stability. We have chosen adhesive parameters that results in particles that adhere with unit probability under the influence of brownian motion (using the chosen viscosity/temperature) and have a linear persistence length on the order of ten monomers. As for any binding potential, each of the four motional terms is approximately harmonic near equilibrium. To maintain rigidity, a large "spring" constant is required, which necessitates correspondingly small timesteps. It is notrivial to choose parameters that all for both relatively rigid contacts (large spring constants) and sufficient time evolution of the system within a reasonable computational time. That is, for initially dilute volume fractions of particles, which are the systems of interest, it is important to simulate the system for enough time to grow large clusters. In most cases, a brownian kernel is included in our aggregation simulations via a langevin thermostat. For simplicity, we choose to employ the free-draining assumption for particle drag, where each particle feels a drag force $F_{drag} = -3\pi\eta d$ and corresponding delta-function correlated random force F_r, consistent with fluctuation dissipation and standard for the langevin thermostat. We are aware that multiple particle hydrodynamic effects may significantly impact the aggregation process, and we are currently in the process of using a coupled Computational Fluid Dynamics/ LAMMPS code to study hydrodynamic interactions between clusters. However, current computational limitations make such a study necessarily limited to the interaction between a small number of at most moderately sized clusters. For these studies, a purely brownian kernel, ran at $T=10^{-3}$ setss sets a standard for the speed at which aggregation can proceed, that is the slowest mechanism used.

The majority of our simulations have involved initially monodisperse dilute ($\varphi=10^{-3}$) systems of 100,000 particles. For the sake of simplicity, we use scaled units, where all particles are spherical with diameter, $d=1$ and mass $m=1$. For most of our simulations, we set $T=10^{-3}$ and $\eta=5.56x10^{-3}$. As a sidenote, this choice of particle parameters makes the diffusive time of monomers $\tau_D=13.1\tau$ and the momentum relaxation time $\tau_B=19.1\tau$. Due to the low volume fraction of the system, this does not result in Ballistic rather than Diffusive Cluster-Cluster aggregation, even at the earliest times, since there is an initial separation between particles on the order of 10 diameters, necessitating on average several diffusive times before monomers collide and adhere. Adhesive

parameters are set to E=100, G=100, γ=1.0, γ_n=10.0. To increase rigidity we have increased the strength of the twisting, shearing, and rolling mode torques each by a factor of 10, which is mathematically identical to increasing the shear moduli G by the same factor. The maximum stable timestep is $\approx 10^{-4}\tau$. As stated, this parameter set enables significant evolution of the cluster size distribution in the available computational time. With 128 processors we are able to realize on the order of 300M timesteps ($3x10^4\tau$) in a walltime of 96 hr. In some cases, multiple wall-times have been necessary to reach a desirable end-point. For a given brownian kernel (T, μ), we then add an additional orthokinetic kernel by choosing a monomer Peclet number (Pe), defined as:

$$Pe_0 = \tau_{D,0}\gamma' \tag{71}$$

where γ' is the background fluid shear rate and the monomer diffusive time, $\tau_{D,0}$, is given by:

$$\tau_{D,0} = \frac{3\pi\eta d^3}{4k_B T} \tag{72}$$

All simulations are run at constant shear rate, so that due to cluster growth, the Peclet number for clusters grows with time:

$$\begin{aligned} Pe_N &= \tau_{D,N}\gamma' \\ \tau_{D,N} &= \frac{R_g^2}{D_N} \\ D_N &\propto R_H^{-1} \propto R_g^{-1} \\ Pe_N &\propto R_g^3 \propto N^{3/D_f} \end{aligned} \tag{73}$$

As clusters grow they feel increasing amounts of shear stress which can result in both restructuring and fragmentation. These in turn affect the fractal dimension, kinetics of growth, and developing cluster size distributions.

7.3 RESULTS

Of primary interest are two related descriptions of the aggregation process in these sheared systems. The first is the kinetics, that is the evolution or the way the system develops over time, which can be observed through the growth of the average cluster size, the cluster size distributions, and other key parameters. Secondly, we are interested in the structure of these systems, the morphology of sheared flocs as seen throught the fractal dimension, the average coordination number, etc. Obviously, these two concepts are linked. Shearing a system of aggregating particles can affect the structure of the flocs that are formed which can in turn affect the rate at which flocs of certain sizes aggregate. The relative intensity of perikinetic vs. orthokinetic aggregation kernels is also important. Additionally, finite rigidity plays a role. Beyond a certain size limit, aggregates will tend to restructure or fragment, possibly leading to the development of a steady state size distribution. The model we have introduced accounts for restructuring and potentially fragmentation; it also allows the time scale for those phenomena to appear naturally as a function of system parameters.

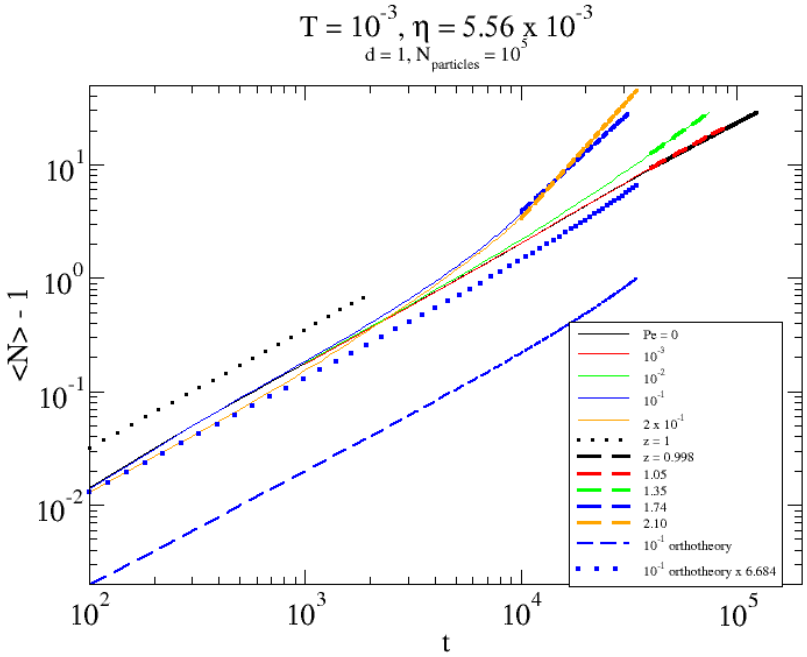

Figure 29. Growth of scaled average cluster size $\langle N\rangle-1$ vs. t for diffusively driven Pe_0=0 and sheared systems with $Pe_0 = 10^{-3}$ to 0.2. Monodisperse orthokinetic predictions are also shown for the case of Pe_0 = 0.1.

In Figure 29 we present results for the growth of the average cluster size as a function of time for sheared systems. 5 different shear rates have been chosen, reported here via the monomer Peclet number ($Pe_0=\tau_{D,0}\dot{\gamma}'$), where $\tau_{D,0}$ is the monomer diffusive time, in this case ≈13.09τ. This figure displays the growth of the scaled average cluster size for each of these shear rates in log-log scale, where by scaled we mean the average size minus 1. It is well-known that since the system is initiated as a monodisperse system of monomers (average size 1), the kinetics is best interpreted through the growth of the scaled average cluster. Results for Pe_0>0.2 are not shown, since in that range, no significant cluster growth is observed. Rather, the shear forces are sufficient to pull apart a dimer, leaving the system primarily composed of monomers; dimers and larger clusters simply cannot form. Figure 29 also shows a power law fit to the late time growth curves for each shear rate indicating the kinetic exponent z. Both Pe_0=0 *and* 10^{-3} have z≈1 as we would expect for systems with a predominately perikinetic kernel. $Pe_0=10^{-2}$ shows an accelerated kinetics where the kinetic exponent rises from 1 at early times to ≈1.35 at the latest times simulated. The higher value of z is a result of the shift from a perikinetic to an orthokinetic mechanism. As stated earlier, this is expected since shear becomes dominant over diffusion as the shear rate increases. For $Pe_0=10^{-1}$, a large increase in the kinetic exponent is observed, rising from ≈1 to 1.74 at the latest times simulated. Doubling the shear rate to $Pe_0=2\times10^{-1}$ increase z to 2.10. It is clear that we do not observe kinetics that are well described as exponential growth (coalescence/monodisperse/orthokinetic) or runaway growth (fractal/monodisperse/orthokinetic) as predicted for purely orthokinetic kernels. However, for the case of Pe_0 = 0.1, this is not

surprising since the divergence time predicted from the above monodisperse orthokinetic theory at this shear rate would be t' $\approx 10^6$, well past our latest simulation time. Of course, this may also be affected by the presence of a perikinetic component, restructuring, fragmentation, or a lack of isotropy in the aggregation mechanism. The first of these is unlikely since the perikinetic kernel becomes less important as the cluster size increases, and the power law fits well describe the growth curves from intermediate to large size clusters present at the end of each run for each shear rate. Restructuring certainly can influence the growth rates, but according to theory, coalescencing clusters (D_f=3.0) represents the slowest form of orthokinetic aggregation, with D_f<3.0 showing runaway growth (divergent at finite times). Fragmentation is also not likely the case, as restructuring is favored over fragmentation with this set of parameters. We propose that the primary reason that aggregation kinetics is better described by power law growth than exponential is the loss of isotropy in the aggregation kernel. That is, the flow constrains the cluster trajectories to reduce the collision cross-section of clusters by aligning them into shear planes due to the formation of Jeffreys orbits. We will discuss this more later. Finite size affects are also not to blame as we have run simulations at a variety of system sizes with similar power law growth.

Figure 30 to Figure 32 show cluster mass (N) vs. radius of gyration (R_g) data for the ensemble of clusters seen at three different shear rates (Pe_0=0,10^{-2}, *and* 10^{-1}) and at a range of times. The mass fractal dimension D_f is determined as the slope of the best fit line through the data in log-log. In Figure 30 we observe a fractal dimension of ≈1.6 for small cluster sizes at all times for Pe_0=0, which is the regime of diffusion limited aggregation (DLCA). We know from previous studies that there are significant variations in the fractal mass/size scaling relationship for small clusters, specifically for DLCA aggregates when N<16, thus a slightly reduced D_f may be expected. For intermediate to large clusters at intermediate times, we observe D_f=1.8, consistent with standard DLCA aggregates as observed in a host of previous studies. The fractal dimension evolves to D_f=2.0 at late simulation times for large clusters, evidencing some level of restructuring for large clusters, a result of the semi-rigid adhesive parameter set used in this study. Figure 31 displays results for Pe_0=10^{-2}, where we observe some interesting features. Beyond N>10, the spread of the data increases, which we attribute to a bifurcation in the possible cluster structures; a spread in D_f develops. At each of the times shown, we obtain two different power law fits to the data, one with D_f≈1.3 for all small clusters of size N<10 and extending beyond this into the lower lobe of the data for

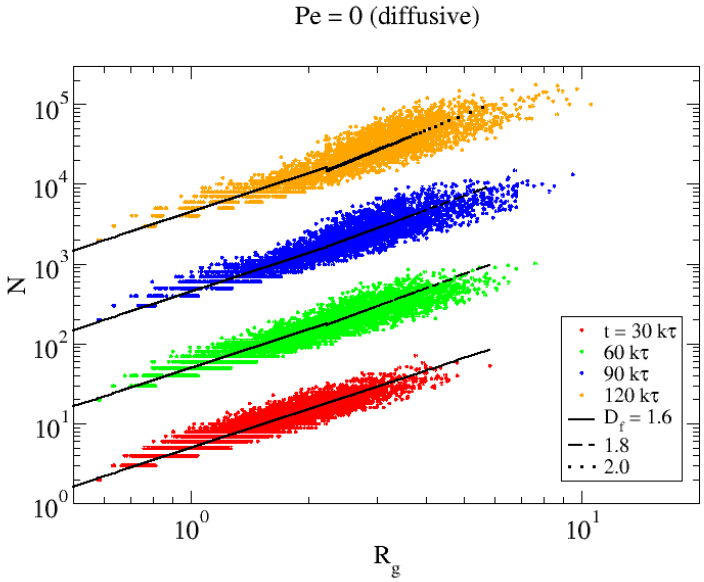

Figure 30. Mass *N* vs. radius of gyration R_g for ensemble of clusters in diffusive system at t = 30,000τ. Power law fit shows D_f.

N>10. We also find a fit to the upper lobe of the ensemble for *N*>10 with D_f evolving from 2.2 at early times to 2.7 at late times. Several physical processes with competing timescales are at work. Steady shear favors the formation of lower D_f aggregates for clusters small enough that shear stresses are insufficient to lead to significant cluster fragmentation or restructuring. This is due to the fact that starting at the point when dimers form from the initial monomer population, clusters begin to orient themselves in the shear flow so that they rotate with the axis of rotation parallel to the vorticity direction; that is, clusters take on Jeffreys orbits. Since the particle velocities within a rotating cluster are larger at the edges furthest from axis, cluster collision and subsequent aggregation will favor long, narrow, highly anisotropic clusters with low D_f ..Competing with this is the fact that for high shear rates and/or larger aggregates, shear stresses cause restructuring in the clusters, increasing D_f, reducing anisotropy in the shear gradient plane where shear torques are strongest. Due to complex hydrodynamic interactions and competing collisional/orientational/restructuring timescales, the presence of at least some restructuring into the vorticity direction can occur. We would expect and do observe (shown later) that restructured clusters are thinner in the vorticity direction than in the shear and shear gradient directions. Figure 32, for $Pe_0=10^{-1}$ shows similar features to Figure 31, with the bifurcation in D_f even more apparent than for $Pe_0=10^{-2}$. The lower lobe still shows $D_f\approx1.3$, but the upper lobe now has $D_f\approx2.8$, very near the limit of a completely restructured, nearly coalesced ($D_f=3.0$) cluster, even at relatively early times. Clearly, this is a result of larger shear stresses. For these systems there are several timescales involved, including a diffusive, shear, collisional, and restructuring timescale. Due to the statistical nature of the aggregation and random configuration of the system, clusters can collide with other clusters at any stage during the process of their restructuring. This collision can then influence the restructuring process in a complex way. What is clear is that quasi-linear clusters are not stable for any reasonable amount of time above a

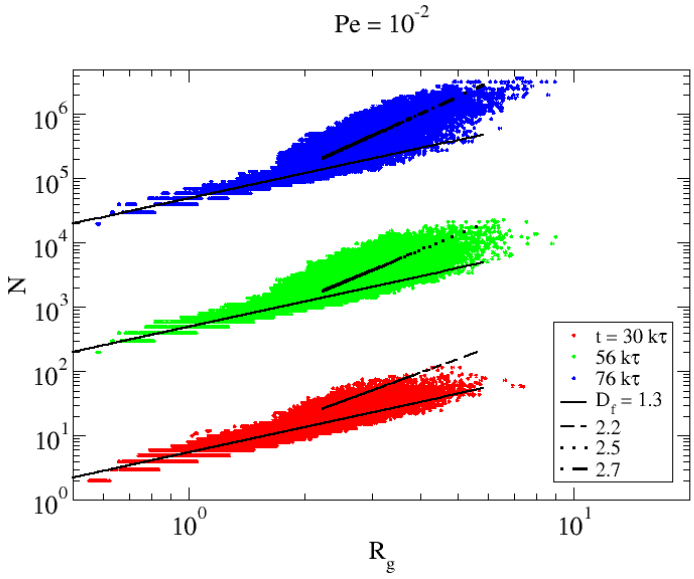

Figure 31. Mass *N* vs. radius of gyration R_g as in Figure 30 or sheared system at $Pe_0=10^{-2}$ at t = 30,000τ. Power law fit shows D_f. Bifurcation in ensemble apparent for clusters above $N \approx 10$.

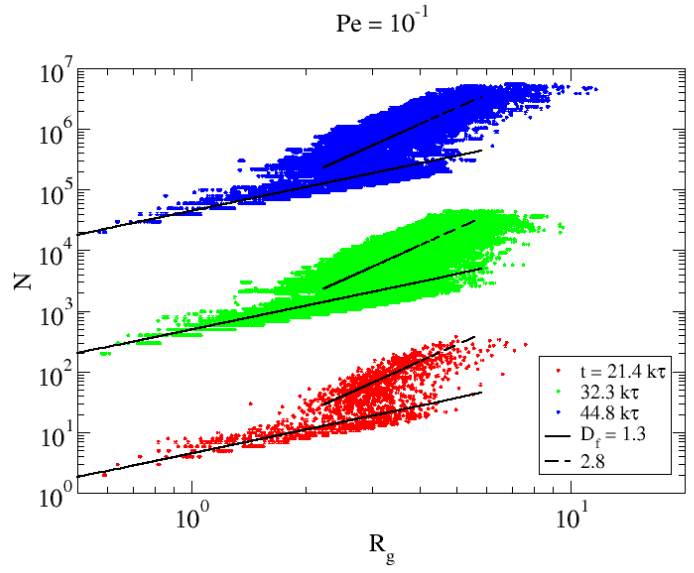

Figure 32. Mass *N* vs. radius of gyration R_g as in Figure 30 or sheared system at $Pe_0=10^{-1}$ at t = 21,000τ. Power law fit shows D_f. Bifurcation more apparent.

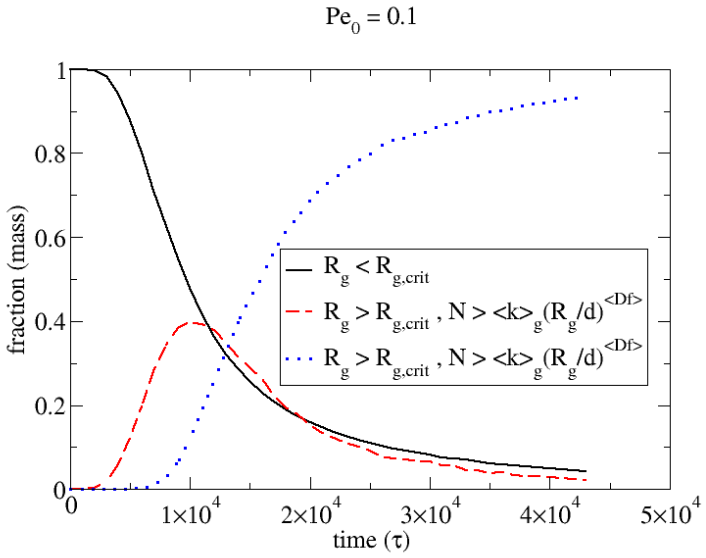

Figure 33. For $Pe_0=10^{-1}$, shown in Figure 32, fraction of mass of clusters with small R_g, large R_g with low D_f, and large R_g with high D_f. $R_{g,crit}$ ≈2 is the radius of gyration at which bifurcation of the ensemble is observed. $\langle k\rangle_g$ is the geometric average of the prefactors found from the two branches of the ensemble with $R_g>R_{g,crit}$. $\langle D_f\rangle$ is the arithmetic average of the fractal dimension of the two branches above $R_{g,crit}$.

certain size since the shear will tend to restructure them quickly, and compact structures are unlikely for $N<5$ due to Jeffrey's orbits. In the intermediate size range, clusters tend to fall onto one of the two distributions (quasi-linear or compact), but the division is not sharp, indicating a spread of restructuring times, and an overlap in timescales between that required for restructuring and that required for a collision with another cluster. Figure 33 displays the time evolution of the populations of clusters in three regimes for the case of $Pe_0 = 0.1$. The first is for clusters that lie below the length scale of bifurcation ($R_g \approx 2$). The second for the clusters that have $R_g>2$ but lie along the original $D_f=1.3$ branch. The final is for the clusters with $R_g>2$ but $D_f=2.8$. At late times, nearly all of the mass ends up in these large D_f, highly restructured flocs.

Figure 34 (a) shows cluster size distributions for $t=0$ to $t=30{,}000\tau$ for the perikinetic case plotted as $n(N)$ or the number density of cluster in a range of size N vs. N, where for statistical purposes, clusters have been binned into bins with exponential spacing. The results are similar to those seen from Monte Carlo simulations of diffusion limited cluster-cluster aggregation In Figure 34 (b) we scale the cluster size N (x-axis) by the average size $\langle N\rangle$ at the time of the sample and multiply $n(N)$ by $\langle N\rangle^2$, which collapses the data for $t>6000$ onto a master curve of the form $Ax^{-\lambda}exp\left[-(1-\lambda)x\right]$ with λ the aggregation homogeneity. We remove the earliest time data since at early times, the size distribution has not yet converged to a self-preserving form. For a perikinetic kernel, we expect to get $\lambda=0$, and we find $\lambda\approx-0.05$ for $N/\langle N\rangle>1$, the valid range of this scaling form. In reality, a fit to the entire distribution gives nearly the same fit with $\lambda\approx-0.07$. In either case, the results are in good agreement with perikinetic expectations.

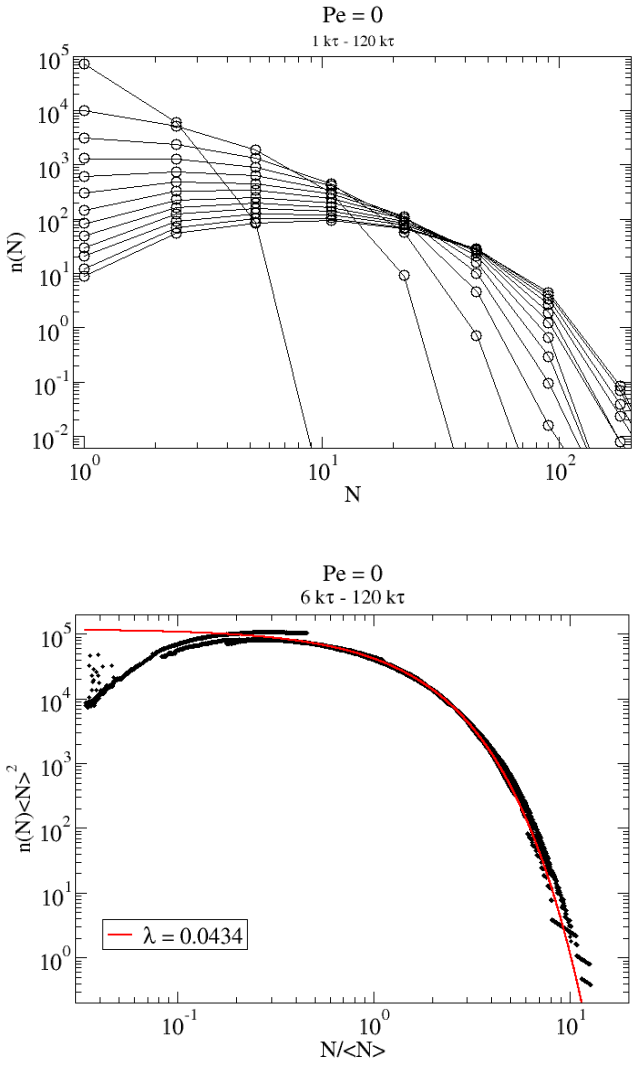

Figure 34. a) (top) Evolution of cluster size distributions for diffusive system Pe_0=0 from t = 0 to t = 30,000τ b) (bottom) cluster size distributions with size N normalized by average size, $\langle N \rangle$, and number of clusters of size N, $n(N)$, multiplied by $\langle N \rangle^2$. Collapse onto master curve is apparent. Fits to scaling form with prefactor, A, and homogeneity, λ, are also displayed.

Figure 35(a) shows size distribution data for the case of Pe_0=0.1. Here the shape of the distribution is quite different than the perikinetic case and is clearly better described as a power law distribution with perhaps an exponential fall off for the largest clusters. It is obviously not similar to a monomodal distribution, which could in part explain the differences we observe between our kinetics and theoretical predictions of exponential or runaway kinetics for orthokinetic kernels. If collisions are not dominated by clusters of similar sizes colliding then the Smoluchowski equation cannot be collapsed onto a single term and the evolution of the average cluster size cannot be determined analytically even with the simple assumptions of the

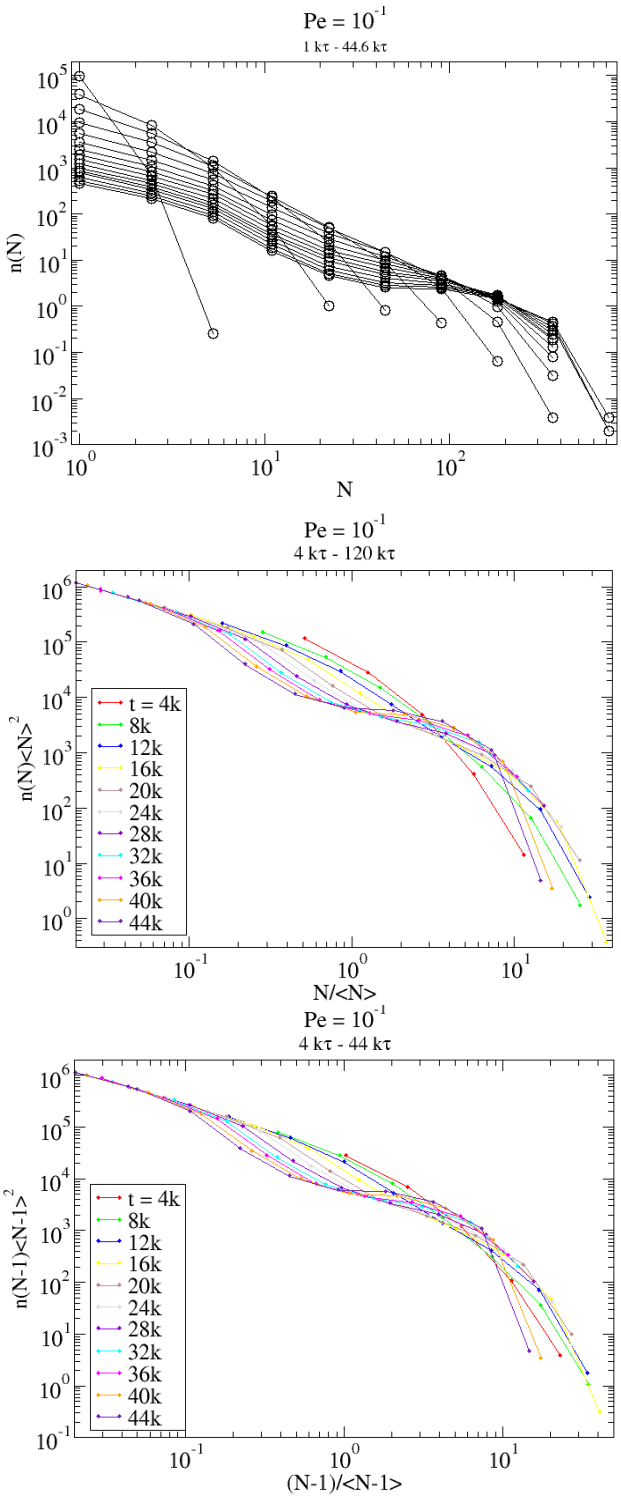

Figure 35. a) (top) Evolution of cluster size distributions for sheared system at $Pe_0=10^{-1}$ from t = 0 to t = 21,000τ b) (middle) cluster size distributions with size N normalized by average size, $\langle N \rangle$, and number of clusters of size N, $n(N)$, multiplied by $\langle N \rangle^2$. Size distributions do not collapse well onto master curve c) (bottom) cluster size distributions with scaled size, $N-1$, normalized by scaled average size, $\langle N \rangle-1$, and number of clusters of scaled size $N-1$, $n(N-1)$, multiplied by $(\langle N \rangle-1)^2$. Size distributions collapse somewhat better. Fit to scaling form gives λ=0.82 (not shown).

orthokinetic kernel. This would be true whether or not $Df<3$ (coalescence). Recent population balance studies by this group indicate that when restructuring is not included as part of the kernel, power-law distributions are observed when using orthokinetic kernels. In Figure 35(b) we attempt to collapse our size distribution data onto a scaling form with little success. This is consistent with recent orthokinetic studies that show difference in early time orthokinetic behavior to late time. However, if one takes into account, as we do in the kinetics results, that the average size begins at 1, and instead scale by the average scaled cluster size $<N>-1$, we do get the late time data to collapse somewhat better as seen in Figure 35(c). Here we find $\lambda \approx 0.82$. Using the relation $z = (1 - \lambda)^{-1}$, we would expect $z \approx 5.6$. However, we have previously seen that even at the latest times for this shear rate $z<2$. This indicates a break in the relation between z and λ, where if we remember the relation was derived by assuming a quasi-monodisperse size distribution. This provides some further support to the notion that the monodisperse size distribution is inconsistent with the orthokinetic kernel.

Figure 36(a)-(c) shows the evolution of the coordination numbers of particles (number of adhesive contacts) for the same systems as in Figure 30 through Figure 32. For the perikinetic case, Figure 36(a), the average coordination number begins at 0 (monodisperse system of monomers), grows to 1 (mostly dimers), and shifts to 2 at late times with a small number of particles with coordination number 3 and 4 at late times. A coordination number of 2 is consistent with extended fractal structures, in this case with $D_f \approx 1.6$. We see similar evolution at $Pe_0=10^{-2}$, with the difference that for late times the population of particles with coordination numbers 3 and 4 is increased. This is consistent with the larger fractal dimension $D_f \approx 2.1$ we observe at this shear rate at late times for large clusters. Finally, in Figure 36(c) we observe that the average coordination number does not remain at 2 but shifts to 6 or higher at late times indicating significant restructuring and compactification, which we confirm through the fractal dimension of $D_f = 2.8$ for large clusters at late times for this shear rate. In Figure 36(d) we show the growth in individual coordination numbers for $Pe_0 = 0.1$. As in Figure 36(c), at late times, the $Pe_0=0$ case shows a large amount of restructuring, with coordination numbers trending toward values larger than 6.

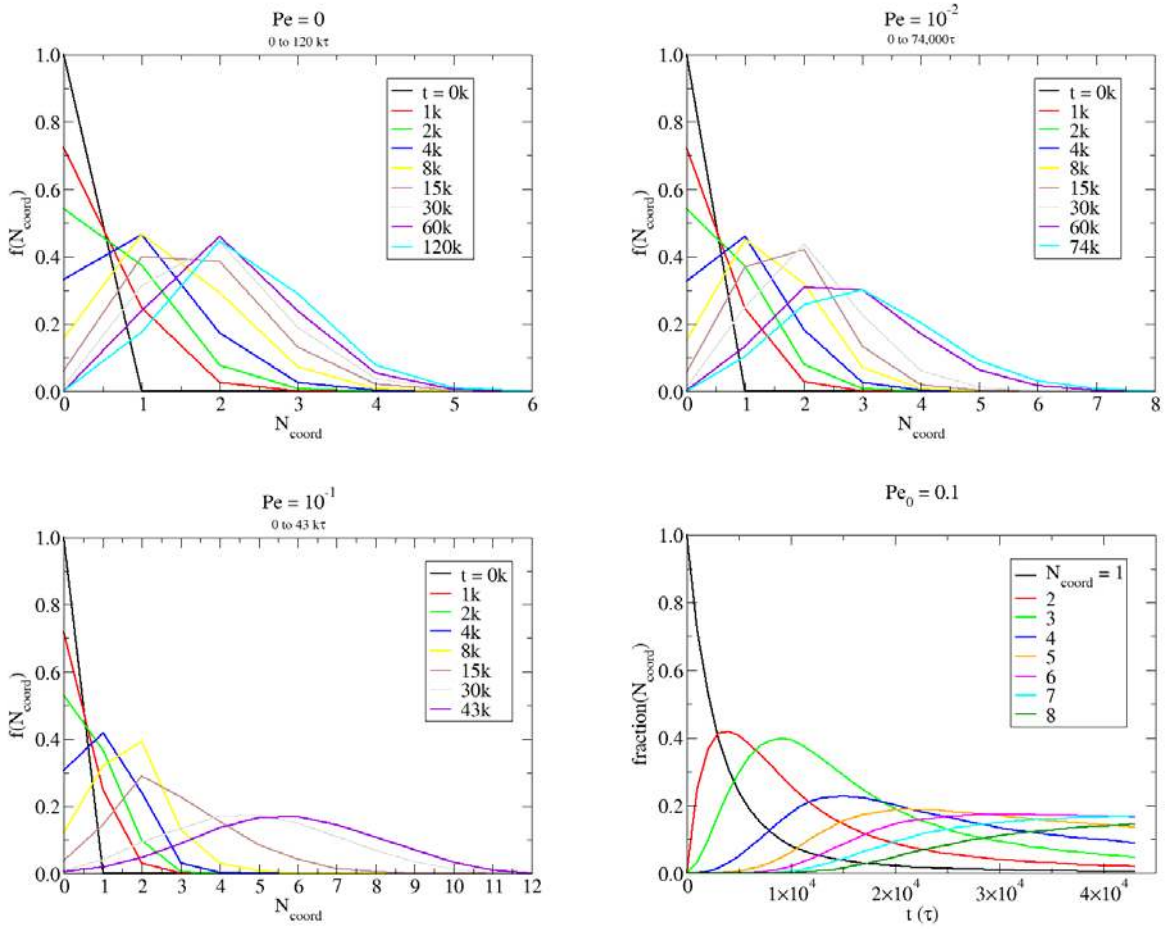

Figure 36. a) (top left) Coordination number histogram for all particles in diffusive system from *t*=0 to *t*=30,000τ. b) (top right) same for sheared system at $Pe_0=10^{-2}$. c) (bottom left) same for sheared system at $Pe_0=10^{-1}$ from *t*=0 to *t*=21,000τ. Compactification of clusters is apparent at late times from shift to larger coordination numbers. d) (bottom-right) Evolution of individual coordination number fractions vs. time for $Pe_0=0.1$ case.

Figure 37 shows two views of the late-time cluster morphologies in the purely kinetic case. The system is isotropic, looking statistically identical from any orientation. A closeup view of this system at late times demonstrates the branched fractal appearance of the flocs formed as a result of thermal diffusion. These structures look qualitatively similar to those observed in many other studies of diffusively limited aggregation. In Figure 38, the late-time cluster morphologies of the sheared $Pe_0=0.1$ case is shown. We immediately observe the anisotropy of the system. The system appears different, as do the individual clusters, when viewed along the voriticity direction as opposed to the shear direction. This, as mentioned earlier, is a result of hydrodynamic forces which tend to align newly formed clusters in Jeffrey's orbits, so that the rotational axis of the clusters is along the vorticity direction. This axis orientation represents the axis through the cluster center for which the cluster has the largest moment of inertia.

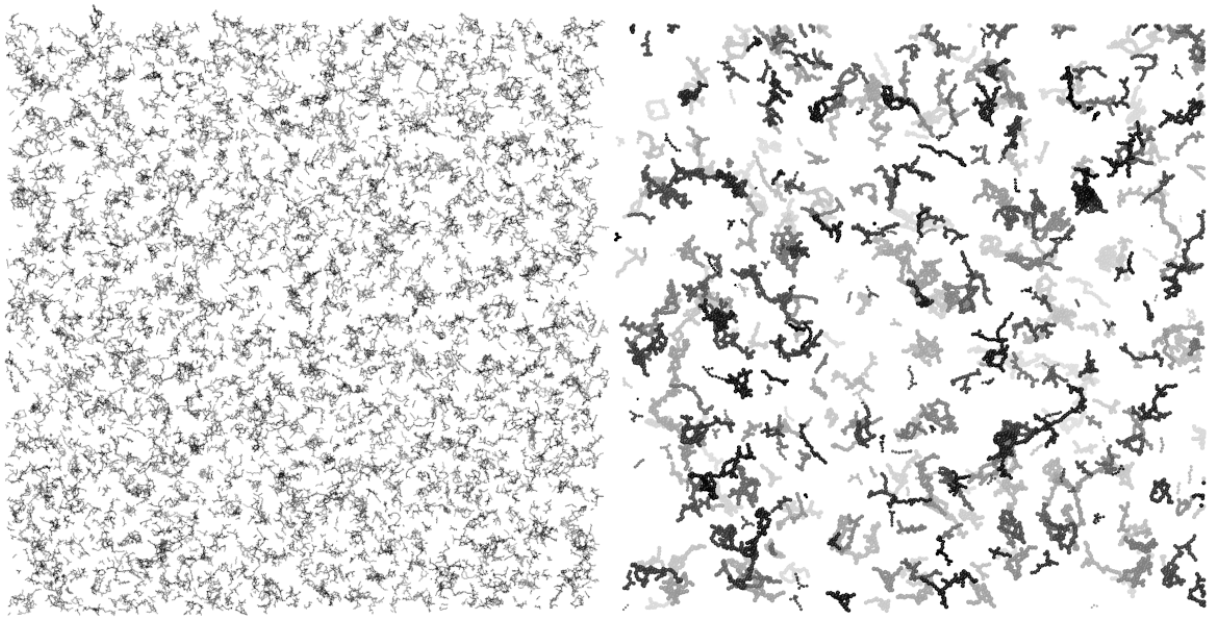

Figure 37. a) (left) Snapshot of diffusive system Pe_0=0 at t=30,000τ b) (right) 150x150x150 d^3 section of system showing individual cluster morphologies.

7.4 SUMMARY

We have successfully demonstrated a model of aggregation in adhesive systems experiencing diffusion and steady shear. Under the purely perikinetic case, we find good agreement in the morphologies (D_f) of structures that are formed, the kinetics of aggregation, and the evolution of the cluster size distribution with well established results. For systems where shear plays a role, we have observed additional physical mechanisms which affect these same metrics. We find power law kinetics with exponents that are shear-rate dependent. We also observe the formation of an anisotropic particle field. Additionally, restructuring is observed to play a large role in these semirigid clusters, leading to large fractal dimensions at high shear rates. Restructuring, as seen in the evolution of the particle coordination numbers, is found to be a dynamic process with timescales that overlap aggregation timescales. These mechanisms affect the kinetics and resulting size distributions in ways that have not been previously fully explained by sectional models. We believe the anisotropy that develops in the particle field resulting from cluster alignment into Jeffreys orbits plays an important role in the growth kinetics and developing size distribution. This study is one of, if not the first of its kind to attempt to treat the full physical description of aggregation of low concentration adhesive particles in a background fluid, including resolving the semirigid adhesive contact between individual particles.

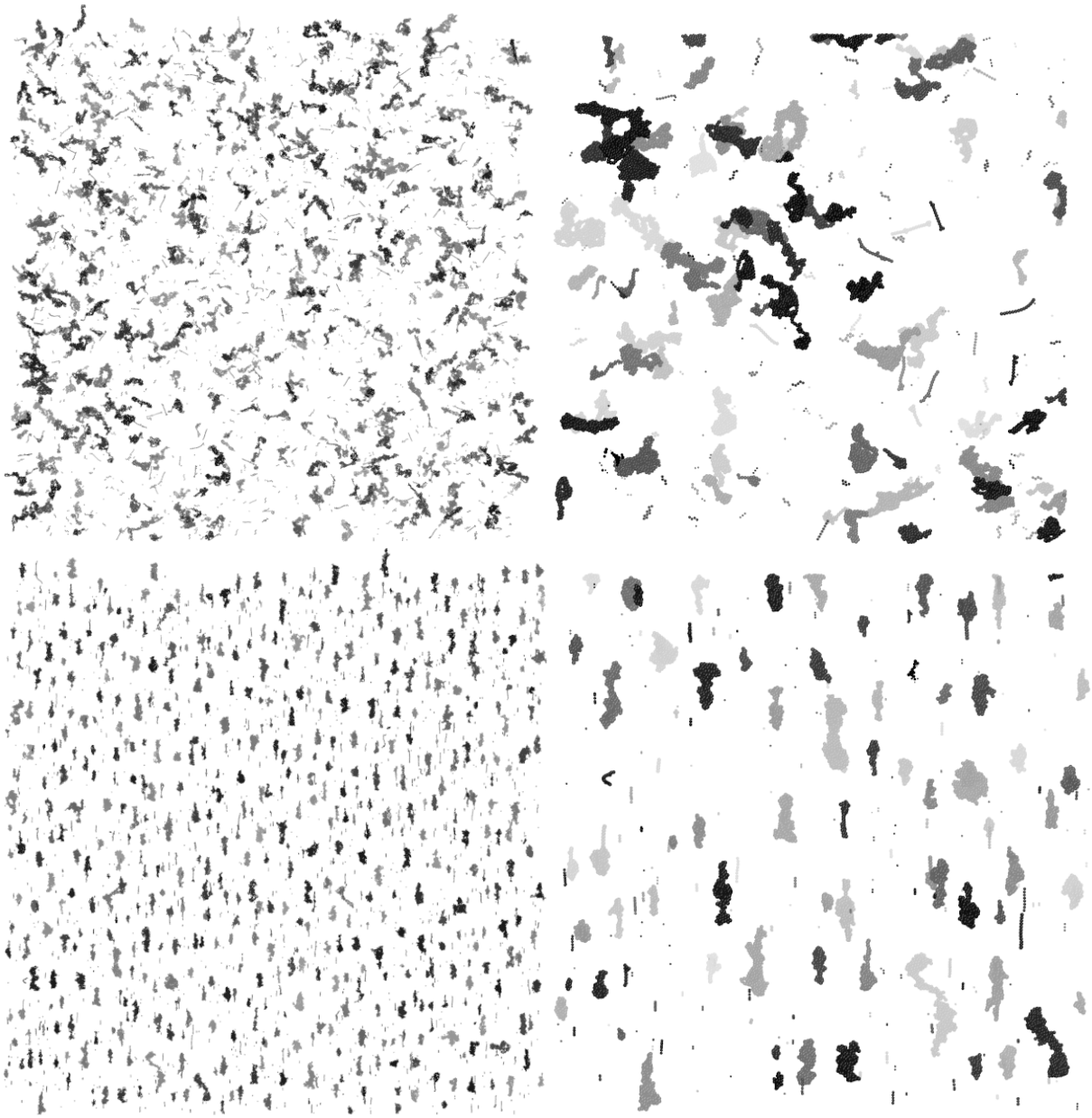

Figure 38. a) (top left) Snapshot of sheared system with $Pe_0=10^{-1}$ at t=21,000τ looking down on x-y plane. Shear velocities are along x, increasing in y b) (top right) 150x150x150 d^3 section of system showing individual cluster morphologies also in x-y. a) (bottom left) Snapshot of same system now looking down at y-z plane b) (bottom right) 150x150x150 d^3 section of system showing individual clusters, looking down at y-z plane.

8 CONCLUSIONS

Algae flocculation is a potential means to effectively and efficiently separate algae from its growth media. To do so, the tendency of the algae surface to generate a net anionic charge that stabilizes the suspension must be overcome and the algae must be brought in contact with sufficient frequency to grow flocs. This work improves our understanding and develops tools to predict both the surface processes and the floc evolution.

To better understand the surface charge, we report measurements of surface functional group concentrations and related these to the flocculant requirements. These functional group concentrations are found to vary with the cultivation conditions and with the algae life cycle stage; higher surface functional group concentrations are found during exponential growth than during stationary phase with even fewer measured during the declining phase. This suggests that cultivation conditions and harvesting time can have a significant impact on the flocculant requirements.

We also measure boundaries on the range of effective flocculation that are determined by the change in surface state (transition to/from deprotonation of surface groups). To predict this we developed models of the surface charge both as a function of the pH and as a function of the ionic content of the growth media. These models are presented in the context of PHREEQC. Because the algae surface also interacts with precipitates, models for precipitate surface states are developed for both traditional inorganic flocculants like $FeCl_3$ and for the precipitates that form from bulk salts. Bulk salts are those available in sufficient concentrations in natural saline and brackish waters to cause precipitation at high pH and that have been associated with autoflocculation of algae. These models show the favorable autoflocculation conditions as a function of the relative ion concentrations, and are in agreement with observed autoflocculation.

When the algae concentration is sufficiently high, alga-alga interactions are frequent enough that the collision efficiency can be reduced without a penalty in the harvesting efficiency. Since high collision efficiency is brought about by the addition of flocculants, the flocculant per biomass is found to be reduced under high concentrations, a desirable result. The collision frequency is known to be significantly affected by the fractal structure of the flocs and we have sought to understand this in a multi-pronged approach. The focus has been on the observed change in floc structure due to shear. Initial flocs tend to be less dense with shear energy from the flow causing flocs to restructure as they grow into denser clusters. This leads to potentially reduced cross sections but at the same time to faster settling velocities and potentially greater water removal.

The floc structure is observed to change as a function of the shear rate in highly controlled Couette flow measurements of the shear-driven aggregation. At the same time, the floc distributions are found to reach a self-similar state. Similar observations are made in particle dynamics simulations in the context of LAMMPS.

To study this restructuring in the high-fidelity simulation environment provided by LAMMPS we have introduced a set of potentials that provide rolling, twisting and shearing resistance in addition to adhesion. One important result to come out of this is the dependence of the

restructuring on random intra-floc motions. It was realized that the typical computational methods to damp out intra-floc vibrations artificially reduce the restructuring that can occur even in the absence of shear. To overcome this we present a new means of thermostating internal modes and show that this significantly alters the floc morphology, radius of gyration and internal particle coordination number.

Additional LAMMPS simulations carried out with the addition of shear energy show the effect of this shear energy on the growth and restructuring process. Of particular note is the clear identification of separate floc structures for early floc growth and for later post-restructured flocs. The early floc growth is characterized by a relatively low fractal dimension. As the flocs grow to a size where the flow shear energy is significant relative to the floc strength, the flocs restructure to a higher fractal dimension and simultaneously the average internal particle coordination number increases. Different degrees of restructuring are observed both with time and with the magnitude of the shear energy.

Ultimately, the evolution of flocs occurs over much longer time and length scales than can be simulated in LAMMPS, and there is a need to provide macroscale models of the floc growth process. This is done using the sectional modeling approach to predicting the evolution of the floc size distribution. We present a general form suitable for use with varying floc structure (fractal dimension and prefactor) and varying floc density. Floc growth predictions varying with different fractal dimensions are presented. Particular attention is paid to the potential fragmentation and restructuring dependencies, and these are analyzed to identify the degree of restructuring that might be expected at different degrees of shear.

9 APPENDIX A: PHREEQC INPUT FILE FOR SEAWATER AUTOCOAGULATION

The PHREEQC input file below calculates pH-dependent speciation of algae surfaces and hydroxyapatite, calcite, and $Mg(OH)_2$ surfaces, allowing the potential for autocoagulation to be estimated.

```
TITLE Autocoagulation simulations.  Patrick V. Brady, Sandia National Labs
PHASES
Hydroxylapatite
        Ca5(OH)(PO4)3 +4.0000 H+  =  + 1.0000 H2O + 3.0000 HPO4-- + 5.0000 Ca++
        log_k           -3.0746
Fe(OH)3
Fe(OH)3 + 3H+ = 3H2O + 1Fe+3
log_k  4.
SOLUTION_SPECIES
H2O + Ca+2  =  CaOH+ + H+
log_k -12.85
delta_h 18.31 kcal
Mg+2 + H2O = MgOH+ + H+
log_k         -11.44
delta_h 15.952 kcal
SURFACE_MASTER_SPECIES
Alg_c  Alg_cOOH
Alg_p  Alg_pH
Alg_n  Alg_nH
Hap_c  Hap_cOH
Hap_p  Hap_pO3H2
Bru_m  Bru_mOH
Cc_c   Cc_cOOOH
Cc_m   Cc_mOH
SURFACE_SPECIES
Alg_cOOH = Alg_cOOH
log_k 0.0
Alg_pH = Alg_pH
log_k 0.0
Alg_nH = Alg_nH
log_k 0.0
Hap_cOH = Hap_cOH
log_k 0.0
Hap_pO3H2 = Hap_pO3H2
log_k 0.0
Bru_mOH = Bru_mOH
log_k 0.0
#Algae amine group
Alg_nH + H+ = Alg_nH2+
log_k 9.9
#Algae phosphoryl group
Alg_pH = Alg_p- + H+
log_k -7.7
#Algae carboxylate group
Alg_cOOH = Alg_cOO- + H+
log_k -3.9
Alg_cOOH + Ca+2 = Alg_cOOCa+ + H+
log_k -3.8
delta_h 1.171 kilojoules
Alg_cOOH + Mg+2 =  Alg_cOOMg+ + H+
log_k   -3.4781
delta_H      -8.42239     kJ/mol
Alg_cOOH + Fe+3 =  Alg_cOOFe+2 + H+
log_k   -1.54
Alg_cOOH + FeOH+2 =  Alg_cOOFeOH+ + H+
log_k   -3.34
```

```
Alg_pH + Ca+2 = Alg_pCa+ + H+
log_k -0.7
Alg_pH + Mg+2 = Alg_pMg+ + H+
log_k -0.6
# BRUCITE
Bru_mOH = Bru_mO- + H+
log_k -12.0
Bru_mOH + H+ = Bru_mOH2+
log_k 10.0
# HYDROXYAPATITE
Hap_cOH + H+ = Hap_cOH2+
log_k 8.41
Hap_pO3H2 = Hap_pO3H- + H+
log_k -1.11
Hap_cOH + HPO4-2 + H+ = Hap_cPO4H- + H2O
log_k 11.63
Hap_pO3H2 + Na+ = Hap_pO3Na- + 2H+
log_k -11.08
Hap_pO3H2 + Ca+2 = Hap_pO3HCa+ + H+
log_k -0.7
Hap_pO3H2 + Mg+2 = Hap_pO3HMg+ + H+
log_k -0.7
# CALCITE
Cc_mOH = Cc_mOH
log_k 0.0
Cc_cOOOH = Cc_cOOOH
log_k 0.0
Cc_cOOOH = Cc_cOOO- + H+
log_k -5.1
delta_H -2.8 kilojoules
Cc_cOOOH + Ca+2 = Cc_cOOOCa+ + H+
log_k -2.6
delta_H 7.4 kilojoules
Cc_cOOOH + Mg+2 = Cc_cOOOMg+ + H+
log_k -2.6
delta_H 8.0 kilojoules
Cc_mOH + H+ = Cc_mOH2+
log_k 11.85
delta_h -60.7 kilojoules
Cc_mOH + CO3-2 + H+ = Cc_mCO3- + H2O
log_k  17.1
delta_h -46.7 kilojoules
Cc_mOH2+ + SO4-2 = Cc_mSO4- + H2O
log_K 2.1
delta_H 11.6 kilojoules
Cc_mOH2+ + HPO4-2 = Cc_mHPO4- + H2O
log_K 2.7
Cc_mOH2+ + HPO4-2 = Cc_mPO4-2 + H+ + H2O
log_K -5.3
SOLUTION 1
# Seawater
-units mmol/kgw
-temp 25
pH 5.0
Ca 10.
P 0.02
Fe(3) 0.0001
K 10
Mg 52
C(4) 2.
S(6) 28.
Na 469.   charge
Cl 546.
```

```
PHASES
Fix_H+
H+ = H+
log_k 0.0
KNOBS
-iterations 150
-convergence_tolerance 1e-12
-tolerance 1e-14
-step_size 10.
-pe_step_size 5.
-diagonal_scale TRUE
SURFACE 1
Alg_cOOH 0.002 10.  20.
Alg_pH 0.0008
Alg_nH 0.0014
Hap_cOH Hydroxylapatite equilibrium_phase 0.072 1e4
Hap_pO2H2 Hydroxylapatite equilibrium_phase 0.05 1e4
Bru_mOH Brucite equilibrium_phase 0.167 1e4
Cc_cOOOH Calcite equilibrium_phase 0.041 1e4
Cc_mOH Calcite equilibrium_phase 0.041 1e4
USE solution 1
USE surface 1
EQUILIBRIUM_PHASES 1
Fix_H+ -6.0 HCl 10.0
Calcite      0.0    0.0
Brucite 0.0 0.0
Hydroxylapatite     0.0    0.0
Fe(OH)3 0.0 0.0
END
USE solution 1
USE surface 1
EQUILIBRIUM_PHASES 1
Fix_H+ -8.0 NaOH 10.0
Calcite      0.0    0.0
Brucite 0.0 0.0
Hydroxylapatite     0.0    0.0
Fe(OH)3 0.0 0.0
END
USE solution 1
USE surface 1
EQUILIBRIUM_PHASES 1
Fix_H+ -10.0 NaOH 10.0
Calcite      0.0    0.0
Brucite 0.0 0.0
Hydroxylapatite     0.0    0.0
Fe(OH)3 0.0 0.0
END
USE solution 1
USE surface 1
EQUILIBRIUM_PHASES 1
Fix_H+ -12. NaOH 10.0
Calcite      0.0    0.0
Brucite 0.0 0.0
Hydroxylapatite     0.0    0.0
Fe(OH)3 0.0 0.0
END
```

10 APPENDIX B: FRACTAL FLOCS

Flocs tend to form more dispersed shapes than a dense sphere, so that a floc of i particles may be larger than a dense sphere of that many particles. A characteristic dimension of such a floc, r_f, is given by

$$r_f = \left(\frac{3v_0}{4\pi}\right)^{1/3}\left(\frac{i}{b}\right)^{1/D} \tag{74}$$

where v_0 is the volume of a primary particle, a single cell, D is the fractal dimension and b is a prefactor. More typically the definition of the mass fractal dimension is given in terms of the radius of the primary particle, a_0,

$$i = b\left(\frac{r_f}{a_0}\right)^D \qquad \text{with} \quad a_0 = \left(\frac{3v_0}{4\pi}\right)^{1/3} \tag{75}$$

This expression shows how the number of primary particles in a floc is related to the floc (fractal) radius and the fractal dimension and the prefactor.

The volume of particles in a floc is proportional to i

$$\text{filled volume} = iv_0 = b\left(\frac{r_g}{a_0}\right)^D v_0 \tag{76}$$

while the volume that the floc encompasses (including the pore-filling fluid) is proportional to $i^{3/D}$

$$\text{floc volume} = \frac{4\pi}{3}r_g^3 = \frac{4\pi}{3}a_0^3\left(\frac{i}{b}\right)^{3/D} \tag{77}$$

so that the volume fraction of particles within the floc is

$$\phi_f = \frac{b^{3/D}}{i^{\frac{3-D}{D}}} = \frac{b}{\left(\frac{r_g}{a_0}\right)^{3-D}}. \tag{78}$$

With fractal dimensions of 1.0, 1.5, 2.0, 2.5 and 3.0, we get volume fractions proportional to the number of particles in the floc as follows. The effective density, given below, also scales with the particle size.

D	ϕ_f	$\Delta\rho_e \propto r_f^{D-3}$	$\Delta\rho_e(r_f = 10r_c)$
1.0	$\phi_f \propto i^{-2}$	$\Delta\rho_e \propto r_f^{-2} \propto i^{-2}$	$0.01(\rho_c - \rho_w)$
1.5	$\phi_f \propto i^{-1}$	$\Delta\rho_e \propto r_f^{-1.5} \propto i^{-1}$	$0.03(\rho_c - \rho_w)$
2.0	$\phi_f \propto i^{-1/2}$	$\Delta\rho_e \propto r_f^{-1} \propto i^{-1/2}$	$0.1(\rho_c - \rho_w)$
2.5	$\phi_f \propto i^{-1/5}$	$\Delta\rho_e \propto r_f^{-0.5} \propto i^{-0.2}$	$0.3(\rho_c - \rho_w)$
3.0	$\phi_f = 1$	$\Delta\rho_e \propto r_f^0 \propto i^0$	$1(\rho_c - \rho_w)$

The effective buoyancy of a floc can be interpreted using the volume fraction of the particle phase times the particle phase density,

$$\rho_e = \phi\rho_c, \quad \Delta\rho_e = \phi(\rho_c - \rho_w) \tag{79}$$

where ρ_e is the effective density, ρ_c is the cell density, ρ_w is the water density. When settling velocity is used to compute the effective density, one gets a correlation between $\Delta\rho_e$ and the apparent dimension, r_f. like

$$\Delta\rho_e \propto r_f^{D-3} \tag{80}$$

showing how the fractal dimension might be determined from this settling data. There is then a substantial reduction in the settling velocity for large fractal particles as can be computed from the above table.

We can also estimate an effective area of connectedness within the floc. This is obtained in a manner directly analogous to the floc volume fraction by defining an area of particles in a floc cross section as

$$\text{particle area in cross section} = \pi a_o^2 i^{2/3} = \pi a_o^2 b^{2/3} \left(\frac{r_g}{a_0} \right)^{2D/3} \tag{81}$$

while the area of the floc is proportional to $i^{2/D}$

$$\text{floc area} = \pi r_g^2 = \pi a_0^2 \left(\frac{i}{b} \right)^{2/D} \tag{82}$$

so that the area fraction of particles within the floc is

$$\alpha_f = \phi_f^{2/3} = \frac{b^{2/D}}{i^{\frac{2}{3}\left(\frac{3-D}{D}\right)}} = \frac{b^{2/3}}{\left(\frac{r_g}{a_0} \right)^{\frac{2(3-D)}{3}}}. \tag{83}$$

11 APPENDIX C: CAPABILITIES ADDED TO LAMMPS DISCRETE ELEMENT MODELING PACKAGE

11.1 JKR-TYPE ADHESIVE GRANULAR POTENTIAL:

This capability allows for resolution of all modes of relative motion of pairs of adhesively bound particles (normal, rolling, shearing, twisting) as well as critical contact force and dissipation in those modes. The full scope of this potential is described in the included modeling summary. This capability is applicable to any system of adhesive particles from algae cells to soot and other aerosols or suspended particulate matter. We have already started pursuing funding in some of these other application spaces based on this new capability.

11.2 GRANULAR THERMOSTATING:

We enhanced our model of granular materials by developing a thermostating mechanism whereby dissipative force fields acting on pairs of particles receive stochastic thermal fluctuations. This ensures that fluctuation-dissipation holds on the system of particles and temperatures are consistent throughout the simulation domain. To our knowledge, this is the first such consistent treatment of temperature for dissipative binary granular force fields.

11.3 TAYLOR-COUETTE FLOW FIELD:

Two distinct methods of modeling Taylor-Couette flow fields (pre-turbulent) were added to the LAMMPS code base. The first allows the user to specify a shear gradient and vortex intensity. This case is used in a simulation with periodic boundaries, thus no Taylor number is specified. The second method allows for a full 3D description of a Taylor cell wherein the Taylor number is specified and the vortex intensity is a consequence of the material parameters of the simulation.

REFERENCES

1. Molina-Grima, E., et al., *Recovery of microalgal biomass and metabolites: process options and economics.* Biotechnology Adv., 2003. **20**: p. 491-515.
2. Sukenik, A., D. Bilanovic, and G. Shelef, *Flocculation of microalgae in brackish and sea waters.* Biomass, 1988. **15**(3): p. 187-199.
3. Wijffels, R.H. and M.J. Barbosa, *An Outlook on Microalgal Biofuels.* Science, 2010. **329**(5993): p. 796-799.
4. Hu, Q., et al., *Microalgal triacylglycerols as feedstocks for biofuel production: perspectives and advances.* Plant Journal, 2008. **54**(4): p. 621-639.
5. Pienkos, P.T. and A. Darzins, *The promise and challenges of microalgal-derived biofuels.* Biofuels Bioproducts & Biorefining-Biofpr, 2009. **3**(4): p. 431-440.
6. Vasudevan, P.T. and M. Briggs, *Biodiesel production-current state of the art and challenges.* Journal of Industrial Microbiology & Biotechnology, 2008. **35**(5): p. 421-430.
7. Chisti, Y., *Biodiesel from microalgae.* Biotechnology Advances, 2007. **25**(3): p. 294-306.
8. Chisti, Y., *Biodiesel from microalgae beats bioethanol.* Trends in Biotechnology, 2008. **26**(3): p. 126-131.
9. Uduman, N., et al., *Dewatering of microalgal cultures: A major bottleneck to algae-based fuels.* Journal of Renewable and Sustainable Energy, 2010. **2**(1).
10. Brennan, L. and P. Owende, *Biofuels from microalgae-A review of technologies for production, processing, and extractions of biofuels and co-products.* Renewable & Sustainable Energy Reviews, 2010. **14**(2): p. 557-577.
11. Sun, A., et al., *Comparative cost analysis of algal oil production for biofuels.* Energy, 2011. **36**(8): p. 5169-5179.
12. Williams, P.J.l.B. and L.M.L. Laurens, *Microalgae as biodiesel & biomass feedstocks: Review & analysis of the biochemistry, energetics & economics.* Energy & Environmental Science, 2010. **3**(5): p. 554-590.
13. Zhang, X., et al., *Harvesting algal biomass for biofuels using ultrafiltration membranes.* Bioresource Technology, 2010. **101**(14): p. 5297-5304.
14. Ayoub, G.M., S.I. Lee, and B. Koopman, *Seawater Induced Algal Focculation.* Water Research, 1986. **20**(10): p. 1265-1271.
15. Bilanovic, D., G. Shelef, and A. Sukenik, *Flocculation of microalgae with cationic polymers--effects of medium salinity.* Biomass, 1988. **17**(1): p. 65-76.
16. Chen, J.J. and H.H. Yeh, *The mechanisms of potassium permanganate on algae removal.* Water Research, 2005. **39**(18): p. 4420-4428.
17. Henderson, R., et al., *Identifying the linkage between particle characteristics and understanding coagulation performance*, in *Particle Separation 2005 - Drinking Water Treatment*, M.Y. Han, K.H. Park, and S. Dockko, Editors. 2006. p. 31-38.
18. Henderson, R.K., S.A. Parsons, and B. Jefferson, *Successful removal of algae through the control of zeta potential.* Separation Science and Technology, 2008. **43**(7): p. 1653-1666.
19. Horiuchi, J.I., et al., *Effective cell harvesting of the halotolerant microalga Dunaliella tertiolecta with pH control.* Journal of Bioscience and Bioengineering, 2003. **95**(4): p. 412-415.

20. Knuckey, R.M., et al., *Production of microalgal concentrates by flocculation and their assessment as aquaculture feeds.* Aquacultural Engineering, 2006. **35**(3): p. 300-313.
21. Lee, A.K., D.M. Lewis, and P.J. Ashman, *Microbial flocculation, a potentially low-cost harvesting technique for marine microalgae for the production of biodiesel.* J. Applied Phycol., 2009. **21**: p. 559–567.
22. McGarry, M.G. and Tongkasa.C, *Water reclamation and algae harvesting.* Journal Water Pollution Control Federation, 1971. **43**(5): p. 824-&.
23. Morales, J., J. Delanoue, and G. Picard, *Harvesting marine microalgae species by chitosan flocculation.* Aquacultural Engineering, 1985. **4**(4): p. 257-270.
24. Oh, H.M., et al., *Harvesting of Chlorella vulgaris using a bioflocculant from Paenibacillus sp AM49.* Biotechnology Letters, 2001. **23**(15): p. 1229-1234.
25. Pan, G., et al., *Removal of cyanobacterial blooms in Taihu Lake using local soils. I. Equilibrium and kinetic screening on the flocculation of Microcystis aeruginosa using commercially available clays and minerals.* Environmental Pollution, 2006. **141**(2): p. 195-200.
26. Pan, G., et al., *Removal of harmful cyanobacterial blooms in Taihu Lake using local soils. III. Factors affecting the removal efficiency and an in situ field experiment using chitosan-modified local soils.* Environmental Pollution, 2006. **141**(2): p. 206-212.
27. Papazi, A., P. Makridis, and P. Divanach, *Harvesting Chlorella minutissima using cell coagulants.* J. Applied Phycol., 2010. **22**: p. 349-355.
28. Pierce, R.H., et al., *Removal of harmful algal cells (Karenia brevis) and toxins from seawater culture by clay flocculation.* Harmful Algae, 2004. **3**(2): p. 141-148.
29. Sengco, M.R. and D.M. Anderson, *Controlling harmful algal blooms through clay Flocculation.* Journal of Eukaryotic Microbiology, 2004. **51**(2): p. 169-172.
30. Spilling, K., J. Seppälä, and T. Tamminen, *Inducing autoflocculation in the diatom Phaeodactylum tricornutum through CO2 regulation.* J. Applied Phycol., 2010.
31. Sukenik, A., et al., *Coprecipitation of microalgal biomass with calcium and phosphate ions.* Water Research, 1985. **19**(1): p. 127-129.
32. Sukenik, A. and G. Shelef, *Algal autoflocculation--verification and proposed mechanism.* Biotechnology and Bioengineering, 1984. **26**(2): p. 142-147.
33. Sukenik, A., et al., *Effects of oxidants on microalgal floculation.* Water Research, 1987. **21**(5): p. 533-539.
34. Vandamme, D., et al., *Flocculation of microalgae using cationic starch.* Journal of Applied Phycology, 2010. **22**(4): p. 525-530.
35. Vandamme, D., et al., *Evaluation of Electro-Coagulation-Flocculation for Harvesting Marine and Freshwater Microalgae.* Biotechnology and Bioengineering, 2011. **108**(10): p. 2320-2329.
36. Wu, Z.C., et al., *Evaluation of flocculation induced by pH increase for harvesting microalgae and reuse of flocculated medium.* Bioresource Technology, 2012. **110**: p. 496-502.
37. Wyatt, N.B., et al., *Critical conditions for ferric chloride-induced flocculation of freshwater algae.* Biotechnology and Bioengineering, 2012. **109**(2): p. 493-501.
38. Zhang, X., et al., *Influence of growth phase on harvesting of Chlorella zofingiensis by dissolved air flotation.* Bioresource Technology, 2012. **116**: p. 477-484.

39. Zou, H., et al., *Removal of cyanobacterial blooms in Taihu Lake using local soils. II. Effective removal of Microcystis aeruginosa using local soils and sediments modified by chitosan.* Environmental Pollution, 2006. **141**(2): p. 201-205.
40. Bratby, J., *Coagulation and Flocculation in Water and Wastewater Treatment* 2nd ed. 2008 International Water Association (IWA).
41. Gregory, J., *Fundamentals of Flocculation.* Crit. Rev. Environ. Sci. Tech., 1989. **19**(3): p. 185-230.
42. Duan, J.M. and J. Gregory, *Coagulation by hydrolysing metal salts.* Advances in Colloid and Interface Science, 2003. **100**: p. 475-502.
43. Leppard, G.G., *Colloidal organic fibrils of acid polysaccharides in surface waters: Electron-optical characteristics, activities and chemical estimates of abundance.* Colloids and Surfaces a-Physicochemical and Engineering Aspects, 1997. **120**(1-3): p. 1-15.
44. Hadjoudja, S., V. Deluchat, and M. Baudu, *Cell surface characterisation of Microcystis aeruginosa and Chlorella vulgaris.* Journal of Colloid and Interface Science, 2010. **342**(2): p. 293-299.
45. Ives, K.J., *The Significance of surface electric charge on algae in water purification.* J. Biochemical Microbiological Tech. Engineer., 1959. **1**(1): p. 37-47.
46. Zhang, X., et al., *Critical Evaluation and Modeling of Chlorella zofingiensis Harvesting Using Dissolved Air Flotation.* in preparation, 2012.
47. Dempsey, B.A., R.M. Ganho, and C.R. Omelia, *The Coagulation of Humic Substances by Means of Aluminum Salts.* Journal American Water Works Association, 1984. **76**(4): p. 141-150.
48. Wesolowski, D.J. and D.A. Palmer, *Aluminum speciation and equilibria in aqueous solution 5. Gibbsite solubility at 50-degrees C and pH 3--9 in 0.1 molal NaCl solutions (A general model for aluminum speciation--analytical methods).* Geochimica Et Cosmochimica Acta, 1994. **58**(14): p. 2947-2969.
49. Flynn, C.M., *Hydrolysis of inorganic iron(III) salts.* Chemical Reviews, 1984. **84**(1): p. 31-41.
50. Henderson, R.K., et al., *Characterisation of algogenic organic matter extracted from cyanobacteria, green algae and diatoms.* Water Research, 2008. **42**(13): p. 3435-3445.
51. Shin, J.Y. and C.R. O'Melia, *Pretreatment chemistry for dual media filtration: model simulations and experimental studies.* Water Science and Technology, 2006. **53**(7): p. 167-175.
52. Shin, J.Y., R.F. Spinette, and C.R. O'Melia, *Stoichiometry of coagulation revisited.* Environmental Science & Technology, 2008. **42**(7): p. 2582-2589.
53. Vandamme, D., et al., *Flocculation of Chlorella vulgaris induced by high pH: Role of magnesium and calcium and practical implications.* Bioresource Technology, 2012. **105**: p. 114-119.
54. Schlesinger, A., et al., *Inexpensive non-toxic flocculation of microalgae contradicts theories; overcoming a major hurdle to bulk algal production.* Biotechnology Advances, 2012. **30**(5): p. 1023-30.
55. Brady, P.V., P.I. Pohl, and J.C. Hewson, *A Coordination Chemistry Model of Algae Autoflocculation.* Algal Research, submitted 2012.
56. Henderson, R., S.A. Parsons, and B. Jefferson, *The impact of algal properties and pre-oxidation on solid-liquid separation of algae.* Water Research, 2008. **42**: p. 1827-1845.

57. Hadjoudja, S., V. Deluchat, and M. Baudu, *Cell surface characterisation of Microcystis aeruginosa and Chlorella vulgaris.* J. Coll. Interf. Science, 2010. **342**: p. 293-299.
58. Parkhurst, D.L. and C.A.J. Appelo, *User's guide to PHREEQC (Version 2) - A computer program for speciation, batch-reaction, one-dimensional transport, and inverse geochemical calculations.*, U.S. GEOLOGICAL SURVEY, 1999.
59. Turner, B.F. and J.B. Fein, *Protofit: A program for determining surface protonation constants from titration data.* Comput. Geosci. , 2006. **32**(9): p. 1344-1356.
60. Dzombak, D.A. and F.M.M. Morel, *Surface Complexation Modeling: Hydrous Ferric Oxide*. 1990: John Wiley and Sons. 393.
61. Pokrovsky, O.S. and J. Schott, *Surface chemistry and dissolution kinetics of divalent metal carbonates.* Environ. Sci. Tech., 2002. **36**: p. 426-432.
62. Stumm, W. and J.J. Morgan, *Aquatic Chemistry*. 1996, New York: Wiley-Interscience.
63. Van Cappellen, P., et al., *A surface complexation model of the carbonate mineral-aqueous solution interface.* Geochim. Cosmochim. Acta., 1993. **57**: p. 3505-3518.
64. Keating, E. and J. Fabryka-Martin, *Assessment of the Potential to Inject RO Concentrate into New Mexico Saline Aquifers: Focus on Chemical Compatibility* Los Alamos National Laboratory: Los Alamos, New Mexico, 2006.
65. Tarquin, T., *High tech methods to reduce concentrate volumes prior to disposal. Draft Final Report to Texas Water Development Board*, University of Texas at El Paso, 2009.
66. Tang, P., J. Greenwood, and J.A. Raper, *A model to describe the settling behavior of fractal aggregates.* Journal of Colloid and Interface Science, 2002. **247**(1): p. 210-219.
67. Johnson, C.P., X.Y. Li, and B.E. Logan, *Settling velocities of fractal aggregates.* Environmental Science & Technology, 1996. **30**(6): p. 1911-1918.
68. Spicer, P.T. and S.E. Pratsinis, *Shear-induced flocculation: The evolution of floc structure and the shape of the size distribution at steady state.* Water Research, 1996. **30**(5): p. 1049-1056.
69. Spicer, P.T. and S.E. Pratsinis, *Coagulation and fragmentation: Universal steady-state particle-size distribution.* Aiche Journal, 1996. **42**(6): p. 1612-1620.
70. Serra, T. and X. Casamitjana, *Structure of the aggregates during the process of aggregation and breakup under a sheer flow.* Journal of Colloid and Interface Science, 1998. **206**(2): p. 505-511.
71. Serra, T., J. Colomer, and X. Casamitjana, *Aggregation and breakup of particles in a shear flow.* Journal of Colloid and Interface Science, 1997. **187**(2): p. 466-473.
72. Soos, M., et al., *Population balance modeling of aggregation and breakage in turbulent Taylor-Couette flow.* Journal of Colloid and Interface Science, 2007. **307**(2): p. 433-446.
73. Selomulya, C., et al., *Aggregation mechanisms of latex of different particle sizes in a controlled shear environment.* Langmuir, 2002. **18**(6): p. 1974-1984.
74. Selomulya, C., et al., *Aggregate properties in relation to aggregation conditions under various applied shear environments.* International Journal of Mineral Processing, 2004. **73**(2-4): p. 295-307.
75. Wang, D., et al., *Characterization of floc structure and strength: Role of changing shear rates under various coagulation mechanisms.* Colloids and Surfaces a-Physicochemical and Engineering Aspects, 2011. **379**(1-3): p. 36-42.
76. Spicer, P.T., et al., *Effect of shear schedule on particle size, density, and structure during flocculation in stirred tanks.* Powder Technology, 1998. **97**(1): p. 26-34.

77. Jarvis, P., B. Jefferson, and S.A. Parsons, *Breakage, regrowth, and fractal mature of natural organic matter flocs.* Environmental Science & Technology, 2005. **39**(7): p. 2307-2314.
78. UTEX. *The Culture Collection of Algae. BG-11 Medium.* 2009 August 2010]; Available from: http://web.biosci.utexas.edu/utex/media.aspx.
79. Kilps, J.R., B.E. Logan, and A.L. Alldredge, *FRACTAL DIMENSIONS OF MARINE SNOW DETERMINED FROM IMAGE-ANALYSIS OF IN-SITU PHOTOGRAPHS.* Deep-Sea Research Part I-Oceanographic Research Papers, 1994. **41**(8): p. 1159-&.
80. Logan, B.E. and J.R. Kilps, *FRACTAL DIMENSIONS OF AGGREGATES FORMED IN DIFFERENT FLUID MECHANICAL ENVIRONMENTS.* Water Research, 1995. **29**(2): p. 443-453.
81. Logan, B.E. and D.B. Wilkinson, *FRACTAL GEOMETRY OF MARINE SNOW AND OTHER BIOLOGICAL AGGREGATES.* Limnology and Oceanography, 1990. **35**(1): p. 130-136.
82. Li, D.H. and J. Ganczarczyk, *Fractal geometry of particle aggregates generated in water and wate-water treatment processes.* Environmental Science & Technology, 1989. **23**(11): p. 1385-1389.
83. Chakraborti, R.K., et al., *Changes in fractal dimension during aggregation.* Water Research, 2003. **37**(4): p. 873-883.
84. Gelbard, F., Y. Tambour, and J.H. Seinfeld, *Sectional representations for simulating aerosol dynamics.* J. Colloid Interface Sci., 1980. **76**(2): p. 541-556.
85. Chellam, S. and M.R. Wiesner, *Evaluation of crossflow filtration models based on shear-induced diffusion and particle adhesion: Complications induced by feed suspension polydispersivity.* Journal of Membrane Science, 1998. **138**(1): p. 83-97.
86. Li, X.Y. and B.E. Logan, *Collision frequencies between fractal aggregates acid small particles in a turbulently sheared fluid.* Environmental Science & Technology, 1997. **31**(4): p. 1237-1242.
87. Li, X.Y. and B.E. Logan, *Permeability of fractal aggregates.* Water Research, 2001. **35**(14): p. 3373-3380.
88. Han, M.Y. and D.F. Lawler, *The (relative) insignificance of G in flocculation.* J. American Water Works Assoc., 1992. **84**(10): p. 79-91.
89. Li, X.Y. and B.E. Logan, *Collision frequencies of fractal aggregates with small particles by differential sedimentation.* Environmental Science & Technology, 1997. **31**(4): p. 1229-1236.
90. Jarvis, P., et al., *A review of floc strength and breakage.* Water Research, 2005. **39**(14): p. 3121-3137.
91. Shamlou, P.A., et al., *Growth-independent breakage frequency of protein precipitates in turbulently agitated bioreactors.* Chemical Engineering Sciences, 1994. **49**(16): p. 2647-2656.
92. Thomas, D.N., S.J. Judd, and N. Fawcett, *Flocculation modelling: A review.* Water Research, 1999. **33**(7): p. 1579-1592.
93. Parker, D.S., et al., *Floc breakup in turbulent flocculation processes.* J. Sanitary Engineer. Div.-ASCE, 1972. **98**(NSA1): p. 79-&.
94. Flesch, J.C., P.T. Spicer, and S.E. Pratsinis, *Laminar and turbulent shear-induced flocculation of fractal aggregates.* Aiche Journal, 1999. **45**(5): p. 1114-1124.

95. Frenklach, M., *Method of moments with interpolative closure.* Chemical Engineer. Sci., 2002. **57**(12): p. 2229-2239.
96. McGraw, R., *Description of aerosol dynamics by the quadrature method of moments.* Aerosol Science and Technology, 1997. **27**(2): p. 255-265.
97. Samson, R.J., G.W. Mulholland, and J.W. Gentry, Langmuir, 1987. **3**: p. 272.
98. Bourrrat, X., et al., Carbon, 1988. **26**: p. 100.
99. Cai, J., N. Lu, and C.M. Sorensen, J. Coll. Int. Sci., 1995. **171**: p. 470.
100. Chakrabarty, R.K., et al., Aerosol Sci., 2008. **9**: p. 785.
101. Charalampopoulos, T.T. and H. Chang, Combust. Flame, 1991. **87**: p. 89.
102. Chokshi, A., A.G.G.M. Tielens, and D. Hollenbach, Astrophys. J., 1993. **407**: p. 806.
103. Dhaubhadel, R., et al., Phys. Rev. E, 2006. **73**: p. 011404.
104. Dobbins, R.A. and C.M. Megaridis, Langmuir, 1987. **3**: p. 254.
105. Gangopadhyay, S., I. Elminyawi, and C.M. Sorensen, Appl. Opt., 1991. **25**: p. 4859.
106. Koylu, U.O. and G.M. Faeth, Combust. Flame, 1992. **89**: p. 140.
107. Koylu, U.O. and G.M. Faeth, J. Heat Transfer, 1994. **116**: p. 152.
108. Koylu, U.O., et al., Combust. Flame, 1995. **100**: p. 621.
109. Puri, R., et al., Combust. Flame, 1993. **92**: p. 320.
110. Sorensen, C.M., J. Cai, and N. Lu, Langmuir, 1992. **8**: p. 2064.
111. Sorensen, C.M., J. Cai, and N. Lu, Appl. Opt., 1992. **31**: p. 6547.
112. Sorensen, C.M. and G.D. Feke, Aerosol Sci. Tech., 1996. **25**: p. 328.
113. Zhang, H.X., et al., Langmuir, 1988. **4**: p. 867.
114. Cai, J., N. Lu, and C.M. Sorensen, Langmuir, 1993. **9**: p. 2861.
115. Ducoste, J., Chem. Eng. Sci., 2002. **57**: p. 2157.
116. Dyer, K.R. and A.J. Manning, J. Sea Res., 1999. **41**: p. 87.
117. Nan, J., et al., 2009 Int. Conf. on Energy and Env. Tech., 2009. **2009**: p. 582.
118. Torfs, E., A. Dutta, and I. Nopens, Chem. Eng. Sci., 2012. **70**: p. 176.
119. Meakin, P., J. of Sol-Gel Sci. Tech., 1999. **15**: p. 97.
120. Hasmy, A., J. of Sol-Gel Sci. Tech., 1999. **15**: p. 137.
121. Meakin, P., J. Colloid Int. Sci., 1984. **102**: p. 505.
122. Mulholland, G.W., et al., Energy Fuels, 1988. **2**: p. 481.
123. Adachi, Y. and K. Aoki, Coll. Surf. A, 2009. **342**: p. 24.
124. Axford, S.D.T., J. Chem. Soc. Faraday Trans., 1996. **92**: p. 1007.
125. Barthelmes, G., S.E. Pratsinis, and H. Buggisch, Chem. Eng. Sci., 2003. **58**: p. 2893.
126. Eggersdorfer, M.L., et al., J. Coll. Int. Sci., 2010. **342**: p. 261.
127. Oles, V., J. Colloid Int. Sci., 1992. **154**: p. 351.
128. Rahimi, H. and A.R.S. Nazar, Energy Fuels, 2010. **24**: p. 1088.
129. Spicer, P.T., W. Keller, and S.E. Pratsinis, J. Coll. Int. Sci., 1996. **184**: p. 112.
130. Spirito, M.D., et al., Physica A, 2002. **304**: p. 211.
131. Thill, A., et al., J. Coll. Int. Sci., 2001. **243**: p. 171.
132. Wang, L., et al., J. Coll. Int. Sci., 2005. **282**: p. 380.
133. Kim, W., C.M. Sorensen, and A. Chakrabarti, Langmuir, 2004. **20**: p. 3969.
134. Kim, W., et al., Aersol Sci., 2006. **37**: p. 386.
135. Sorensen, C.M., et al., Langmuir, 2003. **19**: p. 7560.
136. Fry, D., et al., Phys. Rev. E, 2004. **69**: p. 061401.
137. Seto, R., R. Botet, and H. Briesen, Phys. Rev. E, 041405. **84**: p. 2011.
138. Vanni, M. and A. Gastaldi, Langmuir, 2011. **27**: p. 12822.

139. Dominik, C. and A.G.G.M. Tielens, Phil. Mag. A, 1995. **3**: p. 783.
140. Dominik, C. and A.G.G.M. Tielens, Astrophys. Jour., 1997. **480**: p. 647.
141. Marshall, J.S., Jour. of Comput. Physics, 2009. **228**: p. 1541.
142. Zhao, Y. and J.S. Marshall, Phys. of Fluids, 2008. **20**: p. 043302.
143. Plimpton, S., J. Comp. Phys., 1995. **117**: p. 1.
144. Cleary, W., G. Metcalfe, and K. Liffman, Appl. Math. Model., 1998. **22**: p. 995.
145. Mindlin, D., J. Appl. Mech., 1949. **16**: p. 259.
146. Silbert, L.E., et al., Phys. Rev. E, 2001. **64**: p. 051302.
147. Brilliantov, N.V., et al., Phys. Rev. E, 2007. **76**: p. 051302.
148. Johnson, K.L., K. Kendall, and A.D. Roberts, Proc. Royal Soc. London A, 1971. **324**: p. 301.
149. Sorensen, C.M. and G. Roberts, J. Coll. Int. Sci., 1997. **186**: p. 447.
150. Sorensen, C.M., Aerosol Sci. Tech., 2001. **35**: p. 648.
151. Rintoul, M.D. and S. Torquato, Phys. Rev. E., 1998. **58**: p. 532.

DISTRIBUTION

4 Arizona State University
Attn: Prof. Qiang Hu (1)
Attn: John McGowan (1)
Attn: Prof. Milton Sommerfeld (1)
Attn: Dr. Xuezhi Zhang (1)
Department of Applied Sciences and Mathematics
Arizona State University, Polytechnic Campus
Mesa, AZ 85212

1	MS0346	Anne Grillet	1512
1	MS0346	Lisa Mondy	1512
1	MS0346	Nicholas Wyatt	1512
1	MS0346	Lindsey Hughes	1512
1	MS0359	D. Chavez, LDRD Office	1911
1	MS0735	Ron Pate	6926
1	MS0735	John Merson	6910
1	MS0754	Patrick V. Brady	6910
1	MS0836	Flint Pierce	1541
1	MS0836	Jeremy Lechman	1516
1	MS0836	Anthony Geller	1516
1	MS0836	Chris Bourdon	1512
1	MS0840	Tim O'Hern	1512
1	MS0873	Matthew Hankins	2712
1	MS0899	Technical Library	9536 (electronic copy)
1	MS1108	Ray Finley	6111
1	MS1132	Randy Watkins	1532
1	MS1413	James Carney	8622
1	MS1413	Kylea Parchert	8622
1	MS9291	Blake Simmons	8630
1	MS9292	Cathy Branda	8623
1	MS9292	ToddLane	8623
1	MS9292	Ben Wu	8634
1	MS9409	Patricia Gharagozloo	8365
1	MS9671	Ryan Davis	8634


Sandia National Laboratories